Development of a Vectored Electrospray Thruster for Nanosatellites

Développement d'un propulseur à électropulvérisation vectorielle pour nanosatellites

A Thesis Submitted to the Division of Graduate Studies of the
Royal Military College of Canada
by

Ivan Savytskyy

In Partial Fulfillment of the Requirements for the Degree of
Master of Applied Science in Aeronautical Engineering

April 2023

Development of a Vectored Electrospray Thruster for Nanosatellites

Développement d'un propulseur à électropulvérisation vectorielle pour nanosatellites

Candidate / Candidat

Ivan Savytskyy *Royal Military College of Canada*	MASc Candidate in Aeronautical Engineering / Maîtrise candidat en génie aéronautique

Examination Committee / Comité examinateur

Dr. Mariam El Mezouar *Royal Military College of Canada*	Chair / Président
Dr. James Stotz *Queen's University*	External / Externe
Dr. Francois Chan *Royal Military College of Canada*	Internal-External / Interne-Externe
Dr. Azemi Benaissa *Royal Military College of Canada*	Internal / Interne
Dr. Manish Jugroot *Royal Military College of Canada*	Supervisor / Superviseur

Abstract

Next-generation nanosatellite missions, such as autonomous rendezvous and docking operations, nanosatellite constellations and formations, deep space laser communication, and space-based telescopes, will require precise linear impulse and torque bits for optimized attitude and trajectory control. To address this requirement, a Vectored Electrospray Thruster (VET) that provides high-resolution multi-axis attitude actuation via thrust vector control is currently being developed at the Royal Military College of Canada Advanced Propulsion and Plasma Exploration Laboratory (RAPPEL). The VET employs arrays of linear porous wedge emitters and uses pulse-width modulation to produce stepped emission differentials across the nanosatellite propulsion plane. A two-emitter prototype offering single-axis attitude actuation was developed to validate the thruster concept. A custom power processing unit was built to generate the high-voltage rails necessary for electrospray emission and measure the power consumed by the thruster, while a complementary diagnostics suite was used to characterize the thruster performance. The experimental campaign was bolstered with analytical modeling of the emission profile, which was used to estimate the thrust profile and inform the thruster design. The prototype was tested in the RAPPEL high-vacuum chamber and successfully demonstrated pulsed electrospray emission as well as sequential and simultaneous operation of two emitters, ultimately validating the VET concept.

Résumé

Les missions de nanosatellites de nouvelle génération, telles que les opérations de rendez-vous et d'amarrage autonomes, les constellations et formations de nanosatellites, la communication laser dans l'espace lointain et les télescopes spatiaux, nécessiteront des bits d'impulsion et de couple linéaires précis pour un contrôle optimisé de l'attitude et de la trajectoire. Pour répondre à cette exigence, un propulseur à électropulvérisation vectorielle (VET) qui fournit un actionnement d'attitude multi-axes à haute résolution via un contrôle vectoriel de poussée est actuellement en cours de développement au Laboratoire de propulsion avancée et d'exploration de plasma (RAPPEL) du Collège militaire royal du Canada. Le VET utilise des réseaux d'émetteurs linéaires à coins poreux et utilise la modulation de largeur d'impulsion pour produire des différentiels d'émission échelonnés sur le plan de propulsion du nanosatellite. Un prototype à deux émetteurs offrant un actionnement d'attitude sur un seul axe a été développé pour valider le concept de propulseur. Une unité de traitement de puissance sur mesure a été construite pour générer les rails haute tension nécessaires à l'émission d'électrospray et mesurer la puissance consommée par le propulseur, tandis qu'une suite de système de diagnostic complémentaire a été utilisée pour caractériser les performances du propulseur. La campagne expérimentale a été renforcée par une modélisation analytique du profil d'émission, qui a été utilisée pour estimer le profil de poussée et éclairer la conception du propulseur. Le prototype a été testé dans la chambre à vide RAPPEL et a démontré avec succès l'émission d'électronébulisation pulsée ainsi que le fonctionnement séquentiel et simultané de deux émetteurs, validant finalement le concept VET.

Acknowledgements

Principally, I would like to thank Dr. Manish Jugroot for his mentorship and collaboration and for providing me with the opportunity to participate in the advanced research being conducted at the Royal Military College of Canada Advanced Propulsion and Plasma Exploration Laboratory. Further, I would like to thank the Department of Mechanical and Aerospace Engineering shop, chiefly Mr. Brendan Freeman and Mr. Charles Sadiq, as well as the Department of Electrical and Computer Engineering shop, primarily Dr. Germaine Drolet and Mr. Tristan Redish, for their assistance in the design and fabrication of the experimental prototype developed herein. Additionally, I would like to thank Dr. Jennifer Snelgrove from the Department of Chemistry and Chemical Engineering for granting access to the scanning electron microscope.

I would like to acknowledge the support and funding of the Natural Sciences and Engineering Research Council of Canada Discovery Grant and Collaborative Research and Training Experience International Space Mission Training Program as well as the Director General Air and Space Force Development.

Contents

List of Figures

List of Tables

Nomenclature

A, B, C	scaling parameter - specific charge
C_E	scaling parameter - electric field
d	diameter
D	distance
D_{ToF}	distance - time-of-flight
D_{PWM}	duty cycle
E	electric field
E_{p}	primary electric field
F	force
F_{e}	force - electric
F_{ST}	force - surface tension
g_0	gravitational acceleration on Earth
I	current
I_{emit}	current - emitted
I_{site}	current - emission site
I_{total}	current - total
I_{sp}	specific impulse
I_τ	moment of inertia
k	permeability
L	length
L_{emit}	length - emitter
L_τ	length - lever
m	mass
m_{f}	mass - final
m_{i}	mass - initial
m_{prop}	mass - propellant
P	pressure
P_E	pressure - electric
P_{int}	pressure - interfacial
P_{men}	pressure - meniscus
P_γ	pressure - Young-Laplace
P_{in}	power - input
P_{jet}	power - jet
q_{drop}	droplet charge
q_{sp}	specific charge
Q	volumetric flow rate
Q_{min}	volumetric flow rate - minimum

Q_{por}	volumetric flux
R	resistance
R_{drop}	radius - droplet
R_{res}	radius - reservoir
R_{emit}	radius - emitter
Re	Reynolds number
t	time
T	thrust
u	fluid velocity
v	velocity
v_{exit}	exit velocity
V	voltage
V_{BC}	voltage - boost converter
V_{bus}	voltage - bus
V_{in}	voltage - input
V_{mon}	voltage - monomer
V_{on}	voltage - onset
V_{SR}	voltage - shunt resistor
V_{VD}	voltage - voltage divider
V_{VM}	voltage - voltage multiplier
Z	hydraulic impedance
γ	surface tension coefficient
Δt	change in time
Δv	change in velocity
Δx	displacement
$\Delta \omega$	change in angular velocity
ϵ	electric permittivity
ϵ_{r}	electric permittivity - relative
ϵ_0	electric permittivity - vacuum
η	scaling parameter - onset voltage
η_{tot}	efficiency - total
η_{poly}	efficiency - polydispersive
θ_{w}	wedge full angle
κ	curvature
λ	emission site spacing
μ	dynamic viscosity
ρ	mass density
ρ_{e}	charge density
σ_{e}	electric conductivity
τ	torque
ϕ	porosity
ω	angular velocity

Acronyms

ADC	Analog-to-digital converter
ADCS	Attitude Determination and Control System
ADS-B	Automatic Dependent Surveillance-Broadcast
AFET	Air Force Electrospray Thruster
AJ	Arcjet
AMUSE	Array of Micromachined UltraSonic Electrospray
ARVD	Autonomous rendezvous and docking
ASCENT	Advanced Spacecraft Energetic Non-Toxic
BET	Busek Electrospray Thruster
BET-MAX	BET Multi-Axis
BIT	Busek Ion Thruster
BMI-FeBr4	1-butyl-3-methylimidazolium iron tetrabromide
BRICSat	Ballistic Reinforced Communication Satellite
Cal Poly	California Polytechnic State University
CanX	Canadian Advanced Nanospace eXperiment
CAPSTONE	Cislunar Autonomous Positioning System Technology Operations and Navigation Experiment
CCP	Canadian CubeSat Project
CDH	Command and Data Handling
CEHDA	Coaxial EHD atomization
CMNT	Colloid Micro-Newton Thruster
CNAPS	Canadian Nanosatellite Advanced Propulsion System
CNC	Computer numerical control
COTS	Commercial-off-the-shelf
CSA	Canadian Space Agency
CTRL	Control
CUBICS	CubeSats Initiative in Canada for STEM
CWVM	Cockcroft-Walton voltage multiplier
DAC	Digital-to-analog converter
DAQ	Data acquisition
DC	Direct current
DCIU	Data and command interface unit
DPSS	Diode-pumped solid-state
DRS	Disturbance Reduction System
DSN	Deep Space Network
E0	Emitter 0
E1	Emitter 1

EDL	Entry, descent, and landing
EHD	Electrohydrodynamic
EM	Electromagnetic
EMI-Im	1-ethyl-3-methylimidazolium bis(trifluoromethylsulfonyl)imide
EMI-BF4	1-ethyl-3-methylimidazolium tetrafluoroborate
EMI-GaCl4	1-ethyl-3-methylimidazolium gallium tetrachloride
EOL	End-of-life
EP	Electric propulsion
EPFL	École Polytechnique Fédérale de Lausanne
EPS	Electrical Power System
ES	Electrostatic
ESG	Electron suppression grid
ESP	Electrospray propulsion
ESPET	Electrospray Propulsion Engineering Toolkit
FEEP	Field emission electric propulsion
FHWN	University of Applied Sciences Wiener Neustadt
FOTEC	Forschungs- und Technologietransfer GmbH
GIT	Gridded ion thruster
GNC	Guidance, Navigation, and Control
GPS	Global Positioning System
GSE	Ground support equipment
GUI	Graphical interface unit
GWU	George Washington University
HAN	Hydroxylammonium nitrate
HET	Hall effect thruster
HQP	Highly qualified personnel
HNA	Hydrofluoric, nitric, and acetic acid
HV	High voltage
IC	Integrated circuit
IDE	Integrated development environment
iEPS	Ionic Electrospray Propulsion System
IL	Ionic liquid
IMU	Inertial measurement unit
InSight	Interior Exploration using Seismic Investigations, Geodesy and Heat Transport
Iso-amp	Isolation amplifier
ISS	International Space Station
LHS	Left-Hand Side
LISA	Laser Interferometry Space Antenna
LV	Low voltage
MarCO	Mars Cube One
MEMS	Microelectromechanical systems
MEPS	Monopropellant-electrospray propulsion system
MILET	Modular Ionic Liquid Electrospray Thruster
MIT	Massachusetts Institute of Technology
MMP	Multimode propulsion
MP	Monopropellant
MS	Mass spectrometry
NANOPS	Nano Propulsion System

NASA	National Aeronautics and Space Administration
OBC	Onboard computer
OD	Outer diameter
Op-amp	Operational amplifier
ORCASat	Optical and Radio CAlibration Satellite
PCB	Printed circuit board
PEEK	Polyether ether ketone
PET	Porous-emitter Electrospray Thruster
PIC	Particle-in-cell
PIR	Purely ionic regime
PLA	Poly(lactic acid)
PLGA	Poly(lactic-co-glycolic acid)
PoWEE	Porous Tungsten Electrospray Emitter
PPE	Power and Propulsion Element
PPT	Pulsed plasma thruster
PPU	Power processing unit
PSPL	Plasma and Space Propulsion Laboratory
PTFE	Polytetrafluoroethylene
PWM	Pulse-width modulation
QCM	Quartz crystal microbalance
RAPPEL	Royal Military College of Canada Advanced Propulsion and Plasma Exploration Laboratory
RC	Resistor-capacitor
RF	Radio-frequency
RHS	Right-Hand Side
RJ	Resistojet
RMC	Royal Military College of Canada
RPA	Retarding potential analyzer
RPM	Rotations-per-minute
SEM	Scanning electron microscope
SF6	Sulfur hexafluoride
SFL	Space Flight Laboratory
SiEPS	Scalable iEPS
SMD	Surface mount device
SPI	Serial peripheral interface
SR	Shunt resistor
SWaP	Size, weight, and power
Sum-amp	Summation amplifier
TCM	Trajectory control maneuver
TC	Telecommands
THT	Through-hole-technology
TILE	Tiled Ionic Liquid Electrospray
TM	Telemetry
ToF	Time-of-flight
TPIBC	Two-phase interleaved boost converter
TRL	Technology readiness level
TVC	Thrust vector control
UCLA	University of California, Los Angeles

UIUC	University of Illinois Urbana-Champaign
UTIAS	University of Toronto Institute for Aerospace Studies
UVic	University of Victoria
VAT	Vacuum arc thruster
VD	Voltage divider
VET	Vectored Electrospray Thruster
VOF	Volume-of-fluid
μCAT	Micro Cathode Arc Thruster
μPIM	Micro-powder injection moulding

1 Introduction

An overview of general spacecraft propulsion, nanosatellites, and the efforts to develop propulsion systems for nanosatellites are herein presented. Following this introduction is an outline of the objective and contents of this work.

1.1 Spacecraft Propulsion

Spacecraft propulsion systems provide enhanced capabilities for and greater return from advanced space missions [1]–[3]. Propulsion systems (thrusters) are primarily used for orbital maneuvers, such as altitude and inclination changes and orbit escape and insertion burns, as well as for orbit maintenance (station-keeping) against perturbations due to atmospheric drag, solar radiation pressure, Earth oblateness, and third-body gravitational effects. Propulsion systems are also necessary for deep space trajectory control maneuvers (TCMs) [2]–[4]. For missions involving multiple spacecraft, propulsion is used for constellation and formation management as well as for proximity operations (e.g., rendezvous and docking, on-orbit assembly), and as space becomes increasingly congested, propulsion will be critical for obstacle avoidance [5], [6]. Additionally, propulsion systems may be used for attitude control or reaction wheel desaturation [2], [3], [7].

Spacecraft propulsion systems are divided into three primary classes: chemical, electric, and propellantless [1], [8], [9]. In chemical propulsion systems, energy stored in the propellant chemical bonds is released in the process of combustion—the heated propellant is accelerated through a supersonic nozzle to produce thrust. Electric propulsion (EP) systems use an electrical power supply to electrostatically or electromagnetically accelerate and eject propellant. Finally, propellantless systems use externally-generated energy, such as solar radiation or the geomagnetic field, to propel the spacecraft.

1.1.1 Propulsion Metrics

The purpose of any propulsive maneuver is to impart a change in velocity, or change in momentum, to the spacecraft. The optimal propulsion system is selected based on its ability to provide the required change in velocity, Δv, to the spacecraft under strict power and propellant budgets [10]. The rocket equation, given as

$$\Delta v = v_{\text{exit}} \ln\left(\frac{m_{\text{i}}}{m_{\text{f}}}\right), \tag{1.1}$$

is used to characterize the performance of a system based on its propellant exit velocity in the spacecraft reference frame, v_{exit}, and the mass of propellant it consumes. Here, m_{i} is the spacecraft initial (wet) mass and m_{f} is the spacecraft final (dry) mass, such that the propellant mass is $m_{\text{prop}} = m_{\text{i}} - m_{\text{f}}$ [2], [10]. The first metric for thruster characterization is the thrust T it produces, approximated as

$$T = \dot{m}_{\text{prop}} v_{\text{exit}}, \tag{1.2}$$

where $\dot{m}_{\text{prop}}$ is the propellant mass flow rate. The total impulse (momentum change), of a propulsion system is the integration of the thrust it produces over its operating time. The second metric in characterizing the performance of a thruster is its specific impulse I_{sp}, expressed as the total impulse divided by the mass force of the consumed propellant:

$$I_{\text{sp}} = \frac{T}{\dot{m}_{\text{prop}} g_0} = \frac{v_{\text{exit}}}{g_0}, \tag{1.3}$$

in which g_0 is the gravitational acceleration at the surface of the Earth. Equation 1.1 can thus be rewritten as

$$\Delta v = g_0 I_{\text{sp}} \ln\left(\frac{m_{\text{i}}}{m_{\text{f}}}\right), \tag{1.4}$$

which indicates that the specific impulse is a measure of the propellant mass utilization efficiency for any given Δv profile. Equation 1.4 can be rearranged for the propellant mass in terms of the wet mass

$$m_{\text{prop}} = m_{\text{i}} \left(1 - \exp\left[-\frac{\Delta v}{g_0 I_{\text{sp}}}\right]\right), \tag{1.5}$$

or in terms of the dry mass

$$m_{\text{prop}} = m_{\text{f}} \left(\exp\left[\frac{\Delta v}{g_0 I_{\text{sp}}}\right] - 1\right). \tag{1.6}$$

The thrust produced by the engine must also be taken into consideration, as it determines the burn time, Δt, of a given Δv profile. Engines producing higher thrust reduce the time needed to perform Δv maneuvers or emergency TCMs, giving finer temporal control over the flight trajectory. The burn time is calculated as

$$\Delta t = \frac{m_{\text{i}} g_0 I_{\text{sp}}}{T} \left(1 - \exp\left[-\frac{\Delta v}{g_0 I_{\text{sp}}}\right]\right). \tag{1.7}$$

The principles of propulsion introduced above are illustrated in Fig. 1.1.

A third metric that applies specifically for characterizing the performance of EP systems is the required electrical power, where the input voltage V_{in} and current I_{in} define the applied electrical power via $P_{\text{in}} = V_{\text{in}} I_{\text{in}}$ and the output kinetic jet power P_{jet} is estimated from the thrust and mass flow rate according to [2], [10]:

$$P_{\text{jet}} = \frac{T^2}{2\dot{m}_{\text{prop}}} = \frac{T g_0 I_{\text{sp}}}{2}. \tag{1.8}$$

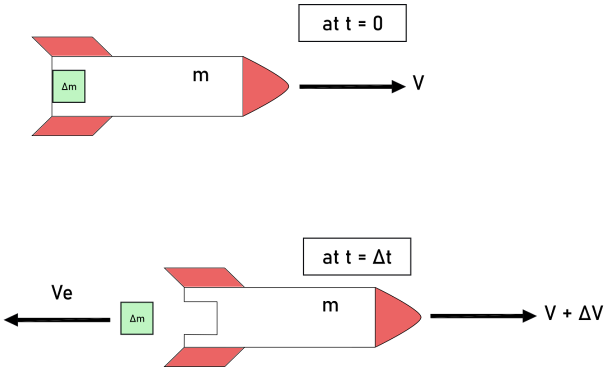

Figure 1.1: Operational principle of spacecraft propulsion (sourced from https://isrofansclub.blogspot.com/2020/10/basics-of-rocketry-rocket-equation.html).

Evidently, an increase in either the thrust or the specific impulse of the engine requires a proportional increase in power, which becomes the ultimate limiting factor for all missions using EP systems. The input and jet power are used to determine the total efficiency of the EP system:

$$\eta_{\mathrm{tot}} = \frac{P_{\mathrm{jet}}}{P_{\mathrm{in}}} = \frac{T^2}{2\dot{m}_{\mathrm{prop}} P_{\mathrm{in}}}. \tag{1.9}$$

Chemical propulsion systems are useful for high-thrust impulsive maneuvers and, moreover, have higher thrust-to-power ratios as compared to EP systems, since energy is stored in chemical bonds rather than relying on electrical power to electrostatically or electromagnetically produce thrust [10]. Due to this property, chemical propulsion systems are most useful for rapid orbital transfer maneuvers, orbit insertion, and deorbiting [11]. However, chemical systems are limited by the energy contained in the chemical bonds of the propellant used, with a typical upper bound on the exit velocities being 4 $\mathrm{km\ s^{-1}}$, equal to 400 s of specific impulse, whereas EP systems can accelerate propellant to exit velocities approaching 100 $\mathrm{km\,s^{-1}}$ or 10,000 s. EP systems typically provide low thrust-to-power ratios of 75 $\mu\mathrm{N\ W^{-1}}$ [8], though the total impulse capabilities of EP systems are typically an order of magnitude higher than chemical systems, making them ideal for long-duration missions. Due to this characteristic, EP systems are replacing chemical systems for upcoming missions. For example, while the International Space Station (ISS) uses chemical propulsion for orbit maintenance [1], a high-power EP system will be used as the primary propulsion system on the upcoming Power and Propulsion Element (PPE) mission [4], [12], rendered in Fig. 1.2, which is the first segment of the Lunar Gateway. Three 12 kW Aerojet Rocketdyne Advanced Electric Propulsion System Hall effect thrusters (HETs) and four Busek BHT-6000 HETs will be used to create the most powerful flight-qualified EP system to date. In any case, optimization studies of these metrics across available propulsion units are performed to select the most suitable system for a given mission profile.

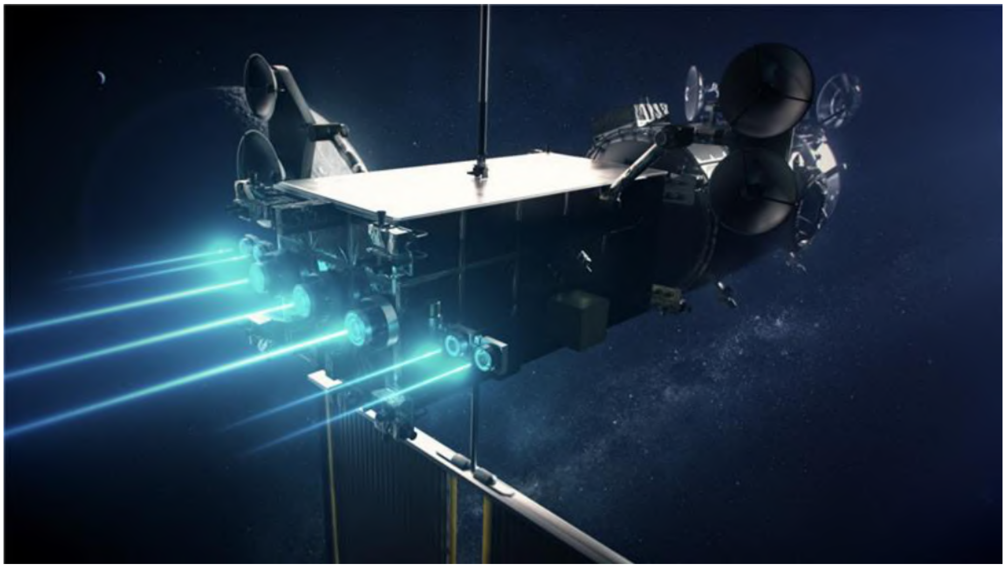

Figure 1.2: Rendering of the PPE, featuring seven high-power HETs (sourced from [12]).

1.2 Nanosatellites Overview

Spacecraft are typically categorized by their mass: microsatellites are classified as spacecraft with a mass below 100 kg, whereas a nanosatellite is classified as a spacecraft with a mass below 10 kg [13]. CubeSats are standardized 10 cm × 10 cm × 10 cm (1U) cubes which have become the accepted form factor for the majority of microsatellite and nanosatellite buses [9]. These units typically have a mass of 1.33 kg as well as 113.5-mm-long rails that extend along each edge for interfacing with a deployer. Several 1U units are assembled together to provide greater mission payload capability, with the 3U configuration of 30 cm × 10 cm × 10 cm (34 cm long including the deployer rails) being the most common platform in the industry [14] and buses up to 12U being launched [15]. An example of a 2U CubeSat, the Optical and Radio CAlibration Satellite (ORCASat) that was developed by the University of Victoria (UVic) [16], is illustrated in Fig. 1.3. Note that, since the majority of nanosatellites launched are 1U to 6U CubeSats [14], the terms nanosatellite and CubeSat are used interchangeably in this work to refer to any spacecraft with mass around or below 10 kg. With these definitions it is also clear that the size, weight, and power (SWaP) constraints of nanosatellites are strict, posing major challenges to nanosatellite subsystem designs.

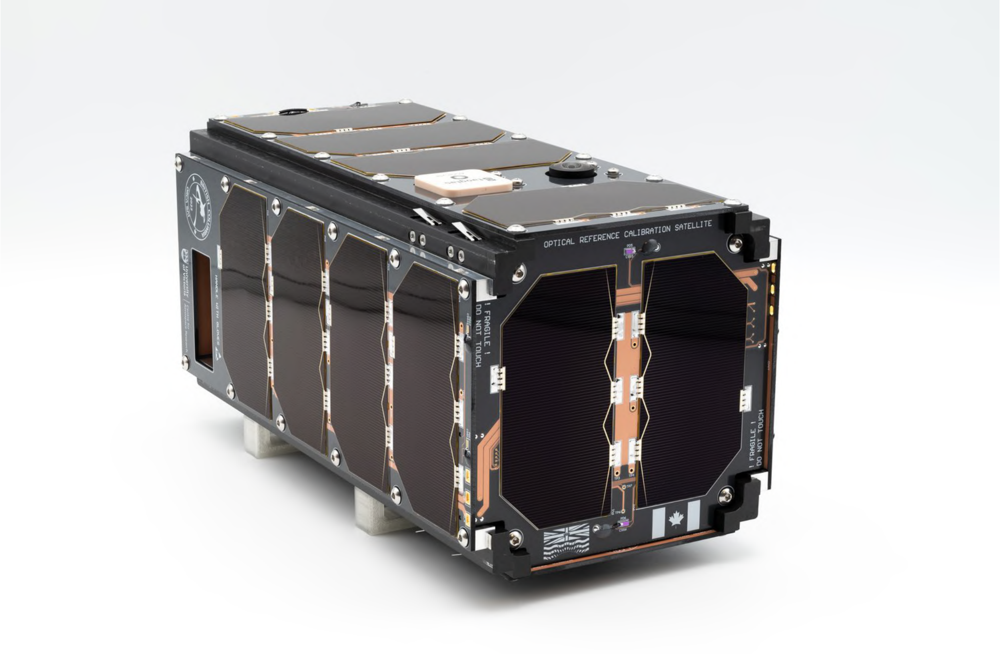

Figure 1.3: ORCASat CubeSat front view (sourced from [17]).

1.2.1 Missions and Programs

Nanosatellites have become a critical asset for the space industry. These platforms provide increased access to previously-ineligible organizations, such as secondary and post-secondary institutions, technology startups, and non-profit organizations, to design, build, launch, and operate satellites. This has led to a significant growth in the number of scientific payloads launched, technology demonstrations performed, and highly qualified personnel (HQP) trained in the space industry [13]. For example, in 2016 the Canadian Space Agency (CSA) launched the Canadian CubeSat Project (CCP) to provide 15 Canadian post-secondary institutions the opportunity to develop CubeSats that would be deployed from the ISS [18]. Two CubeSats, the LORIS CubeSat from Dalhousie University and ORCASat from the University of Victoria, were successfully deployed from the ISS in late 2022, while another four CubeSats from McMaster University, University of Alberta, Yukon University, and Aurora Research Institute of Aurora College deployed from the ISS in early 2023. With the success of the CCP, in late 2022 the CSA launched the CubeSats Initiative in Canada for STEM (CUBICS) program to further stimulate scientific and technological research and facilitate the training of HQP in the Canadian space industry [19].

Notable nanosatellite missions include the Canadian Advanced Nanospace eXperiment (CanX) series. These nanosatellites were developed by the Space Flight Laboratory (SFL) at the University of Toronto Institute for Aerospace Studies (UTIAS) in collaboration with national and international partners as technology demonstration missions. CanX-1 was the first Canadian nanosatellite [20]. It was a 1U CubeSat which validated preliminary nanosatellite design concepts. The subsequent CanX-2 was a 3U, 3.5 kg CubeSat designed for ionospheric profiling, greenhouse gas monitoring, and studying surface degradation of materials exposed to the space environment [21]. CanX-4 and CanX-5 were two 8U, 6 kg CubeSats which demonstrated autonomous dual-spacecraft precision formation flying [22]. The 3U CanX-7 mission featured an Automatic Dependent Surveillance-Broadcast (ADS-B) payload developed by the Royal Military College (RMC) [23], [24] and successfully demonstrated the use of a drag sail for deorbiting [25]. Developed by the National Aeronautics and Space Administration (NASA), the 12U Cislunar Autonomous Positioning System Technology Operations and Navigation Experiment (CAPSTONE) is another notable ongoing CubeSat mission that will validate the performance of autonomous guidance software for navigation and stationkeeping in the cislunar environment in preparation for the upcoming Lunar Gateway mission [15].

1.2.2 Subsystems

As with all spacecraft, the critical subsystems onboard a nanosatellite are Electrical Power System (EPS), Command and Data Handling (CDH), communications, and Guidance, Navigation, and Control (GNC) [2], [8]. The EPS is composed of power generation, storage, and distribution elements: deployable or surface-mounted solar arrays generate power, which is then distributed to the other subsystems or stored in rechargeable batteries. The CDH subsystem is composed of an onboard computer (OBC) that is responsible for monitoring the spacecraft state-of-health, processing and storing incoming data from the payload, and controlling all other subsystems to meet the mission profile. The communications subsystem consists of transceivers and antennas that receive incoming uplinks from the ground support equipment (GSE) and crosslinks from other satellites as well as transmit data via crosslinks and downlinks. GNC systems determine and control the orientation, position, and trajectory of the spacecraft. The Attitude Determination and Control System (ADCS) is the part of GNC which is responsible for orientation sensing and attitude actuation. An ADCS is composed of sensors, e.g., Earth-horizon, Sun, or star sensors or inertial measurement units (IMUs), and actuators, e.g., magnetorquers, reaction wheels, or thrusters. Navigation is achieved with, e.g., Global Positioning System (GPS) receivers or, for interplanetary missions, the Deep Space Network (DSN).

Trajectory control for nanosatellites is achieved via the use of a primary propulsion system, typically chemical or electric. However, as illustrated in Fig. 1.4, only 159 (7.4 percent) of 2138 nanosatellites launched have featured propulsion systems [14]. This disparity can be attributed to the relatively lower technology readiness level (TRL) of most nanosatellite-rated propulsion systems due to the challenge of scaling these systems down to meet nanosatellite SWaP constraints. This has rendered many missions bereft of propulsion capabilities and thus lowers the return these mission can provide.

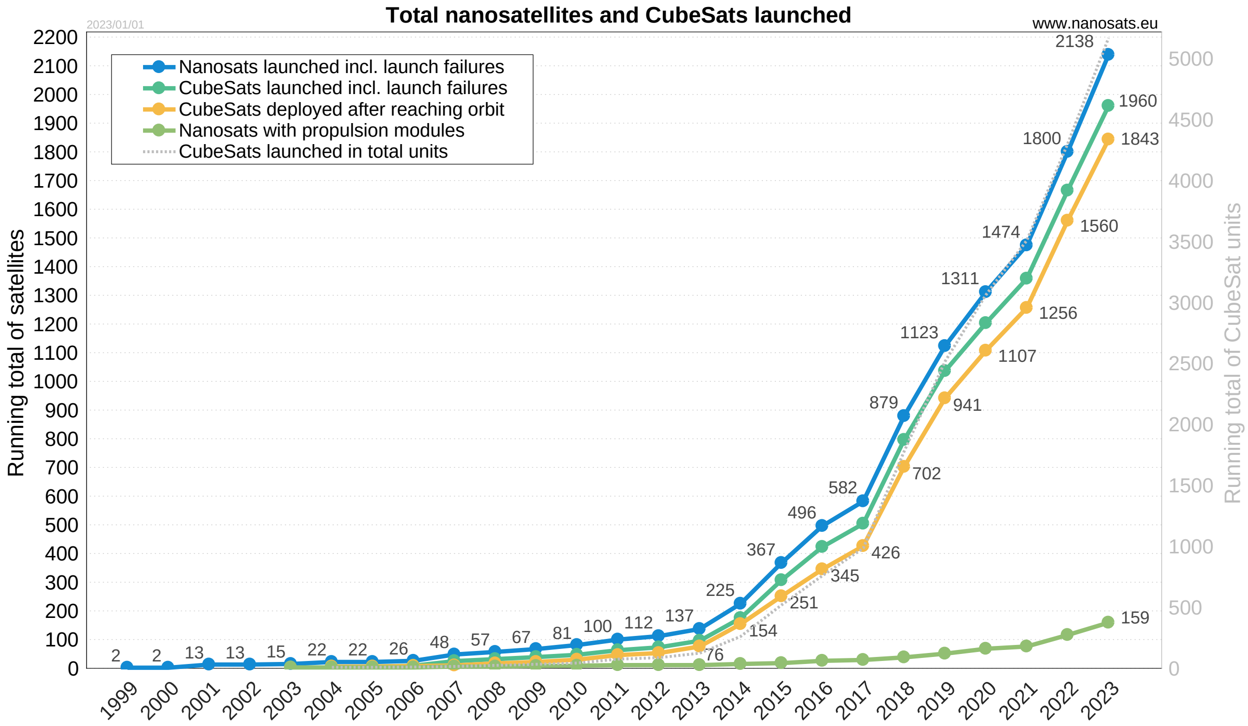

Figure 1.4: Total nanosatellites and CubeSats launched as of Jan 1, 2023 (sourced from [14]).

1.3 Nanosatellite Propulsion Systems

Nanosatellite propulsion systems are a critical enabling technology for next-generation nanosatellite missions [7]. While nanosatellite missions have experienced significant proliferation in recent years, this trend has not been complemented by an abundance of robust and economical propulsion systems [9], [14], which are necessary for missions involving, e.g., autonomous rendezvous and docking (ARVD) operations [5], [6] or formation flying [26]. As such, various organizations have carried out rapid development of novel and advanced propulsion systems for nanosatellites, with many prototypes gaining flight-qualified status and some even developing into commercial products. As with general spacecraft propulsion, nanosatellite propulsion systems can be divided into three major classes: chemical, electric, and propellantless [8], [9]. Within the category of chemical propulsion are monopropellant (MP) and cold gas thrusters. EP systems include electrothermal, electrostatic (ES), and electromagnetic (EM) thrusters, while propellantless systems include solar sails.

1.3.1 Chemical Propulsion

Cold gas propulsion systems provide thrust via the expulsion of a pressurized gas through a conventional supersonic nozzle. These systems typically provide nanosatellites with anywhere from 100 μN to 100 mN of thrust at specific impulse levels of 30 to 75 s and are ideally-suited for nanosatellites due to their low complexity and cost [8], [9]. Indeed, cold gas thrusters were used on the Mars Cube One (MarCO) CubeSat mission, which consisted of two identical 6U CubeSats designed for interplanetary operation at Mars [27]. The propulsion system featured eight 25-mN cold gas thrusters operating with R236fa propellant at 40 s specific impulse to provide reaction wheel desaturation and TCMs. The MarCO satellites were launched in

2018 and successfully relayed data from the NASA Interior Exploration using Seismic Investigations, Geodesy and Heat Transport (InSight) lander during its entry, descent, and landing (EDL) phase [28]. The 3U CanX-2 CubeSat featured a sulfur hexafluoride (SF6) cold gas thruster, referred to as the Nano Propulsion System (NANOPS), that regularly provided 35 mN of thrust at 46 s specific impulse [9]. The NANOPS was later developed into the Canadian Nanosatellite Advanced Propulsion System (CNAPS), which consisted of four similar thrusters and was used onboard the 6U CanX-4/5 mission.

MP thrusters use a metal catalyst to decompose liquid propellant, after which the activated propellant is accelerated through a supersonic nozzle. These systems typically operate at 200 to 235 s of specific impulse for a 1-N-class propulsion system [9]. For example, the Aerojet MR-103 thruster operating at 1 N of thrust and 227 s specific impulse using hydrazine was recently flown onboard microspacecraft [29]. Green monopropellants are currently being investigated to be used as non-toxic fuels with higher thrust density for MP systems. One notable green monopropellant is Advanced Spacecraft Energetic Non-Toxic (ASCENT) [30], a proprietary blend of hydroxylammonium nitrate (HAN). Another notable MP thruster is the Busek BGT-X5 [31], pictured in Fig. 1.5. The Busek BGT-X5 propulsion system has a volume of 1U, a wet mass of 1.5 kg, and may provide up to 660 N s of total impulse using 300 g of ASCENT while operating at a specific impulse of 225 s. The currently-operating 6U Lunar Flashlight CubeSat mission also features four 100-mN ASCENT monopropellant thrusters providing 3300 N s of total impulse [30].

Figure 1.5: Busek BGT-X5 monopropellant thruster (sourced from [31]).

1.3.2 Electric Propulsion

Electrothermal thrusters use electrical power to increase the propellant energy beyond what is achieved via pressurization or combustion, meaning the specific impulse of electrothermal systems is higher than that of their chemical counterparts [8]–[10]. These systems provide anywhere from 10 μN to 500 mN of thrust and have a specific impulse range of 60 to 150 s [9]. Warm gas thrusters are simply cold gas thrusters that use a heating element to energize the emitted cold gas and increase its specific impulse. Resistojets (RJs) use an resistively-heated element embedded directly in a monopropellant or bipropellant engine to raise the propellant temperature, while arcjets (AJs) provide an electrical discharge which weakly ionizes the gaseous propellant. An operational schematic of a RJ is shown in Fig 1.6, where a resistive element is added to the combustion chamber to further heat the propellant prior to its exit via the supersonic nozzle. Finally, electrodeless

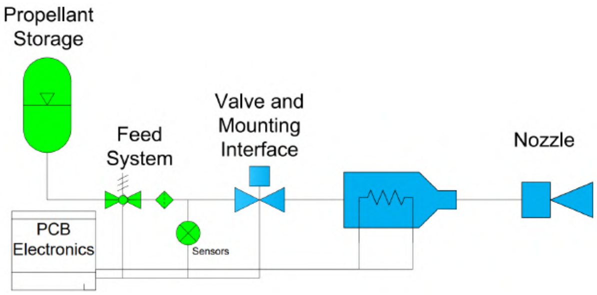

Figure 1.6: Resistoject schematic (sourced from [32]).

electrothermal thrusters provide heating via radio-frequency (RF) or microwave radiation. Electrothermal propulsion systems also have flight heritage. For example, the 1.5U AuroraSat-1 CubeSat mission featured six water-based RJ thrusters that enabled three-axis attitude control and provided a total impulse of 70 N s using 70 g of water propellant [8].

Gridded ion thrusters (GITs) are a type of ES propulsion system that use a set of biased grids to accelerate a strongly ionized gaseous propellant [10]. These devices consist of a cylindrical discharge chamber into which propellant (e.g., xenon) is injected, a set of acceleration grids across which an electrical potential is applied, and an external neutralizer (e.g., hollow cathode). Ionization is achieved via electron bombardment, i.e, direct current (DC) ionization, in which an internal hollow cathode generates high-energy electrons that collide with and ionize neutral propellant, or electrodeless ionization, in which RF or microwave energy is deposited into the propellant. Magnetic circuits may also be included in the design to generate magnetic cusp regions that increase the electron lifetime in the discharge chamber and improve the ionization efficiency. An operational GIT schematic is shown in Fig. 1.7, where the interior anode and screening grid are biased to a large electric potential (kV) and the second grid is grounded. Lunar Ice Cube and LunaH-Map are two 6U CubeSats that were secondary payloads onboard the NASA Artemis I mission and which featured GITs. Busek Ion Thruster (BIT-3) RF GITs were used by each of the CubeSats to provide approximately 1 mN of thrust at 1200 to 2000 s of specific impulse using iodine propellant and operating at 55 to 75 W of input power [8], [9]. At present, neither of the thrusters have successfully been operated, as the LunaH-Map BIT-3 experienced a propellant management system failure, while Lunar IceCube experienced telecommunications challenges [33]. The flight-qualified ThrustMe NPT30-12 RF GIT is another notable system [34]. The NPT30-12 stores solid

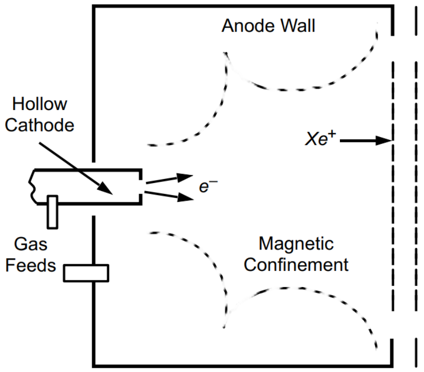

Figure 1.7: GIT schematic (sourced from [10]).

diatomic iodine, which is sublimated and subsequently ionized using RF induction. The thruster operates at a nominal thrust and input power of 0.8 mN and 55 W, respectively, with a specific impulse of up to 2500 s. A schematic of the NPT30-12 is shown in Fig. 1.8.

Electrospray propulsion (ESP) devices are a type of ES propulsion that are arguably one of the most promising propulsion technologies for nanosatellites [7]. As illustrated in Fig. 1.9, a conducting liquid propellant is extracted from a porous emitter via an applied electric potential, and a porous reservoir is used to store propellant. These devices electrostatically accelerate conducting fluids to exceedingly high exit velocities [35], require an input power as low as 1.5 W [9], and are fabricated and packaged in small form factors that easily meet the volume and mass constraints of nanosatellites [36]. Indeed, ESP devices typically do not require propellant management systems, as the liquid propellants used in these devices typically have negligible vapour pressures and thus may simply be stored in a porous medium that is exposed directly to vacuum. This property significantly reduces their footprint and complexity relative to other nanosatellite propulsion systems. Furthermore, electrospray thrusters have extensive flight heritage onboard satellites [8], [9], [37], [38]. For example, electrospray thrusters flew onboard two 1.5U AeroCube-8 CubeSats in 2015, providing 74 μN of thrust at 1150 s of specific impulse [9]. In addition, ESP thrusters developed by ENPULSION have flown onboard over 60 satellites [38], providing 350 μN of thrust and up to 4000 s specific impulse, albeit at a demanding 45 W of input power [39].

HETs are a type of ES propulsion which have gained prevalence in both academia and industry since their inception in the mid-20th century [41]. Theses devices consist of an annular or cylindrical discharge channel, internal neutral gas feed port, internal anode, external cathode that produces electrons, and permanent magnets or electromagnets [42]. Opposing magnetic poles are placed to produce a primarily-transverse magnetic field **B** at the channel exit, which couples with the axial electric field **E** generated by the internal anode and external cathode to induce an azimuthal **E** × **B** electron drift that reduces the axial electron conductivity, thus generating a large localized electric field directly in the plasma. Incoming neutral atoms are

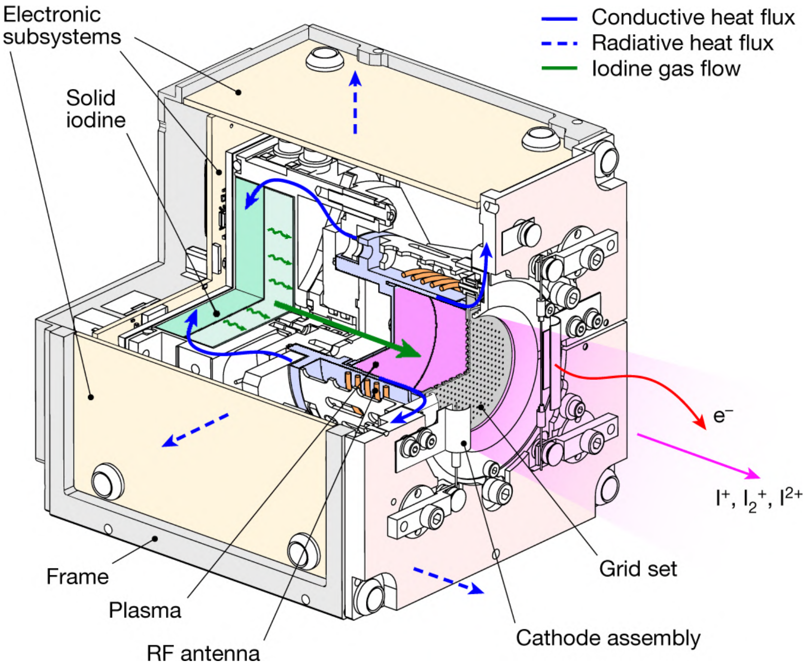

Figure 1.8: ThrustMe NPT30-12 RF GIT schematic (sourced from [34]).

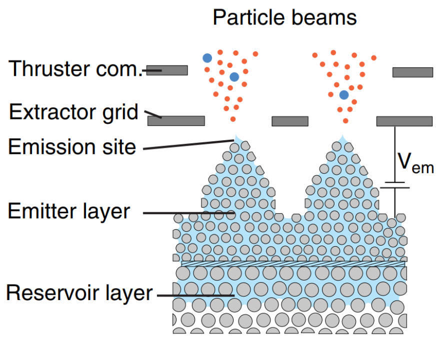

Figure 1.9: ESP schematic (sourced from [40]).

ionized by the upstream electrons and are subsequently accelerated by the downstream electrons to produce thrust. Nanosatellite-rated Hall thrusters typically operate at 10^1 to 10^2 W of input power and produce 1 to 60 mN of thrust at 800 to 1950 s of specific impulse [8], [43]. An operational schematic of a Hall thruster is illustrated in Fig. 1.10. The first flight-qualified CubeSat-rated HET was the Exotrail 50 W permanent magnet HET [44], which was launched and tested in late 2020 and operated using xenon propellant to produce 2.15 to 3.12 mN of thrust on multiple burns.

In pulsed plasma thrusters (PPTs), a type of EM propulsion, a charged capacitor discharges between two electrodes and the resulting arc ablates and ionizes a solid propellant, typically polytetrafluoroethylene (PTFE). The ions are accelerated via their self-induced Lorentz forces [8]–[10]. Vacuum arc thrusters (VATs) are similar to PPTs, though they discharge directly from an ablative cathode, i.e., one electrode is sacrificial and acts as the propellant source. PPTs and VATs are ideally suited for nanosatellites, as they provide high-resolution thrust and attitude control via small and repeatable impulse bits on the order of 1 μN s, have few to no moving parts, and operate from 0.5 W to 50 W [9]. PPTs and VATs also have flight heritage on nanosatellites. The Austrian CubeSat PEGASUS from the University of Applied Sciences Wiener Neustadt (FHWN), launched in June 2017, featured four PPT units. A set of Micro Cathode Arc Thrusters (μCATs) developed by George Washington University (GWU) were flown onboard the 1.5U Ballistic Reinforced Communication Satellite (BRICSat-P) CubeSat mission, providing 20 μN of thrust at 3000 s specific impulse.

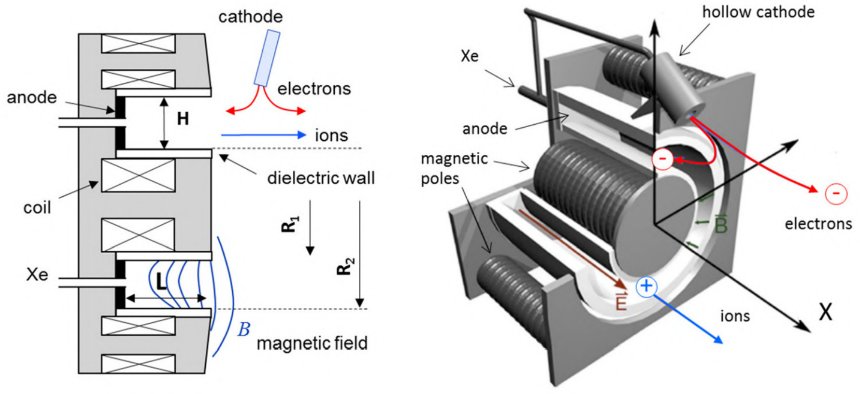

Figure 1.10: HET schematic (sourced from [41]).

1.3.3 Propellantless Propulsion

The most promising form of propellantless propulsion technology is the solar sail propulsion system. Solar sails harness momentum imparted onto an absorptive or reflective surface by solar photons to provide thrust to the spacecraft [9], [45]. Furthermore, solar sails have already successfully been implemented onboard CubeSats, where the LightSail 2 CubeSat mission demonstrated the use of solar sailing for CubeSat trajectory and attitude control [45]. LightSail 2 featured four independent 4.6-μm-thick triangular aluminized Mylar sail sections that totalled to produce a deployed sail area of 32 m^2. The deployment process for the sails is illustrated in Fig. 1.11. The control strategy used to validate the concept involved orienting the sail normal vector parallel to the Sun normal vector when moving away from the Sun and perpendicular to the Sun normal vector when moving towards the Sun, such that the solar radiation pressure would provide an increase to the orbital velocity. This scheme successfully increased the LightSail 2 spacecraft apogee by several kilometers on multiple occasions.

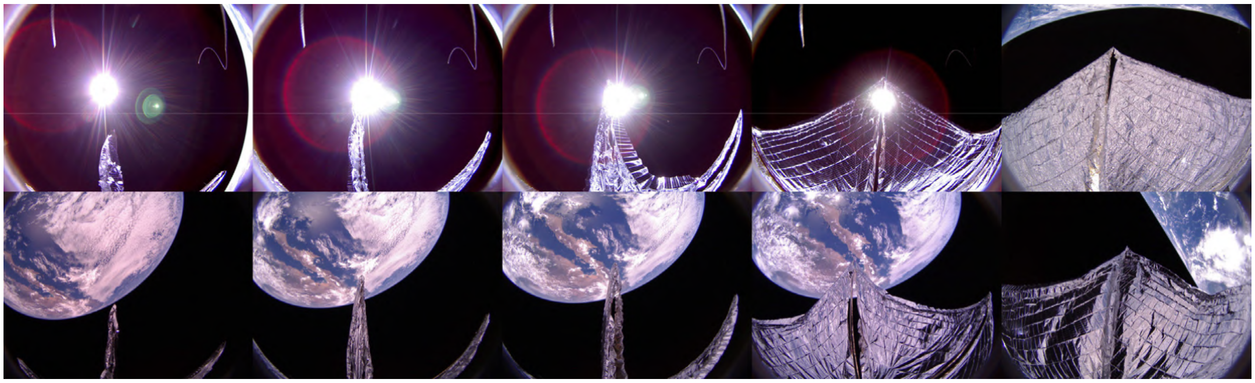

Figure 1.11: LightSail 2 solar sail deployment (sourced from [45]).

1.3.4 System Selection

The advantages of EP over chemical propulsion are best illustrated through an example nanosatellite mission. The estimated performance of cold gas, MP, GIT, ESP, and HET propulsion systems for a 100 m s^{-1} Δv mission profile are tabulated in Table 1.1, where a nanosatellite dry mass of 4 kg is assumed. The propellant mass is calculated using Eq. 1.6 and the burn time is calculated using Eq. 1.7. Evidently, the propellant mass required for the chemical engines is an order of magnitude higher than for the EP systems. Conversely, the Δt for EP systems is an order, or even two orders, of magnitude higher than for chemical engines, making these systems less suited for, as an example, emergency TCMs. Most notably, ESP systems provide the greatest Δv capabilities relative to the other systems due to their high specific impulses.

Table 1.1: Performance parameters of primary nanosatellite propulsion systems, based on a Δv of 100 m s^{-1} and nanosatellite dry mass of 4 kg.

System	T [mN]	I_{sp} [s]	m_{prop} [g]	Δt [hr]	Ref.
Cold gas	35	46	992	3.6	[9]
MP	100	235	177	1.1	[9], [30]
RJ	10	150	281	11	[9]
GIT	1	2500	16	111	[34]
ESP	0.35	4000	10	318	[39]
HET	3	2000	20	37	[8], [44]
PPT	0.02	3000	14	5565	[9]

1.4 Thesis Objective

The objective of this work is to develop an ESP system that provides improved propulsion capabilities for nanosatellites and complements the existing literature on ESP. The thruster is designed to serve as a primary propulsion system while also serving as a mechanism for attitude actuation, which is conducive for optimized attitude and trajectory control. An experimental campaign is carried out to validate the thruster mechanical and electrical designs as well as to characterize the thruster performance, while modeling of the electrospray emission profile is used to estimate the thruster performance and inform the thruster design.

1.4.1 Thesis Organization

Chapter 1 provided an overview of spacecraft propulsion and nanosatellites and outlined existing nanosatellite propulsion systems. Chapter 2 is an in-depth review of the theory, design, modeling, experimental characterization, and flight heritage of existing ESP systems. Chapters 3 to 6 are dedicated to the design, modeling, experimental characterization, and performance analysis of the electrospray thruster developed in this work. Chapter 7 concludes this work. Appendix A provides low-level details of the thruster electrical design.

2 Electrospray Propulsion

Recent advances in microelectromechanical systems (MEMS) manufacturing techniques have contributed to the rapid development of ESP devices [46]–[48]. These devices provide high-resolution attitude and trajectory control capabilities for nanosatellites [49]. They are characterized by their high specific impulse (1000 to 5000 s) [35], [50], high theoretical efficiency (up to 90 percent) [51], superior thrust precision (nN to μN) [26], relatively high Δv capabilities (hundreds of m s^{-1}) [46], as well as their small form factor (mm to cm) [52]. As shown in Chapter 1, ESP devices offer superior performance relative to other nanosatellite propulsion systems due to their high specific impulse, and as will be discussed in this chapter, their exceptional miniaturization capabilities and low power requirements allow them to effectively meet nanosatellite SWaP constraints.

2.1 ESP Overview

ESP devices operate on the electrospray phenomenon: the spraying of a fluid due to an applied ES force. These devices use a strong electric field to extract, accelerate, and emit a conductive liquid propellant. The electric field formed by the potential difference between the emitter and an extractor electrode causes the propellant surface to deform into the characteristic Taylor cone, the apex of which generates charged particles in the form of droplets or ions [53].

2.1.1 Emission Modes

The three types of electrospray emitters are internally fed, externally wetted, and porous [55]. These configurations are illustrated in Fig. 2.1. The traditional internally fed emitters require a pressurized feed system to deliver propellant to the capillary port, where the capillary typically has a diameter below 100 μm. For externally wetted emitters, the propellant spans a surface and is passively fed to the emission site. Porous emitters use capillary action to passively transport propellant to the emitter tip. Regardless of the

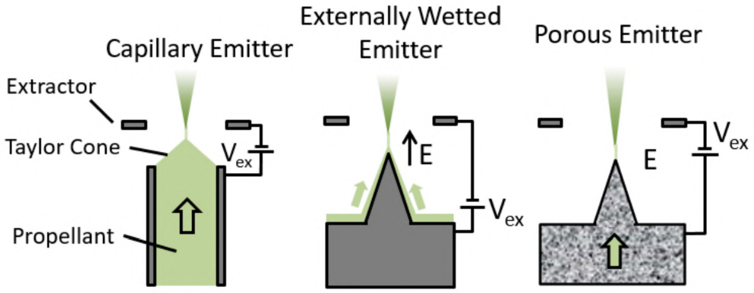

Figure 2.1: ESP emitter configurations: internally fed, externally wetted, and porous (sourced from [54]).

emitter type, the thrust produced by a single Taylor cone is only on the order of tens to hundreds of nN [50]. To achieve the practical thrust levels required for propulsive maneuvers, arrays of individual emitters are fabricated along the thrust plane. This enables the formation of hundreds to thousands of emission sites per square centimeter and this configuration is referred to as multiplexed electrospray. It is also common to couple emitters to a more voluminous propellant reservoir that increases the total propellant stored in and thus total Δv delivered by the thruster.

The competing forces that dictate the emission mode are illustrated in Fig. 2.2. As will be presented in subsequent sections, parameters such as the magnitude of the ES force, hydraulic impedance of the emitter, propellant conductivity, and propellant viscosity determine whether the thruster operates in droplet (colloid) mode or in the purely ionic regime (PIR). Droplets have relatively low charge-to-mass (specific charge) ratios, making droplet mode ideal for high-thrust maneuvers, whereas PIR, which emits ions with a significantly higher charge-to-mass ratio, is well-suited for maneuvers and missions requiring high specific impulse. The PIR is achieved with a relatively higher voltage and lower flow rate and approaches performance in excess of 5550 s specific impulse and 90 percent theoretical efficiency [35], [52], [56].

Beam quasineutrality is achieved by emitting positively and negatively charged particles in tandem or in succession [57]. Maintaining beam quasineutrality is critical for preventing spacecraft charging and for mitigating thruster inefficiencies due to space charging effects [58]. An optional accelerator electrode may also be included in the design to decouple the extraction and acceleration mechanisms [59]. In such a configuration, the voltage between the emitter and extractor electrode is kept constant, while the accelerator electrode voltage is varied to provide finer throttling control.

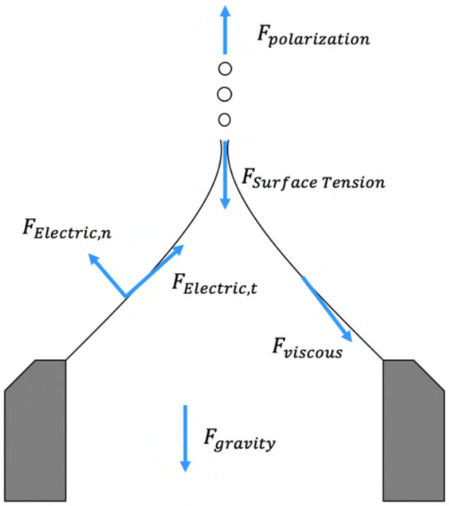

Figure 2.2: Schematic of competing forces within a Taylor cone (sourced from [60]).

2.1.2 History of ESP

Preliminary research into the electrospray phenomenon dates back to 1882 [3], when Lord Rayleigh derived a simple analytical expression to describe the maximum charge a liquid droplet can sustain before electrospray emission occurs [61]. This expression, known as the Rayleigh limit, is found by equating the electric pressure

P_E of a point charge to the Young-Laplace (capillary) pressure P_γ of a droplet:

$$P_E = P_\gamma \tag{2.1}$$

$$\frac{1}{2}\epsilon_0 \left(\frac{q_{\text{drop}}}{4\pi\epsilon_0 R_{\text{drop}}^2} \right)^2 = \frac{2\gamma}{R_{\text{drop}}}, \tag{2.2}$$

in which ϵ_0 is vacuum electrical permittivity, q_{drop} is the droplet charge, R_{drop} is the droplet radius, and γ is the liquid surface tension coefficient, leading to

$$q_{\text{drop}}^2 = 64\pi^2\gamma\epsilon_0 R_{\text{drop}}^3. \tag{2.3}$$

Further research into electrospray was conducted in the early 1900s by Zeleny [62], who investigated the impact of flow rates and electric fields on emission modes, in the mid 1900s by Taylor [63], who derived the characteristic Taylor cone angle of 49.3 degrees, and in the late 1900s by de la Mora [64], who identified the minimum flow rate required to sustain a Taylor cone-jet:

$$Q_{\text{min}} = \frac{\gamma\epsilon_{\text{r}}\epsilon_0}{\rho\sigma_{\text{e}}}, \tag{2.4}$$

in which ϵ_{r} is the relative electrical permittivity and σ_{e} is the fluid electrical conductivity.

Applied research and development of ESP systems began in the early 1960s and lasted until the early 1970s [3], [65]. Glycerol-based propellants were used to operate colloid thrusters for 100s of hours and in arrayed configurations, with time-of-flight (ToF) mass spectrometry (MS) measurements even being performed [66]. The United States and Europe both continued development of ESP devices with performance specifications comparable to the devices of today; however, due to the exceedingly high voltages (> 10 kV) required for operation and with MEMS manufacturing techniques still emerging, ESP was paused to focus on the more promising GIT and HET technologies. It was not until the 1990s that research into ESP was revitalized due to the maturation of the MEMS industry and development of the promising ionic liquid (IL) propellants. The 1990s also saw renewed interest in field emission ion sources, which led to the development of field emission electric propulsion (FEEP), a subclass of ESP which uses liquid metal propellant and operates strictly in the PIR [67], [68]. FEEP devices typically operate at relatively high specific impulses, but only extract cations and thus require external electron sources to ensure beam quasineutrality.

ESP research of the current century ultimately culminated in the application of ESP onboard the Laser Interferometry Space Antenna (LISA) Pathfinder mission [37]. Two clusters of four Colloid Micro-Newton Thruster (CMNT) systems which provided 5 to 30 μN at 150 to 240 s specific impulse to the Disturbance Reduction System (DRS) were used to counteract small disturbance forces on the order of 10^{-6} N. The CMNTs used 1-ethyl-3-methylimidazolium bis(trifluoromethylsulfonyl)imide (EMI-Im) IL propellant [69].

2.1.3 Propellants

One of the most common propellants currently used by electrospray thrusters are ILs—also known as molten salts—which are composed of positively and negatively charged molecules that mix together to form a quasineutral, inert, low off-gassing, and conducting fluid at ambient temperatures. Indeed, ILs typically exhibit zero vapour pressure, making them ideally suited for space applications as they will not offgas into the nanosatellite and near-satellite environment [58]. However, the disadvantage of ILs is that the molecular species contain complex internal degrees of freedom [70], resulting in an extended energy distribution function and reducing the overall efficiency of the thruster. One of the most common IL propellants used in ESP is 1-ethyl-3-methylimidazolium tetrafluoroborate (EMI-BF4). The mass properties of the first four EMI-BF4 ionic species are tabulated in Table 2.1. Other notable ESP propellants include 1-ethyl-3-methylimidazolium gallium tetrachloride (EMI-GaCl4) and 1-butyl-3-methylimidazolium iron tetrabromide (BMI-FeBr4).

Table 2.1: Mass properties of EMI-BF4.

	$[\text{EMI-BF4}]_n$ EMI^+				$[\text{EMI-BF4}]_n$ BF4^-			
n	0	1	2	3	0	1	2	3
Mass [amu]	111	309	507	705	87	285	483	681

2.1.4 Performance Relations

The performance of electrospray thrusters is governed primary by the specific charge q_{sp} distribution of the emitted propellant:

$$\langle q_{\text{sp}} \rangle = \frac{I_{\text{emit}}}{\dot{m}_{\text{prop}}}, \tag{2.5}$$

in which I_{emit} is the emitted current. The exit velocity of the emitted ions can be approximated as

$$v_{\text{exit}} = \left(2 q_{\text{sp}} V_{\text{in}}\right)^{1/2}, \tag{2.6}$$

where V_{in} is the applied voltage. This leads to the expression for the thrust,

$$T = I_{\text{emit}} \left(\frac{2V_{\text{in}}}{q_{\text{sp}}}\right)^{1/2}, \tag{2.7}$$

as well as the specific impulse,

$$I_{\text{sp}} = \frac{\left(2 q_{\text{sp}} V_{\text{in}}\right)^{1/2}}{g_0}. \tag{2.8}$$

As will be discussed, the emitted beam is typically not monoenergetic due to the presence of ions with varying specific charges [70]. The performance of an electrospray thruster with a distribution of specific charges is further characterized by its polydispersive efficiency,

$$\eta_{\text{poly}} = \frac{\left(\sum_i I_i / q_{\text{sp},i}\right)^2}{\left(\sum_i I_i / q_{\text{sp},i}\right) I_{\text{total}}}, \tag{2.9}$$

where I_i is the current associated with specific charge $q_{\text{sp},i}$ and I_{total} is the total emitted current.

Knowledge of the total emitted current, specific charge, and exit velocity allows for the calculation of the torque generated by each emitter for a nanosatellite. The torque is calculated as $\tau = L_\tau T = I_\tau \dot{\omega}$, in which L_τ is the lever length, I_τ is the nanosatellite moment of inertia, and $\dot{\omega}$ is the angular acceleration. The change in angular velocity based on the total emitted current for a given operating duration Δt is thus:

$$\Delta\omega = T \frac{L_\tau}{I_\tau} \Delta t = I_{\text{total}} \left(\frac{2V_{\text{in}}}{q_{\text{sp}}}\right)^{1/2} \frac{L_\tau}{I_\tau} \Delta t. \tag{2.10}$$

This process is illustrated in Fig. 2.3, where an electrospray thruster with two emitters provides attitude actuation to a 1U CubeSat. One of the emitters produces a stronger beam for a period Δt, which produces a torque on the spacecraft and causes it to rotate at an angular rate of $\Delta\omega$.

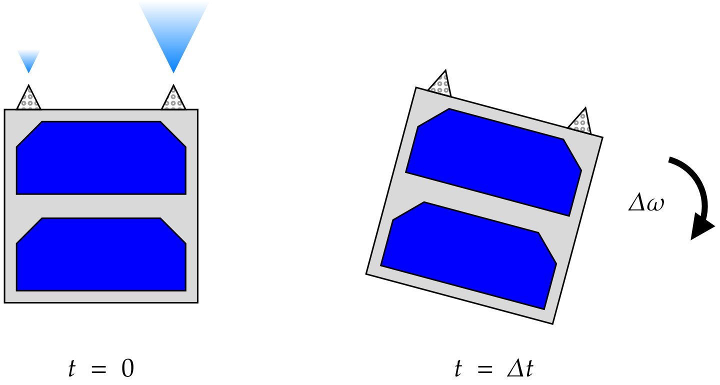

Figure 2.3: Attitude actuation for a 1U CubeSat using ESP.

One of the primary advantages of ESP devices is that the theoretical thrust density of ESP typically exceeds that of other EP systems, such as traditional GITs. In all gridded ES propulsion systems, the thrust density is proportional to the space charge limited current density J, which is dictated by the Child-Langmuir law [10]:

$$J = \frac{4\epsilon_0}{9} \left(2q_{\text{sp}}\right)^{1/2} \frac{V_{\text{in}}^{3/2}}{D^2}, \tag{2.11}$$

in which D is the distance between the accelerating electrodes. The ratio of GIT and ESP current densities can thus be expressed as:

$$\frac{J_{\text{ESP}}}{J_{\text{GIT}}} \approx \left(\frac{V_{\text{in,ESP}}}{V_{\text{in,GIT}}}\right)^{3/2} \left(\frac{D_{\text{GIT}}}{D_{\text{ESP}}}\right)^{2}. \tag{2.12}$$

The extractor distance for ESP is on the order of 100 μm, whereas the extractor distance for GITs is on the order of 1 mm, suggesting that the achievable space charge limited current density of ESP is 100 times higher than that of GITs for any given accelerating voltage [71].

2.1.5 Performance Mechanisms

The primary challenge found in electrospray thrusters is mitigating impingement of the emission plume on the extractor and accelerator grids [72]. This reduces the total emitted current and thus the total thrust produced. In addition, propellant collected on the extractor electrode can backspray onto the emitter: the continuous overspray and backspray is an efficiency loss mechanism and can lead to propellant bridging and subsequent short-circuiting. Short-circuiting is one of the most common end-of-life (EOL) mechanisms and can result in complete destruction of individual emitters [36].

As discussed, IL are quasineutral molecular fluids, and while they have many advantages, the presence of multiple ionic species in the plume decreases the overall performance of electrospray thrusters: due to the fact that different ionic masses are accelerated to different final velocities, the polydispersive efficiency is decreased [70]. One of the leading causes of ionic species distributions is fragmentation, which is when IL clusters solvate into smaller ions (i.e., monomers, dimers, etc.) and a larger neutral cluster. While the smaller ion is further accelerated, the neutral cluster follows a ballistic trajectory at a lower exit velocity and therefore decreases the overall specific impulse.

2.1.6 Diagnostics

Electrospray thruster performance is typically characterized using ToF MS [50], [52], [53], [73], retarding potential analyzers (RPAs) [50], torsional thrust balances [48], [52], [74], magnetically-levitated platforms with optical angular decoders [26], wire probes [75], high-speed video microscopy [72], and quartz crystal microbalances (QCMs) [76]. These methods may be categorized into direct measurement methods, such as torsional thrust stands, and indirect measurement methods, such as ToF. Direct and indirect measurements are often used to complement one another [52], though one of the primary challenges in ESP diagnostics is reconciling the differences between direct and indirect measurement profiles [76].

The most basic properties of interest are the operational voltage and the current draw and emission of each emitter [76]. The high voltage (HV) delivered to each emitter can be measured with HV probes or voltage dividers (VDs), while a shunt resistor (SR) may be used to determine the current being delivered directly to each emitter. A schematic of a HV rail with a VD and SR is shown in Fig. 2.4, where V_{VD} is the output VD measurement relative to ground and V_{SR1} and V_{SR2} return the voltage measurement across the SR based on Ohm's law, $V = IR$. The VD output is calculated as,

$$V_{\mathrm{VD}} = V_{\mathrm{in}} \frac{R_2}{R_1 + R_2}, \tag{2.13}$$

therefore the VD in Fig. 2.4 divides the HV signal by a factor of approximately 10^4. Current intercepted by the extractor electrode is typically also measured and subtracted from the emitter current draw to determine the emission interception fraction, and finally the emitted current that is actually expelled from the thruster can be measured with, e.g., a Faraday cup connected to an ammeter. Regarding the emitted current measurements, full-beam measurements that capture all of the expelled current or partial-beam measurements that measure a small fraction of the expelled current may be performed.

The thrust produced by ESP devices is a critical figure of merit. The thrust can be measured directly using, e.g., torsional thrust stands and mass balances, or it can be indirectly measured using the ToF method. An operational schematic of a torsional thrust stand is shown in Fig. 2.5, where a displacement sensor measures the displacement Δx of a moment arm due to a thrust T [74]. The electrostatic fins are used for in-situ calibration and the magnet is used for damping high-frequency oscillations. Magnetically-levitated nanosatellite platforms which experience angular displacement have also been used to infer thrust [26]. The mass flow rate is another critical figure of merit, as it can be coupled with measurements of the thrust to determine the specific impulse of the thruster (Eq. 1.3). Capillary emitters may use bubble tracking to

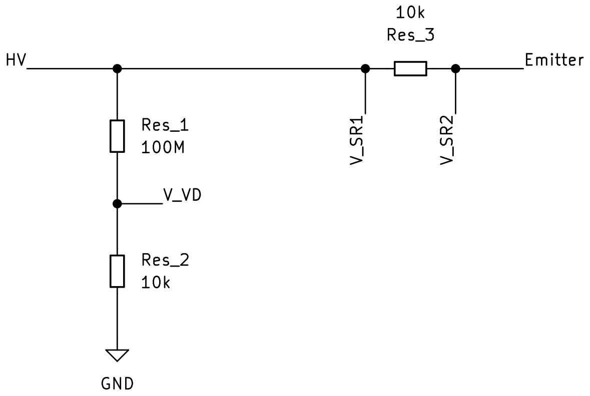

Figure 2.4: Schematic of VD and SR for a HV electrospray rail.

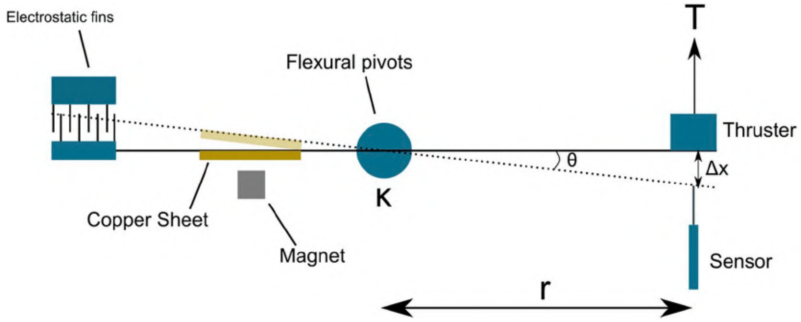

Figure 2.5: Top view schematic of a torsional thrust balance (sourced from [74]).

measure flow rates, while porous substrates are opaque, so their mass flow rates may only be inferred from mass loss during operation. The mass flow rate is one of the most challenging variables to measure in ESP, as the mass flow rate per emitter can be on the order of 1 ng s^{-1} [76].

Due to the fact that the electrospray beam may contain neutral species, instruments which measure only the current (e.g., Faraday cups), are insufficient for fully characterizing the thruster. QCMs are used in ESP to measure the total mass flux emitted by the thruster [76]. A QCM contains an oscillating quartz crystal which resonates at a frequency determined by the total accumulated mass on the collector plate. The signal from a second shielded QCM placed in tandem with the collecting QCM may be subtracted from the collecting QCM for greater accuracy. One QCM drawback is that mass accumulated on the collector plate surface may be dislodged due to high energy particle bombardment, introducing measurement inaccuracies.

The stopping potential of emitted ions is an important plume property and can be characterized with an RPA, which consists of two outer grounded grids and a set of inner biased grids all mounted upstream of a Faraday cup [76]. The inner grids are biased to a particular HV setting such that only particles with a stopping potential greater than the biasing voltage are transmitted. An RPA sweep may be performed to determine the electrospray beam energy distribution.

ToF MS is commonly used in the ESP community to indirectly measure the thrust and specific impulse. Similar to the RPA, ToF uses outer grounded grids and inner biased grids upstream of a Faraday cup, though in ToF the Faraday cup is placed at a large fixed distance away from the grid assembly, as shown in Fig. 2.6. The biased grids are activated and interrupt the flow of the electrospray plume and the specific charge of the beam can be inferred from the flight time, defined as:

$$t_{\mathrm{ToF}} = D_{\mathrm{ToF}} \left(2 q_{\mathrm{sp}} V_{\mathrm{in}}\right)^{-1/2}, \tag{2.14}$$

in which D_{ToF} is the flight distance. The ToF trace can then be integrated to determine the thrust

$$T_{\mathrm{ToF}} = -\frac{2|V_{\mathrm{in}}|}{D_{\mathrm{ToF}}} \int_0^\infty t \frac{dI(t)}{dt} dt, \tag{2.15}$$

and the mass flow rate

$$\dot{m}_{\mathrm{prop}} = -\frac{2V_{\mathrm{in}}}{D_{\mathrm{ToF}}} \int_0^\infty t^2 \frac{dI(t)}{dt} dt. \tag{2.16}$$

Nondimensional modifiers that account for cluster fragmentation may also be included in Eqs. 2.15 and 2.16. A sample ToF trace for the École Polytechnique Fédérale de Lausanne (EPFL) thruster using EMI-BF4 propellant [52] is shown in Fig. 2.7.

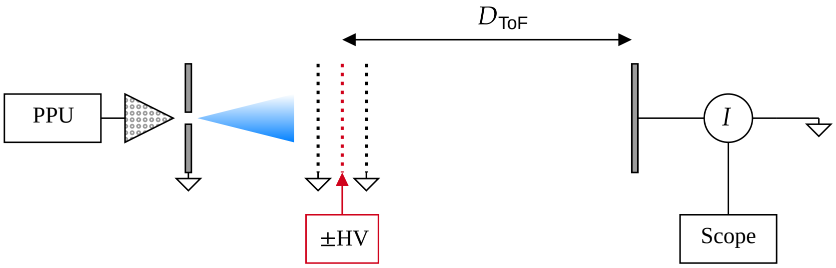

Figure 2.6: ToF diagnostic method schematic.

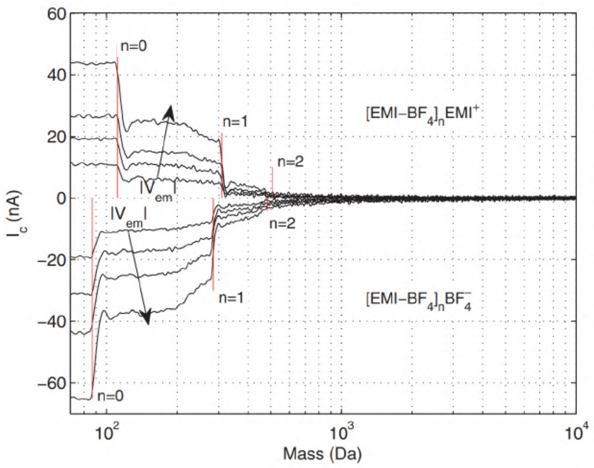

Figure 2.7: Sample ToF data for the EPFL thruster using EMI-BF4 propellant (sourced from [52]).

2.2 Porous ESP

ESP devices using porous emitters have the distinct advantage of only requiring a monolith substrate to provide both the propellant reservoir and the emission source. This reduces the size and complexity of the design by removing the need for additional propellant management systems, as seen with traditional capillary emitters. Porous emitter materials are typically borosilicate glass [52], carbon xerogels [77], [78], and metals [71]. The geometries can be pyramids [79], cones [80], needles [81], wedges [82], or comb-like slices [71]. Porous substrates with large pore sizes (40 to 250 μm) give rise to droplet emission while substrates with small pore sizes (0.5 to 40 μm) give rise to ion emission [71], [75], [82], [83]. Figure 2.8 shows a close-up image of a NanoFEEP porous tungsten emitter with a radius of 0.8 μm, fabricated using Micro-powder injection moulding (μPIM) and sharpened using electrochemical etching [84]. Electrospray thrusters employing arrays of linear porous wedge (prism) emitters have recently gained attention as viable candidates for nanosatellite propulsion systems [50], [52], [53], [56], [82], [83], [85]. The linear porous wedge is a strip of porous substrate at the apex of which multiplexed emission can be observed. Porous wedge emitters are most commonly manufactured from commercially-available sintered borosilicate glass discs [79], which are categorized according to their pore sizes, from P0 (205-μm-diameter) down to P5 (1.3-μm-diameter) [83].

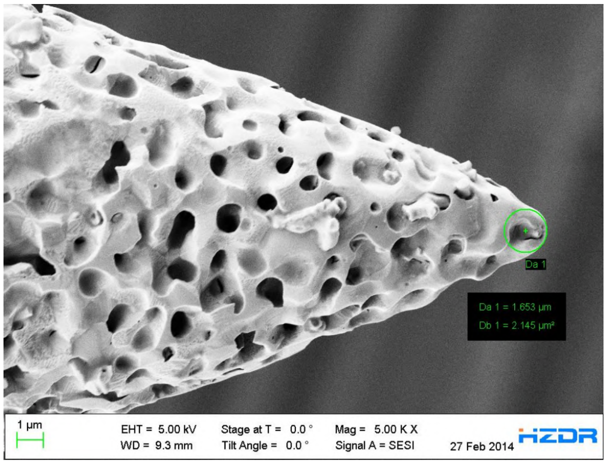

Figure 2.8: NanoFEEP porous tungsten emitter (sourced from [84]).

2.2.1 Porous Flow

Laminar flow through a porous medium (substrate) is described by Darcy's law for low Reynolds number ($Re < 1$):

$$\mathbf{Q}_{\text{por}} = -\frac{k}{\mu}\nabla P, \tag{2.17}$$

where $\mathbf{Q}_{\text{por}}$ is the volumetric flux, k is the substrate permeability, μ is the fluid dynamic viscosity, and P is the fluid pressure. The Reynolds number is described by $Re = \rho u d/\mu$, where ρ is the fluid density, u is the fluid velocity, and d is the porous particle size. The fluid velocity u is related to the volumetric flux via $u = Q_{\text{por}}/\phi$, in which ϕ is the porosity. The porosity characterizes the extended path that the fluid must take within a porous medium: the path in a low-porosity material is more convoluted and thus the fluid must travel with a greater velocity to sustain a given volumetric flux, whereas in a highly-porous medium u approaches q_{por} as ϕ approaches unity. The permeability is related to the porosity and pore radius R_{por} via $k = \phi R_{\text{por}}^2/8$ [80]. The interfacial pressure drop across the fluid meniscus is described by:

$$P_{\text{int}} = P_{\text{men}} - QZ, \tag{2.18}$$

in which P_{men} is the upstream back pressure provided by the reservoir meniscus of radius R_{res}, Q is the volumetric flow rate, and Z is the hydraulic resistance [83]. The back pressure for concave menisci exposed to vacuum is approximated by the Young-Laplace equation:

$$\Delta P_{\text{men}} \approx -\frac{2\gamma}{R_{\text{res}}}. \tag{2.19}$$

Courtney and Shea [83] investigated the influence of porous reservoir permeability on beam composition. The experiment coupled an unchanged Duran Group P5-grade (1.0 to 1.6 μm pores) sintered borosilicate glass wedge emitter to reservoirs of varying porosity grades. Such a configuration is illustrated in Fig. 1.9, where a porous emitter with smaller pore sizes is coupled to a reservoir with larger pore sizes. It was shown that reservoirs with large pores and low Laplace back pressure generate droplet-dominated beams, while reservoirs with small pores and high Laplace back pressure produce ion-dominated beams. Wright and Wirz [82] developed an analytical model to examine the behaviour and spacing of multiplexed emission along a porous wedge. It was proposed that emission sites separated by 50 to 300 μm arise naturally due to pressure and electric field variations. As the uniform upstream flow approaches the wedge apex, oscillatory separation of the flow and irregularities in the substrate cause individual flow cells to form, giving rise to pressure stagnation points further downstream. This results in flow and charge concentrations that contribute to the formation of hundreds of discrete emission sites per wedge. Such emission patterns have been experimentally observed by multiple groups [52], [75], [85], demonstrating the impact of the substrate porous properties on ESP performance.

Contrary to the standard theory that a decrease in pore size would lead to a higher hydraulic impedance and thus more ionic emission, Ma et al. [35] measured a higher specific charge using P4-grade emitters compared to P5-grade emitters. Based on ToF curves for P4-1-tip, P4-25-tip, P4-100-tip, and P5-100-tip emitters, Ma et al. [35] found an average specific mass flow rate of 1.38×10^{-6} kg s^{-1} A^{-1} for the P4-grade emitters and an average specific mass flow rate of 2.49×10^{-6} kg s^{-1} A^{-1} for the P5-grade emitter. Taking the inverse of the specific mass flow rate, an average specific charge of 725,689 C kg^{-1} is calculated for the P4-grade emitters, while an average specific charge of 402,145 C kg^{-1} is calculated for the P5-grade emitter. Indeed, the highest computed specific impulse, based on the ToF curves, was 6938 s for the P4-grade emitters, but only 4234 s for the P5-grade emitter.

Notably, porous substrates have one distinct disadvantage in that the distribution of pore spacing and radii leads to unpredictable and uncontrollable emission site position and spacing. For example, Dressler et al. [80] developed spatially resolved emission current density maps as a function of the extraction voltage for porous P5-grade conical emitters operating with EMI-Im and observed that the number of off-axis emission sites increased as a function of the applied voltage. Indeed, multiple Taylor cones can be formed on emitter tips where the curvature is significantly larger than the average pore size. Wright et al. [75] used axial and radial wire probe measurements to characterized the emission site spacing of the electrochemically-etched Porous Tungsten Electrospray Emitter (PoWEE) operating with EMI-Im propellant. The axial current measurements as a function of the applied voltage are illustrated in Fig. 2.9. Evidently, there is significant nonuniformity in the emission profile, highlighting the inherent disadvantage of porous ESP devices.

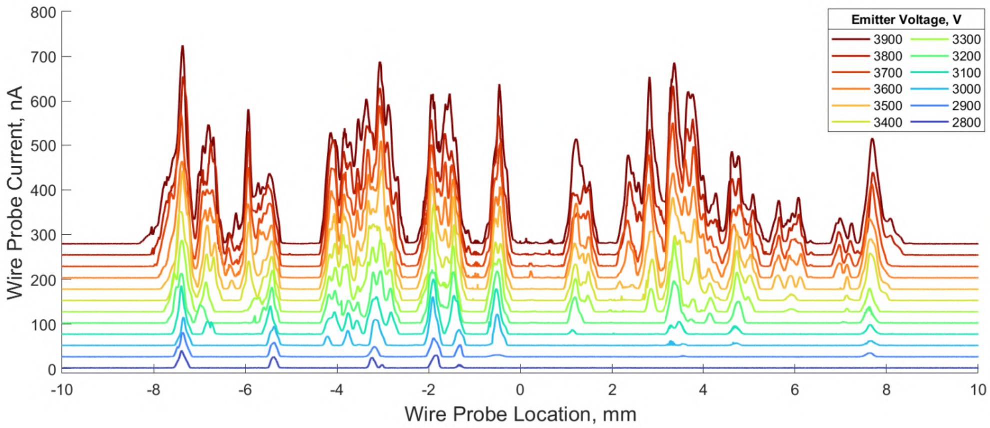

Figure 2.9: Axial wire probe current measurements of the PoWEE thruster (sourced from [75]).

2.2.2 Thrusters Using Porous Substrates

Table 2.2 provides a list of notable electrospray thrusters which employ porous substrates, including the Ionic Electrospray Propulsion System (iEPS), Scalable iEPS (SiEPS), the EPFL thruster, ENPULSION NANO AR3, Porous-emitter Electrospray Thruster (PET), Busek Electrospray Thruster (BET), Air Force

Electrospray Thruster (AFET), and the Modular Ionic Liquid Electrospray Thruster (MILET).

The iEPS, developed by the Massachusetts Institute of Technology (MIT), features 480 conical borosilicate emitter tips situated above a 1 mL reservoir tank and packaged in a volume of 14 mm × 14 mm × 14 mm, with a wet mass of 3.5 g [36]. The SiEPS (Fig. 2.10), a descendant of the iEPS, features eight iEPS modules arranged in parallel along the nanosatellite propulsion plane. An SiEPS prototype was successfully flown onboard the AeroCube-8 CubeSat mission in 2015 [9] and the iEPS concept was eventually used as the foundation for the commercial Tiled Ionic Liquid Electrospray (TILE) thruster developed by Accion Systems [91]. The ENPULSION NANO series was successfully demonstrated in orbit in 2019, and since has been flown on over 60 satellites [38].

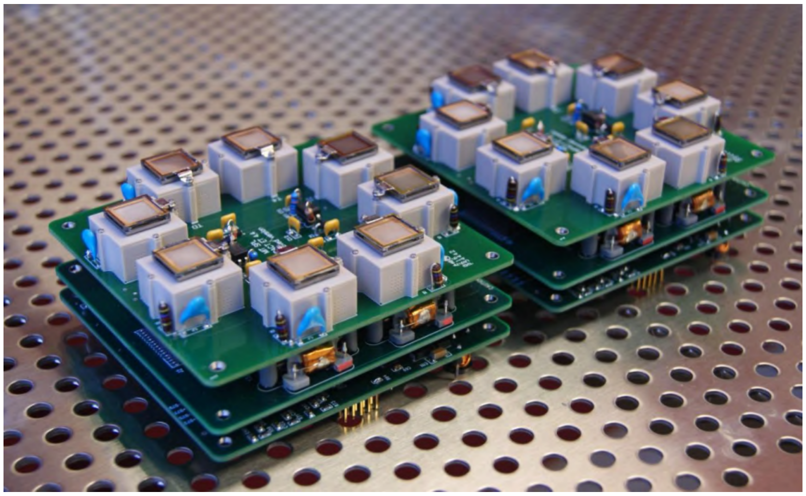

Figure 2.10: MIT SiEPS modules (sourced from [46]).

Table 2.2: Porous ESP systems and their performance specifications.

ESP System	Configuration	Propellant	T [μN]	I_{sp} [s]	Ref.
iEPS	Borosilicate cones	EMI-BF4	12	760	[46]
SiEPS	Borosilicate cones	EMI-BF4	82	1717	[36], [86]
EPFL	Borosilicate wedges	EMI-BF4	20	3260	[52]
NANO AR3	Tungsten needles	Indium	100 to 400	2000 to 6000	[81], [87]
PET-100	Borosilicate cones	EMI-BF4	11 to 221	2733 to 5551	[35]
BET-300-P	Wedges	EMI-IM	5 to 150	840 to 1050	[69]
AFET	Borosilicate pyramids	EMI-BF4	39	1436	[79], [88]
MILET	Nickel cones	EMI-BF4	1 to 23	1263	[89], [90]

2.2.3 Fabrication

Porous ESP emitters are typically fabricated using laser ablation [48], computer numerical control (CNC) micromilling [52], [56], and electrochemical etching [75]. The advantages of laser ablation and electrochemical etching are that these MEMS techniques are used to build devices with dimensions on the order of nanometers and often in large arrays or batches, and result in precise ESP emitters. However, these techniques are often highly cost- and time-intensive as well as complex, making them impractical for rapid prototyping. Conventional CNC milling has the advantage of requiring little fabrication time and expenses and has been shown to yield emitter tips comparable to those obtained by, e.g., laser ablation [52]. Regardless of the fabrication method, the ultimate objectives are to produce sharp and uniform tips and to maintain a tight tolerance across arrayed emitters.

Little and Jugroot [48] used an Oxford Series A 400 Hz diode-pumped solid-state (DPSS) picosecond laser with a resolution of 10 μm for micromilling P5-grade porous wedge emitters and molybdenum extractor electrode films. The emitter wedge was milled using 12-to-13-μm-deep cuts of increasingly larger rectangular dimensions to form a quasi-continuous slope. It was found that milling the prism first would result in stalagmite-like protrusions from debris masking, thus all surrounding material was ablated first prior to the fabrication of the emitter. Reddy et al. [47] used wet isotropic etching to fabricate self-aligned gates for a FEEP thruster array. A silicon-nitride mask was deposited onto a silicon emitter substrate and isotropically etched with hydrofluoric, nitric, and acetic acid (HNA) to produce emitter tips with radii of 50 nm. A 25-μm-thick insulating layer was then applied using photolithography, followed by a deposition of titanium-gold film for the extractor electrode. Natisin et al. [79] used conventional CNC milling to fabricate the AFET-2 borosilicate emitters and housing. Tapered end carbide tools and high spindle speeds of 50,000 rotations-per-minute (RPM) were used to produce tips with radii of curvature of 10 to 20 μm.

2.3 Thrust Vector Control

Next-generation ARVD operations [5], [6], [92], nanosatellite constellations [26], laser communication transmitters [26], [93], and space-based gravitational wave detectors [69], [72], [94] will require high-resolution linear impulse and torque bits for precise attitude and trajectory control. With few exceptions, nanosatellite attitude actuation is achieved primarily with reaction wheels and magnetorquers to accuracies of 0.015 to 1 degrees [2], [8], [26], [93]. Propulsion systems employing high-resolution thrust vector control (TVC) thus offer increased capabilities for nanosatellite missions. They can be used for multi-axis attitude actuation and linear impulse control or for unloading reaction wheels [2], [95]. The increased overlap of the propulsion and attitude control systems is conducive for optimized attitude and trajectory control as it serves to minimize propellant usage and improve the overall efficiency of the spacecraft.

2.3.1 ES Deflection

In ES propulsion systems, the traditional method of TVC is ES plume deflection in the form of segmented or laterally-translated electrodes [95]. ES thrust vectoring for ESP was demonstrated as early as 1968, when deflecting electrodes were used to produce transverse thrust from an array of colloid beams [66]. More recently, thrust vectoring has been implemented by ENPULSION in their commercial NANO AR3 field emission thruster, in which three segmented electrodes provide transverse potential differentials that deflect evaporated indium propellant [38], [81], [87]. The NANO AR3 thruster and optical images of its plume during operation are shown in Fig. 2.11. The TVC capability of the NANO AR3 was recently verified at the Forschungs- und Technologietransfer GmbH (FOTEC) diagnostics facility [87]. A remotely-controlled semi-circular rotating arm equipped with 23 Faraday cups measured the spatial ion current density distribution, while an autonomous algorithm translated the commanded thrust vector into the extractor electrode voltages.

Figure 2.11: ENPULSION NANO AR3 thruster unit (LHS) and differential throttling demonstration (RHS). The central profile in the RHS corresponds to a minimum thrust vector angle. Sourced from [81], [87].

The measured deviations for the inclination and azimuthal angle were typically below 2 degrees and below 10 degrees, respectively.

2.3.2 Clustering

TVC can also be achieved with stepped thrust differentials, i.e., clustering (see Fig. 2.3). For example, the SiEPS offers TVC through clustering: eight thruster units, each with its own voltage control system, are distributed across the propulsion panel to provide dual-axis attitude control and single-axis propulsion with a Δv on the order of 10^2 m s^{-1} [46]. Experimental work with four iEPS thrusters placed in roll configuration for attitude actuation was also carried out by Mier-Hicks et al. [26]. Pairs of modules emitting ion beams of opposite polarity were placed on opposing sides of a magnetically-levitated mockup nanosatellite to produce complementary torques. The modules demonstrated set point accuracies of 15 arcseconds over the course of 20 min and 22 arcseconds over the course of 10 hr. The configuration also demonstrated slew rates of 0.3 to 1.8 degrees min^{-1} when operating at 2.4 μN of thrust per module.

2.3.3 Pulsed Control

Courtney et al. [69] investigated pulsed operation of the Busek BET-300-P electrospray thruster. Pulse-width modulation (PWM) was used to regulate the average thrust from 12 μN to 96 μN when pulsing at 2 Hz and 5 Hz. As shown in Fig. 2.12, an increase in the duty cycle corresponded to an increase in the average thrust, as more total current was being emitted over one cycle. The BET-300-P was also used to demonstrate pulse widths on the order of ms, suggesting pulse frequencies on the order of 100s of Hz are possible [94]. These pulses corresponded to measured impulse bits on the order of 100 nN s. However, transient effects such as inrush current spikes and ms-long rise times were also observed when transitioning from inactive to high current levels (100 μA), suggesting that there is likely an upper limit to the pulse frequency beyond which emission is highly unstable. Current efforts are underway at Busek to develop the BET Multi-Axis

(BET-MAX) propulsion system, which will use four BET-300-P thrusters distributed across the nanosatellite propulsion plane to achieve multi-axis attitude actuation [96].

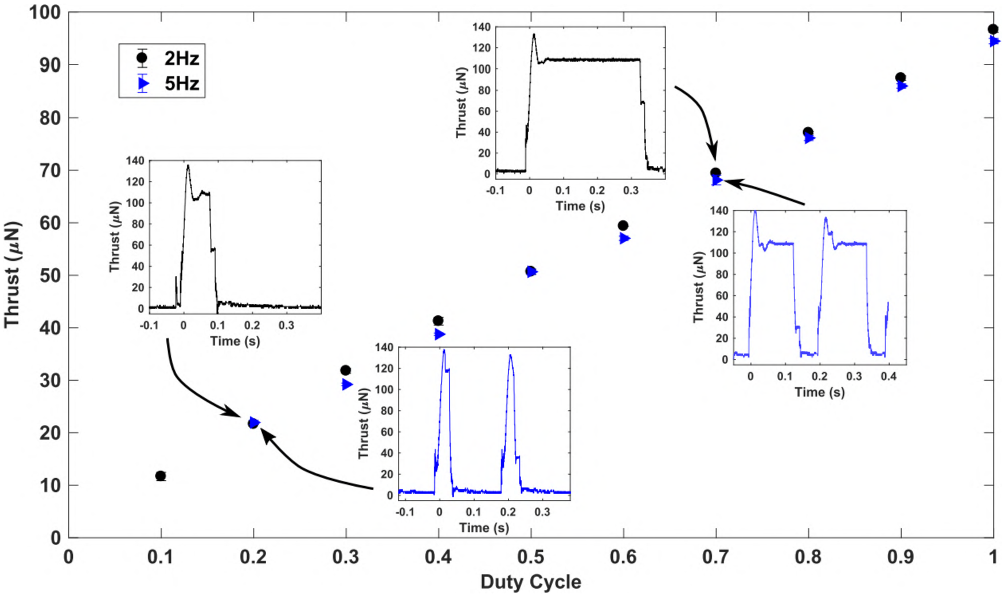

Figure 2.12: Busek BET-300-P average thrust control via PWM (sourced from [69]).

2.4 ESP Modeling

Modeling of electrospray thrusters is useful for studying electrospray physics, characterizing life-limiting mechanisms in thrusters, estimating thruster performance, and informing the thruster design [72]. ESP models may be categorized into numerical fluid and particle models as well as parametric numerical and analytical models. Fluid models are useful for studying propellant flow, cone-jet formation, and droplet emission and evolution. Particle models treat droplets, clusters, and ions as discrete point particles and are used to study their trajectories and interactions in the emission plume. Parametric numerical and analytical models are used for rapid parametric studies that inform the thruster design, for investigating electrospray physics, and for estimating thruster performance.

Since the electrospray process is complex and the performance of electrospray thrusters is dependent on a wide range of parameters, ESP models typically investigate specific/limited regions of the thruster. For example, the Plasma and Space Propulsion Laboratory (PSPL) at the University of California, Los Angeles (UCLA) [72] identified four overlapping regions for modeling (Fig. 2.13). The first is the extraction region, which addresses fluid flow in the upstream emitter and reservoir domains and where the ES force overcomes the surface tension force such that charged particles in the form of droplets or ions are emitted. This region is typically modelled using electrohydrodynamic (EHD) analysis. Next is the transition region, where a transition from cone-jet to droplet emission as well as field evaporation are observed. The next region is referred to as the interaction region and it is where Coulombic interactions of charged particle as well as droplet and cluster fragmentation is observed. Finally, charged particle dynamics in the plume region are governed primarily by the macroscopic electromagnetic field.

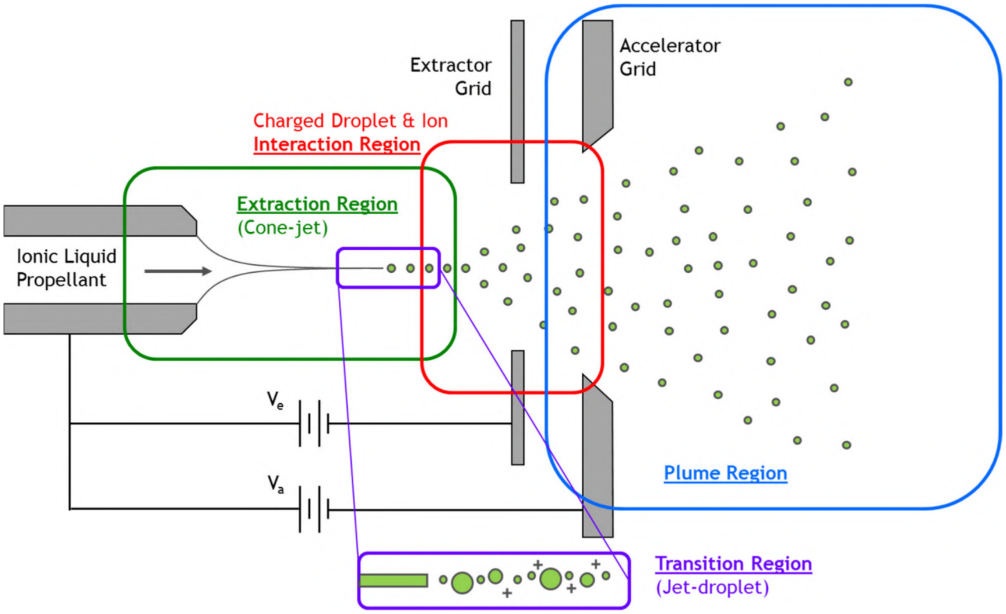

Figure 2.13: PSPL electrospray thruster simulation regions (sourced from [72]).

2.4.1 EHD Modeling

An accurate representation of the local pressure and electric field variations which give rise to multiplexed emission can be achieved with EHD modelling. The governing EHD equations [53], [97], coupled with the volume-of-fluid (VOF) method for a propellant and vacuum interface, are summarized below. The Poisson equation

$$\nabla^2 V = -\frac{\rho_\mathrm{e}}{\epsilon}, \tag{2.20}$$

in which V is the electric potential, ρ_e is the charge density, and ϵ is the electrical permittivity, is used as the source term in the charge transport equation:

$$\frac{\partial \rho_\mathrm{e}}{\partial t} + \nabla \cdot \mathbf{J} = 0, \tag{2.21}$$

where $\mathbf{J} = \sigma_\mathrm{e}\mathbf{E} + \rho_\mathrm{e}\mathbf{u}$ is the current density for a given electric field $\mathbf{E}$ and fluid velocity $\mathbf{u}$. Gauss's law

$$\mathbf{E} = -\nabla V, \tag{2.22}$$

is used to compute the electric field, and the charge conservation equation is solved alongside the incompressible Navier-Stokes equation:

$$\rho \left[\frac{\partial \mathbf{u}}{\partial t} + \mathbf{u} \cdot \nabla \mathbf{u} \right] = -\nabla P + \mu \nabla^2 \mathbf{u} + \rho \mathbf{g} + \mathbf{F}_\mathrm{e} + \mathbf{F}_\mathrm{ST}, \tag{2.23}$$

where P is the pressure, $\mathbf{F}_\mathrm{e}$ is the electric force, and $\mathbf{F}_\mathrm{ST} = \gamma\kappa\mathbf{n}$ is the surface tension force subject to an interface curvature κ. The electric force is computed via:

$$\mathbf{F}_\mathrm{e} = \rho_\mathrm{e}\mathbf{E} - \frac{1}{2}\mathbf{E}^2 \nabla \epsilon. \tag{2.24}$$

Notable EHD models of the extraction region include those developed by PSPL [72], Forbes [97], and Mallalieu [53]. PSPL [72] used OpenFOAM to solve the above EHD equations, employing the model to simulate cone-jet emission of heptane from a capillary. Forbes [97] developed an EHD model of the Array of Micromachined UltraSonic Electrospray (AMUSE) ion source, a mechanically-driven and droplet-based capillary emitter array used for MS, in ANSYS Fluent. This Fluent framework was later elaborated upon by Mallalieu [53], who incorporated the Fluent built-in porous media solver into the AMUSE EHD model to describe fluid flow through and droplet emission from a porous wedge. The VOF for EMI-BF4 propellant from [53] for the first 0.1 ms of operation is shown in Fig. 2.14. Other notable electrospray EHD models include the Yan et al. [98] study of core-shell droplet formation in coaxial EHD atomization (CEHDA) of poly(lactic acid) (PLA) and poly(lactic-co-glycolic acid) (PLGA) solutions.

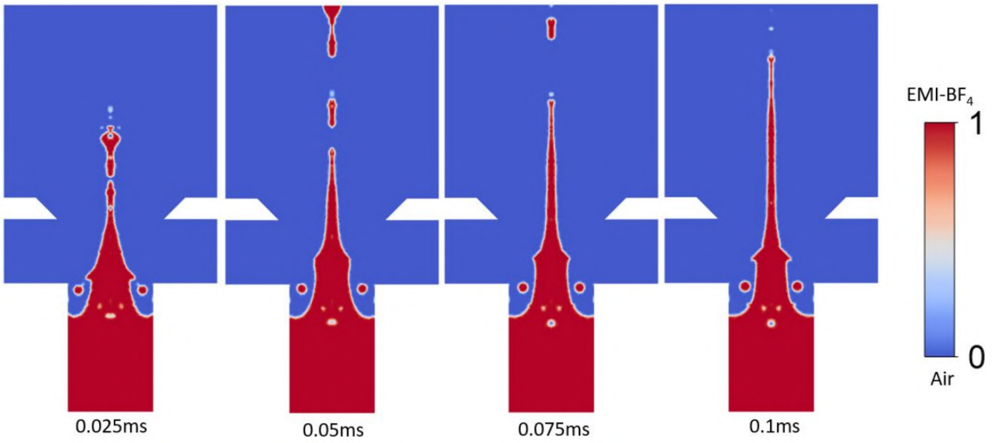

Figure 2.14: EMI-BF4 VOF for first 0.1 ms of droplet emission from a porous cone (sourced from [53]).

2.4.2 Particle Modeling

Particle modeling is useful for simulating charged particle trajectories and interactions in the interaction region as well as the near-field and far-field plume regions. Particle trajectories are typically described via the Lorentz force:

$$\mathbf{F} = q\left(\mathbf{E} + \mathbf{v} \times \mathbf{B}\right), \tag{2.25}$$

in which **B** is the magnetic field and the electric field is determined via Eq. 2.22. PSPL [72] used COMSOL Multiphysics to study Coulombic interactions between droplets. The droplets were treated as point charges with spherical drag and the simulation demonstrated how dissimilar axial droplet velocities causes clustering, which leads to lateral perturbance of the droplets. High-speed video microscopy was also used to experimentally capture the electrospray plume expansion caused by the Coulombic interactions of charged ethanol droplets in the downstream cone-jet and near-field plume region. The same particle model was also used to simulate the evolution of mass-varying particle populations and showed that smaller droplets experience greater lateral displacement relative to larger droplets.

The particle-in-cell (PIC) technique is commonly employed to simulate electrospray thrusters [70]. PIC simulations utilize the Lagrangian representation of macroparticles to describe their behaviour within a discretized simulation mesh [99]. The charge density and current density at each mesh node are solved via weighted scattering, and the electromagnetic fields are then solved via the finite difference method. The electromagnetic fields at each node are gathered onto each macroparticle to push it according to the

Lorentz force (Eq. 2.25). Petro et al. [70] used the PIC method to investigate the fragmentation, trajectory, and space-charge effects of EMI-BF4 species. Characterization of ionic cluster fragmentation is critical for determining the thruster polydispersive efficiency (Eq. 2.9).

2.4.3 Parametric Modeling

Parametric modeling is useful for identifying optimized design values. For example, Jones [100] used a numerical scheme to investigate the effects of geometry and materials on the onset voltage of arrayed capillary emitters. The capillary radius, height, emitter pitch, and relative permittivity of the surrounding medium were varied in combinations to determine which values would require the lowest onset voltage. It was found that dielectric mediums with relative permittivity near unity, capillary heights greater than 300 μm, smaller capillary radii, decreased spacing between the emitter and extractor electrode, and a pitch-to-height ratio greater than 2.5 was ideal in reducing the onset voltage. Analytical modeling also serves as a useful tool for rapid parametric analysis of the thruster design and for estimating the thruster performance. Parametric numerical and analytical ESP modeling will be discussed further in Chapter 4.

2.5 HV Electronics

To achieve the necessary electric field strength for electrospray emission, electrospray thrusters typically operate in the kV regime [101]. Periodic polarity reversal to maintain spacecraft charge balancing and mitigate space-charge inefficiencies is also employed [40], [58]. Finally, galvanic isolation of the HV rails from the LV electronics is critical for ensuring none of the sensitive low voltage (LV) electronics become damaged. Meeting these requirements, all while operating within the constraints of nanosatellite SWaP targets, is the purpose of an ESP power processing unit (PPU). The thruster PPU also typically acquires voltage and current measurements at each emitter using VDs and SRs, respectively, incorporates over-voltage and over-current protection, conditions the HV rails, and interfaces with the data and command interface unit (DCIU). The DCIU transmits telecommands (TC) to and monitors telemetry (TM) from the PPU, interfaces with the parent system (typically the OBC), and processes and stores incoming PPU TM. The DCIU may also incorporate features such as feedback control systems to operate at a constant voltage or current.

2.5.1 HV Circuitry Generation

The PPU HV circuitry may be built from a series of low-level electronics components, as with the bimodal MP-ESP (MEPS) PPU developed at the University of Illinois Urbana-Champaign (UIUC) in collaboration with Froberg Aerospace [102]. The MEPS PPU is composed of two separate voltage-boosting circuits, one delivering ±3250 V during ESP operation and the other delivering 24 V during chemical operation. The ESP circuit (Fig. 2.15) consists of a two-phase interleaved boost converter (TPIBC) operating at 100 kHz, followed by a high-frequency 1:7 step-up transformer, and completed by a Cockcroft-Walton voltage multiplier (CWVM). The output voltage of the boost converter V_{BC} is controllable via:

$$V_{\mathrm{BC}} = \frac{V_{\mathrm{bus}}}{1 - D_{\mathrm{PWM}}}, \tag{2.26}$$

in which V_{bus} is the bus voltage and D_{PWM} is the duty cycle. This control allows for closed-loop management of the output voltage. The transistors alternate pulse production, and each pulse enters opposite ends of the transformer primary, ultimately generating an alternating current signal. Isolation between the HV components and LV circuitry is provided by the transformer. The transformer also provides an intermediate voltage increase, thereby reducing the burden on the TPIBC. The CWVM rectifies the transformer signal through six capacitor-diode stages, each of which consists of two capacitor-diode pairs. The CWVM output voltage V_{VM} is determined by the number of stages N:

$$V_{\mathrm{VM}} = 2NV_{\mathrm{in}}, \tag{2.27}$$

where V_{in} is the input voltage. With a bus voltage of 7.4 V, an overall gain of 440 is needed for ESP mode. Using Eq. 2.26, a TPIBC output of 39 V is achieved with an 81 percent duty cycle. The voltage is then multiplied by the transformer turn ratio and then further multiplied via Eq. 2.27. The TPIBC and CWVM prototype boards are shown in Fig. 2.16. The predicted ESP current is 350 μA, resulting in an estimated 1.14 W input power draw [102].

The PPU HV circuitry may also be built using commercial-off-the-shelf (COTS) HV converters and components. For example, both the iEPS PPU developed by Mier-Hicks et al. [101] and the California Polytechnic State University (Cal Poly) PPU developed by Howe [59] used the ultra-miniature XP Power A series DC-HVDC converters to generate the required HV rails. The iEPS PPU [101] used A30s (±3000 V) as well as HV relays in an H-bridge configuration to power four emitters, with four relays switching the polarity of the HV supply and four relays used for thruster pair activation. Howe [59] used a single A20 converter (+2000 V) and developed an extensive integrated diagnostics suite for the operation of one emitter at a single polarity, with features such as active current limiting circuitry as well as a heater and complementary thermocouple circuit.

Alternatively, many ESP laboratories use a combination of commercial HV power modules, such as signal generators coupled with HV DC power supplies, to generate the HV rails necessary for electrospray. For

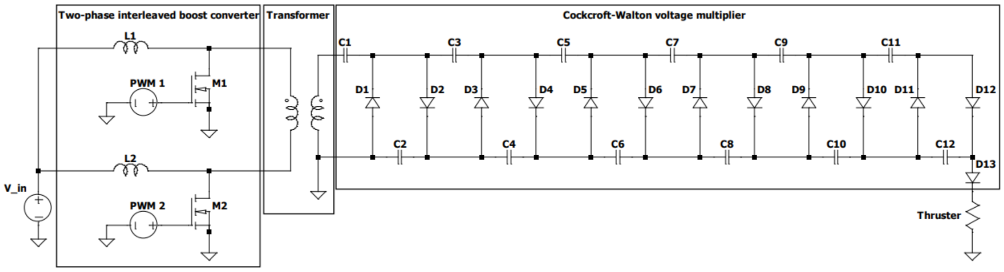

Figure 2.15: MEPS ESP PPU schematic (sourced from [102]).

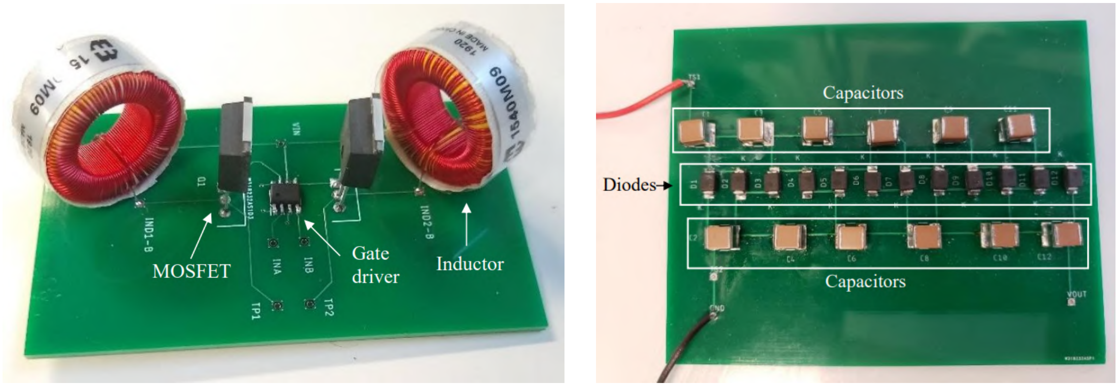

Figure 2.16: MEPS ESP PPU TPIBC (LHS) and CWVM (RHS) prototypes (sourced from [102]).

example, Huang et al. [90] used a Rigol DG1022Z signal generator connected to a HV power supply to achieve bipolar emission, Chen at al. [50] used the dual-channel HB-S502-10AC to deliver ±10,000 V, and Natisin et al. [79] used a high speed pulse generator with an output of ±3500 V, a rise time of 25 ns, and a switching frequency of up to 30 kHz for testing of the AFET-2.

2.6 Multimodal ESP Systems

Multimode propulsion (MMP) is the integration of multiple propulsive modes into a unified system in which the key attribute is shared propellant between modes [11]. MMP has the potential to provide advanced, versatile propulsion capabilities to future nanosatellite missions. MMP is in contrast to hybrid-mode propulsion, in which multiple, but separate, propulsion systems are available onboard a spacecraft. The main disadvantage of hybrid mode propulsion is that it requires the preallocation of propellant to specific modes for particular mission phases. MMP offers increased mission flexibility by allowing for in situ propellant allocation and reduces the overall spacecraft dry mass through the unification of the respective propellant management and electrical systems. It is especially relevant for nanosatellites, which have stringent SWaP constraints. While the constituents of a MMP system may have performance envelopes similar to all-chemical or all-electric systems, their unification provides higher payload transfer rates through higher payload mass fractions and lower burn times.

One promising multimodal system currently being developed by multiple organizations [102]–[105] is the bimodal MP-ESP system, which operates in high thrust, low specific impulse monopropellant mode and relatively low-thrust, high specific impulse electrospray mode. Another promising multimodal system is the cold gas and ESP bimodal thruster. Little and Jugroot [48] investigated the use of a 5-mm-long linear gold gas nozzle situated above a 3.5-mm-long P5-grade porous wedge emitter. A thin molybdenum film was inserted at the throat of the cold gas nozzle to extract and accelerate the electrospray plume. A torsional thrust balance measured the thrust and specific impulse of the cold gas mode, operating using nitrogen, to be 7.9 mN and 43.3 s, respectively. The emitted current in electrospray mode was measured to be only 250 nA, where imagery of the emitter apex displayed evidence of pore closure, which likely reduced the number of active emissions sites.

2.7 Concluding Remarks

A detailed overview of ESP was provided in this chapter. The physics of electrospray emission, ESP propellants, performance metrics of ESP devices, and diagnostic techniques were discussed. Porous ESP and ESP TVC were introduced, and the development of ESP modeling methods, ESP PPUs, and multimodal ESP systems were reviewed. In concluding this review of ESP, it can be asserted that ESP devices have the potential to provide superior propulsion capabilities to nanosatellites, as they operate at high performance levels and are typically housed in exceedingly small form factors, making them ideal to meet the SWaP constraints of nanosatellites. However, there are still a number of life-limiting mechanisms and performance challenges, namely propellant overspray and polydispersive inefficiencies, that will need to be addressed before ESP devices become robust, economical, and even ubiquitous. The following chapter will detail the mechanical, electrical, and experimental design of the electrospray thruster developed for this research.

3 VET Design

As discussed in Chapter 2, propulsion systems with TVC capabilities can enable significantly greater return from next-generation nanosatellite missions. The Vectored Electrospray Thruster (VET) was thus developed at the Royal Military College of Canada Advanced Propulsion and Plasma Exploration Laboratory (RAPPEL) to provide improved propulsion capabilities to nanosatellites [7]. The VET uses the principles of clustering, based on the SiEPS [46], and pulsed control, based on the BET-300-P [69], to achieve high-resolution TVC. The design and fabrication of a two-emitter prototype offering single-axis attitude actuation is presented.

3.1 Principle of Operation

For an electrospray thruster with multiple distributed emitters (i.e., one which employs clustering), varying the duty cycle of each emitter varies the total current it emits and therefore the total thrust it produces. The resulting thrust differentials across the nanosatellite propulsion plane enable TVC (see Fig. 2.3). Figure 3.1 illustrates the nine-step PWM configuration for the two-emitter VET prototype operating along one rotation axis—either the spacecraft yaw or pitch axis. Nine steps were selected to allow each emitter (E0 and E1) to operate in duty cycle increments of 25 percent. At steps 0 and 8, a single emitter operates exclusively, resulting in maximum torque on the nanosatellite. As the duty cycle for the opposing emitter is increased, the torque is balanced out and the spacecraft experiences a more linear acceleration—though the overall trajectory still possesses curvature. At the central step, step 4, both emitters operate at a maximum duty cycle and the spacecraft experiences strictly linear acceleration.

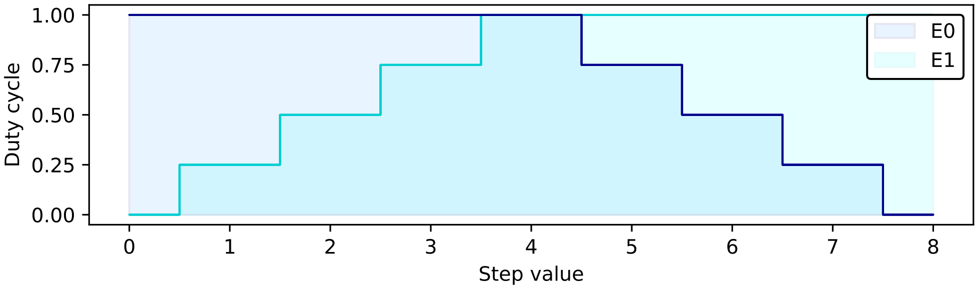

Figure 3.1: Nine-step VET PWM configuration used to produce emission differentials across two porous wedges. E0 refers to Emitter 0 and E1 refers to Emitter 1.

3.2 Mechanical Design

An exploded view of a rendered VET module is illustrated in Fig. 3.2, while a fully-assembled VET module and magnified cross-section of the emitter apex is shown in Fig. 3.3. The housing base was fabricated from polyether ether ketone (PEEK), had dimensions of 96 mm × 24 mm × 12 mm (sized to within CubeSat standards), and housed the steel distal electrode [106] and ROBU sintered borosilicate glass emitters. PEEK was selected as the housing material as it is easy to manufacture, is not electrically conductive, and has low offgassing rates [107]. For each side, a 10-mm outer diameter (OD) carbon steel wave disc spring and PEEK housing lid provided compression forces to secure the components, while a thin sheet of wetted Whatman Grade 1 qualitative filter paper provided an electrical interface between the distal electrode and emitters. Each HV rail was fastened to the distal electrodes via ring connectors. Notably, this design did not feature a porous reservoir, as is commonly seen in literature [79], [83]. The purpose of this design choice was to test whether a single porous emitter could act as both an emission source and reservoir, which would allow for further miniaturization and simplification of the thruster design.

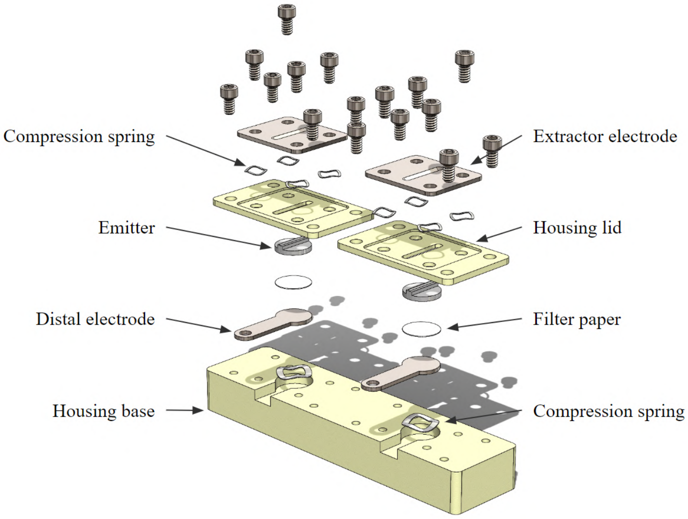

Figure 3.2: VET module exploded view.

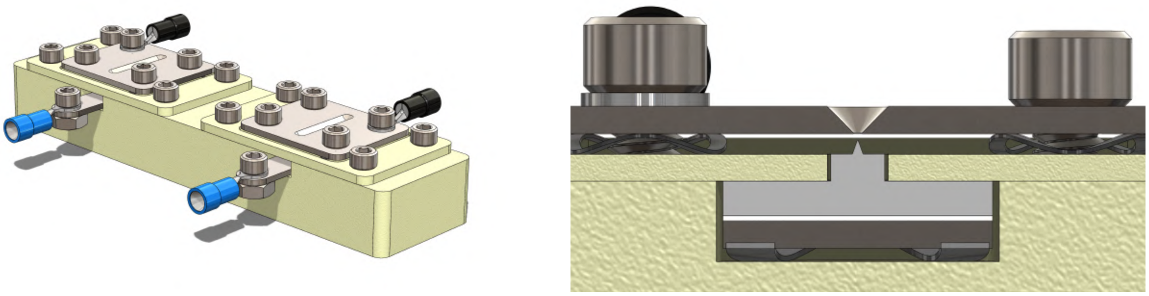

Figure 3.3: Complete VET module assembly (LHS) and magnified cross-section of the emitter apex (RHS).

The porous emitter featured a 1-mm-tall rectangular platform which fixed its rotation with respect to the housing lid and provided coarse alignment of the emitter apex with the extractor electrode aperture [79]. The housing lid was fabricated from a 1.6-mm-thick PEEK sheet, therefore a 24 mm × 20 mm × 0.6 mm inset cut was added to the housing lid such that the lid and the emitter rectangular platform would be flush and to accommodate the extractor electrode. The emitter wedge was designed to have a height of 500 μm, an apex radius of curvature of 20 μm, and a wedge full angle of 40 degrees. The extractor electrodes were compressed against a set of smaller wave disc springs, allowing for the height and pitch of each extractor to be finely adjusted, as shown in the RHS of Fig. 3.3. Each extractor electrode was fabricated from a single sheet of 1-mm-thick aluminum and featured a 45-degree chamfer which diverged from a 250-μm-wide aperture. Electrospray beam divergence from a porous wedge can reach half-angles of 35 degrees [75], therefore the chamfer was added to reduce interception of the beam current by the extractor. Insulating PEEK screws were originally used to secure the extractor electrode to prevent electrical shorts that may occur due to propellant leakage within the housing interface when the housing lid is compressed against the emitter; however, it was found that the PEEK screw heads would easily strip after repeated use and thus regular steel screws were used for securing the extractor electrode. Similar to the distal electrodes, a ring terminal was secured to each of the extractor electrodes to provide a ground connection. All fasteners used in the VET module were selected as #4-40 threads. In an attempt to identify any major design flaws, the initial configuration was 3D-printed to scale (Fig. 3.4, LHS) and assembled. This 3D printed prototype served as a valuable tool for validating the thruster concept and iterating the design. The RHS of Fig. 3.4 shows the finished VET module mounted to the thruster mount plate. Table 3.1 provides a summary of the mechanical design.

While previous electrospray emitters developed at RAPPEL were microfabricated using picosecond laser ablation [48], the emitters in this work were fabricated using conventional machining techniques on a Haas VF-5/40 CNC mill according to the procedure outlined by Natisin et al. [79]. Figure 3.5 shows scanning electron microscope (SEM) images of sample P4-grade and P5-grade emitters fabricated with both ball nose end mills and tapered square end mills. The upper LHS image illustrates the platform and wedge geometry of the first iteration of emitters, while the upper RHS image shows its apex from the side. The apex radius of curvature of the first iteration is estimated to be below 50 μm. As shown in the upper RHS image, the apex has undergone minor fracturing during manufacturing and thus irregularities in the apex height and curvature are present. The middle and lower image sets show the second iteration of P4-grade and P5-grade emitters, respectively. While the tapered square end mill provided a sharper triangular profile, it can be seen in the middle and lower RHS images that the apexes have trapezoidal profiles with widths on the order of 50 to 100 μm. This profile would likely cause the electric field to be strongest on the corners of the trapezoid, as opposed to along the central axis, and thus lead to significant off-axis emission directed towards the extractor electrode. Nonetheless, these first attempts at conventional CNC fabrication of porous glass emitters by RAPPEL have yielded extremely promising results, and there are current efforts underway to fabricate sharper and more uniform wedges.

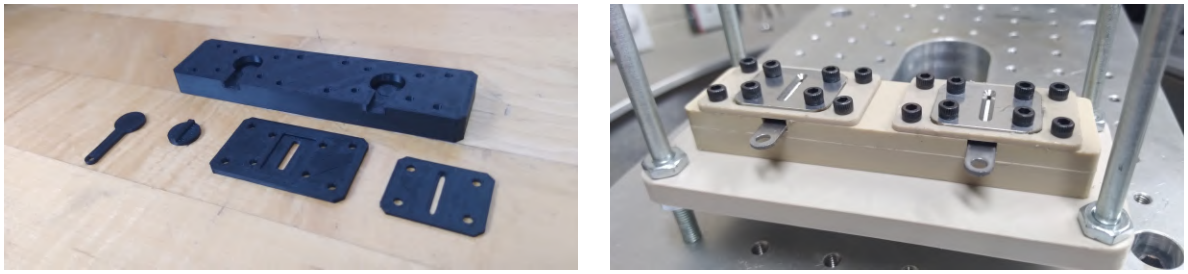

Figure 3.4: VET module 3D printed prototype (LHS) and fully-fabricated assembly (RHS).

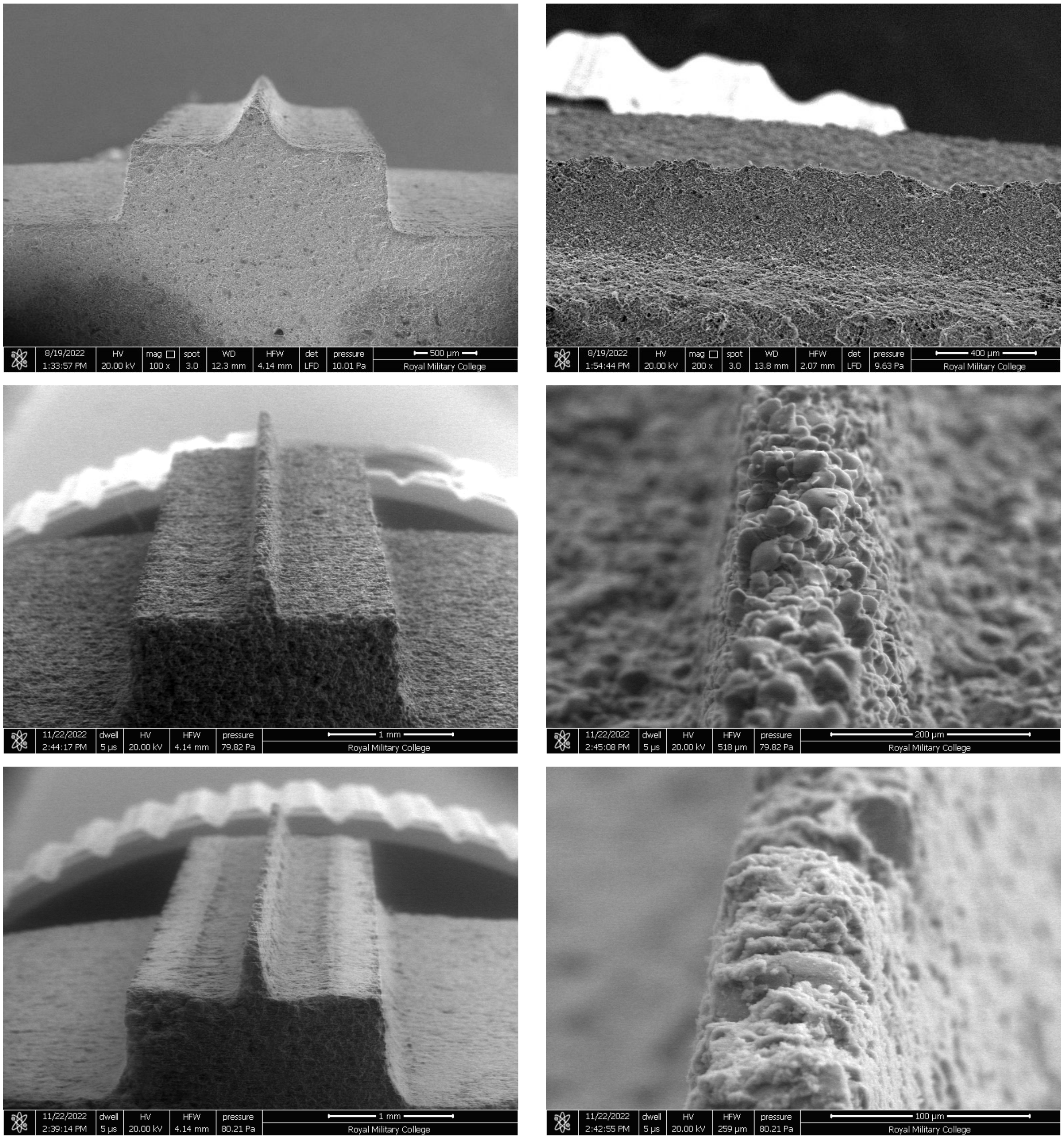

Figure 3.5: SEM images of conventionally-machined P4-grade and P5-grade emitters. Upper LHS: front profile of a P5-grade emitter platform and wedge, milled with a ball nose end mill. Upper RHS: side profile of the same P5-grade emitter apex, illustrating irregularities along the apex. Central LHS: front profile of a P4-grade emitter, milled with a tapered square end mill. Central RHS: magnified view of the same P4-grade emitter apex. Lower LHS: front profile of a second P5-grade emitter, milled with a tapered square end mill. Lower RHS: magnified view of the same P5-grade emitter apex.

Table 3.1: Summary of VET mechanical components.

Component	Material	Dimensions	Features
Housing base	PEEK	96 mm × 24 mm × 12 mm	• Two symmetric emitter insets • Bottom #4-40 holes for securing to thrust mount
Lower spring	Carbon steel	10 mm OD × 200 μm	• Lower compression force
Distal electrode	Stainless steel	10 mm OD × 1 mm	• 18 mm × 6 mm tab • #4 through hole for ring connector
Interface	Cellulose paper	10 mm OD × 180 μm	• 11 μm pore sizes
Emitter	Borosilicate glass	10 mm OD × 2.8 mm	• Height: 500 μm • Apex radius: 20 μm • Half-angle: 20 degrees • P4-grade: 16 μm pore sizes • P5-grade: 1.6 μm pore sizes
Housing lid	PEEK	40 mm × 24 mm × 1.6 mm	• 25 mm × 21 mm × 0.6 mm inset cut • Upper compression force
Upper springs	Stainless steel	6 mm OD × 150 μm	• Used for pitch and alignment control of extractor electrode
Extractor electrode	Aluminum	24 mm × 20 mm × 1 mm	• 12 mm × 250 μm aperture • 45 degree chamfer
Fasteners	Black-oxide steel	#4-40	• All fasteners standardized to #4-40

3.3 Electrical Design

A custom PPU was developed to generate the HV rails necessary for electrospray emission and to monitor the thruster during operation [59], [108], while a custom DCIU was developed to receive TM from and transmit TC to the PPU and provide a graphical interface unit (GUI) to the user.

The ultra-miniature XP Power A Series A30 DC-HVDC converters were selected to deliver ±3000 V at 330 μA total output current to the emitters, while optocouplers were used to toggle the HV rails. A commercial microcontroller board was used to issue HV settings to the A30 converters as well as to issue PWM commands to the optocouplers. A digital-to-analog converter (DAC) was used to convert digital commands from the microcontroller into proportional control voltages for the A30 converters, while an operational amplifier (op-amp) acted as a voltage follower and provided the current gain required to power the HV converters. A high-side VD and high-side SR were placed directly prior to each emitter to measure the operating voltage and emitter current draw, respectively. This housekeeping data was directed to isolation amplifiers (iso-amps) that were powered by isolation-based voltage regulators and output their signals to the built-in analog-to-digital converter (ADC) in the microcontroller. The A Series converters, optocouplers, voltage regulators, and isolation amplifiers provided complete galvanic isolation between the HV and LV rails, ensuring all the sensitive electronic components were safe during operation.

Figure 3.6 illustrates a breadboard prototype of the PPU developed early in this research. The prototype circuit drew approximately 5 W during HV operation, which is acceptable for a solar-power-based nanosatellite EPS [8]. The breadboard prototype validated the PPU design and a printed circuit board (PCB) prototype was then developed. The PCB prototype consisted of two PCBs, one that contained the HV and PWM control (CTRL) electronics and one that contained the data acquisition (DAQ) electronics.

Figure, 3.7 is a simplified schematic of the PPU, while Fig. 3.8 shows the final prototype version of the PPU used for testing. The configuration consists of the two aforementioned PCBs, the commercial microcontroller board, and two additional breadboards. The central breadboard contained a resistor-capacitor (RC) clamping circuit, which was added to prevent voltage overshoot during HV switching. The lower-right breadboard contained summing amplifier (sum-amp) circuits: since the microcontroller ADC only accepted an input of 0 to 5 V and the FEMTO current amplifiers—used in the diagnostics suite to measure the emitted current at a collector plate—output ±1 V, the intermediate sum-amp circuit was included in the design to add a DC offset to the FEMTO signals (FEMTO-0 and FEMTO-1). The microcontroller and a personal computer exchanged TM and TC via wired serial communications. The PCBs were each sized to 96 mm × 96 mm with the intention of meeting the CubeSat size standard. All integrated circuits (ICs) and passive components used in the PCBs were the same through-hole-technology (THT) elements used in the breadboard prototype, which allowed for the direct application of known and verified elements to be used and easier

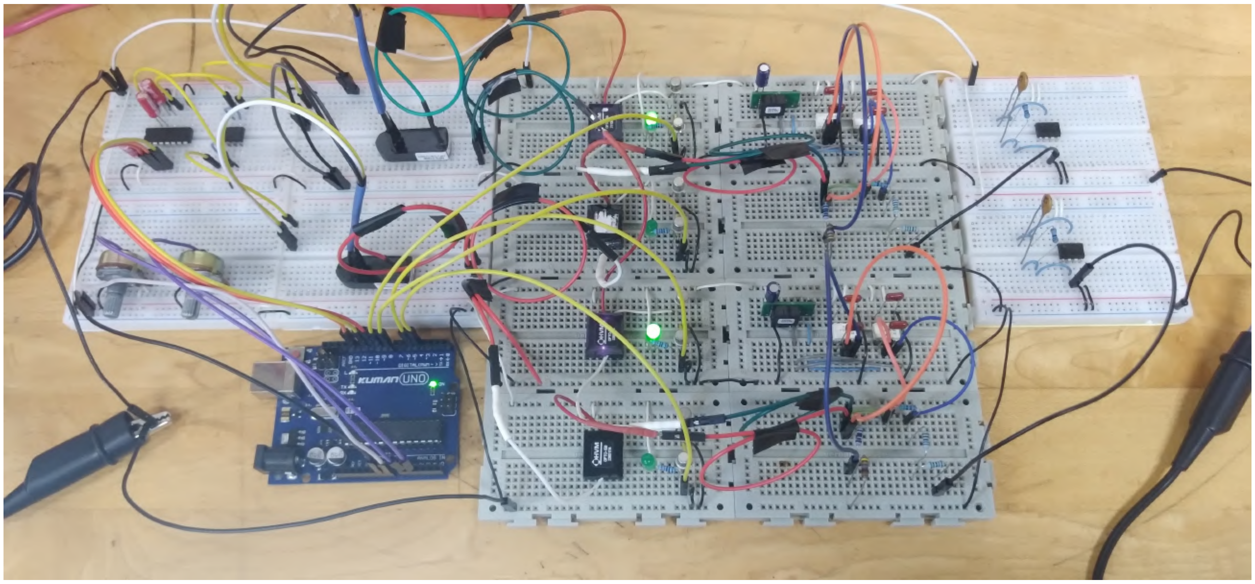

Figure 3.6: VET PPU breadboard prototype. The left breadboard contained the DAC, voltage follower, and XP Power A30 converters. The middle breadboard contained the switching transistors, optocouplers, voltage regulators, voltage dividers, shunt resistors, and isolation amplifiers. The final board contained a set of unipolar transimpedance amplifiers that measured the output current [109]; these were replaced with FEMTO DHPCA-100 current amplifiers during testing.

soldering/desoldering operations to be performed. In addition, all ICs and shunt and voltage divider resistors were connected to the PCBs via sockets, which allowed for these elements to easily be swapped in the case a different component was required or an element became defective. Finally, coaxial cables were used to deliver the HV rails to the vacuum chamber. Further details on the PPU and DCIU can be found in Appendix A.

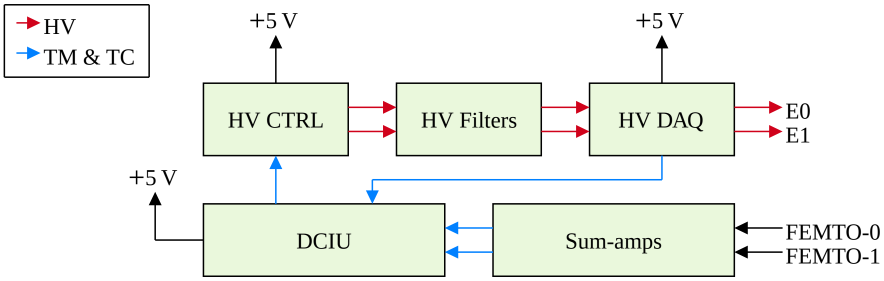

Figure 3.7: Simplified schematic of the VET PPU.

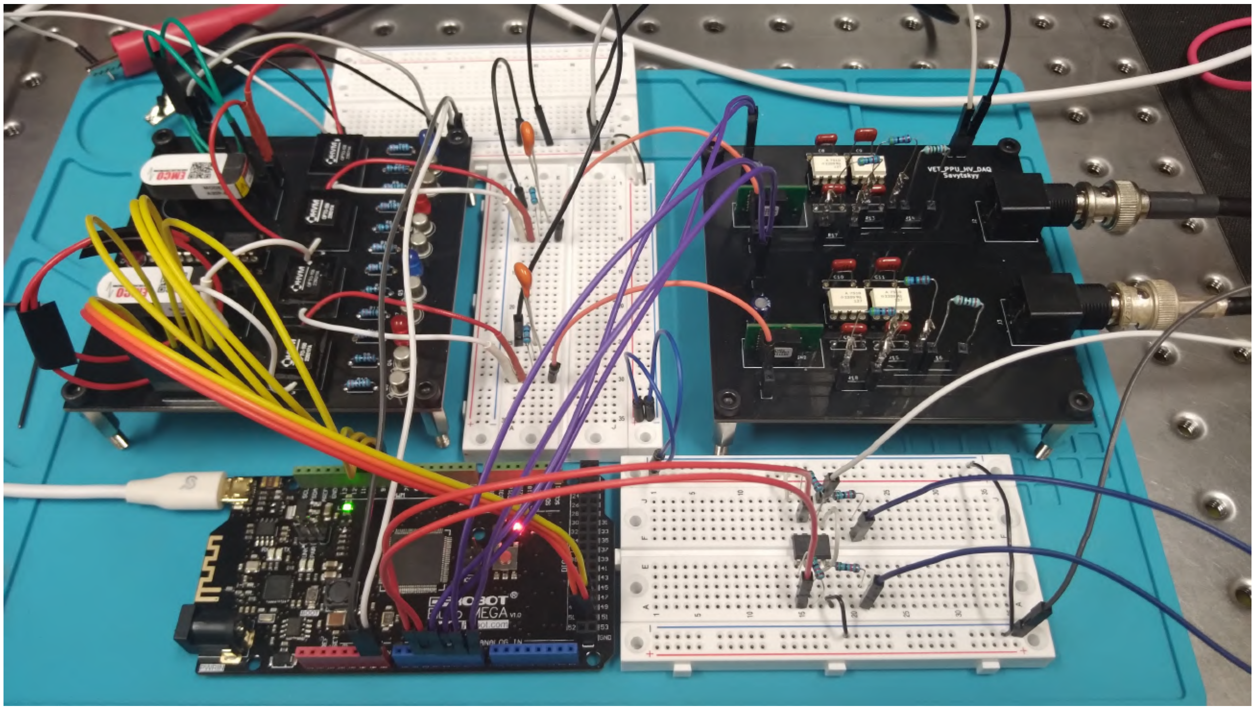

Figure 3.8: Final iteration of the VET PPU used for testing. The left-most PCB contained the HV and PWM control electronics, while the right-most PCB contained the DAQ electronics. The central breadboard contained an RC clamping circuit, while the lower-right breadboard contained the summing amplifier circuit. The commercial microcontroller board is in the lower-left.

3.4 Diagnostics Suite

A simplified schematic of the diagnostics suite used to validate the VET TVC capabilities is illustrated in Fig. 3.9. Two FEMTO DHPCA-100 variable gain high-speed current amplifiers measured the current collected at each collector plate and output their signals to the PPU and an oscilloscope for waveform analysis [109]. Note that a 50 Ω load was added to the FEMTO output lines for impedance matching. A negatively-biased electron suppression grid (ESG) prevented secondary electrons emitted by the collector plates from impinging on the VET module [79], [109].

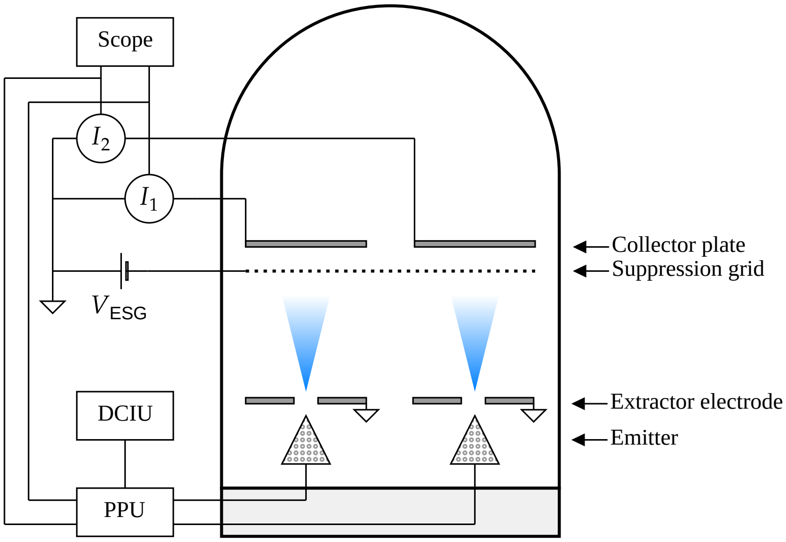

Figure 3.9: VET experimental platform schematic.

3.5 Concluding Remarks

The operational, mechanical, electrical, and experimental designs of the VET concept were detailed in this chapter. The dual-emitter VET prototype uses the principles of clustering and PWM to provide TVC for nanosatellites. The thruster housing, electrodes, and porous emitters were all fabricated in house. The porous emitters were the first iteration of conventional CNC-milled emitters fabricated at RMC, therefore the emitter apexes are highly trapezoidal and nonuniform. It is expected that future iterations of CNC-milled emitters will yield sharper and more uniform results. A custom PPU was also developed to provide bipolar HV rails to each of the porous emitters. The PPU featured a PCB suite for HV control as well as voltage and current DAQ, and additional breadboard elements were included after for conditioning the HV rails and processing measurements collected by the diagnostics suite. The following chapter will discuss efforts to model the VET emission profile and estimate the thruster performance.

4 VET Emission Profile Modeling

Analytical and numerical modeling are commonly employed to inform the thruster design and to estimate thruster performance. Initial design of the VET was influenced by preliminary PIC modeling of ion trajectories. An analytical model based on the Wright and Wirz framework [82] was also used to estimate the VET beam composition and torque profile. The analytical model provided a reference for whether a single P5-grade emitter can act as both the emission source and reservoir, which would allow for further miniaturization of the thruster design.

4.1 Electrostatic Deflection

An ES PIC (ES-PIC) simulation was initially performed to investigate ES-deflection-based TVC from a capillary using EMI-BF4 in ion mode, similar to what is employed by the ENPULSION NANO AR3 [87]. The purpose of the simulation was to determine how a deflected ion beam would evolve and whether electrostatic deflection of a single linear emitter could offer single-axis TVC. ES-PIC simulations utilize the Lagrangian representation of macroparticles to describe their behaviour within a discretized simulation mesh [99]. The charge density at each mesh node is solved via weighted scattering, and the electric potential is then solved via Poisson's equation (Eq. 2.20) using the finite difference method. Gauss's law (Eq. 2.22) is then used to solve the electric field, which is subsequently gathered onto each macroparticle to push it according to $\mathbf{F} = q\mathbf{E}$. The ES-PIC simulation used Python code developed and validated by the author prior to the start of this graduate programme.

The evolution of EMI-BF4 over 17 ns is shown in Fig. 4.1, in which the dashed line is the central thrust axis. The capillary width was set to 80 μm, the electrode gap width was set to 200 μm, and the electrode distance from the capillary was set to 180 μm. The left electrode was biased to -1800 V and the right electrode was biased to -2200 V (Eq. 2.6). EMI-BF4 ions were injected at the approximate location of a Taylor cone apex with velocities calculated from the average potential of $-2000\,\text{V}$. Thrust vectoring via electrostatic deflection is clearly illustrated in Fig. 4.1, where the asymmetric electric field causes deflection of the ion beam towards the right electrode. While this configuration may provide TVC, it would likely also exacerbate propellant overspray to the electrodes, which would accelerate thruster degradation, as discussed in Chapter 2. Notably, the beam spread is underrepresented in this simulation as electrospray plumes may expand to half angles of 20 to 35 degrees [72], [75], so the added beam curvature would only serve to further reduce the thruster efficiency. Single-slot electrodes providing on-axis thrust are therefore better suited for TVC as the beam deflection and subsequent overspray would be minimized.

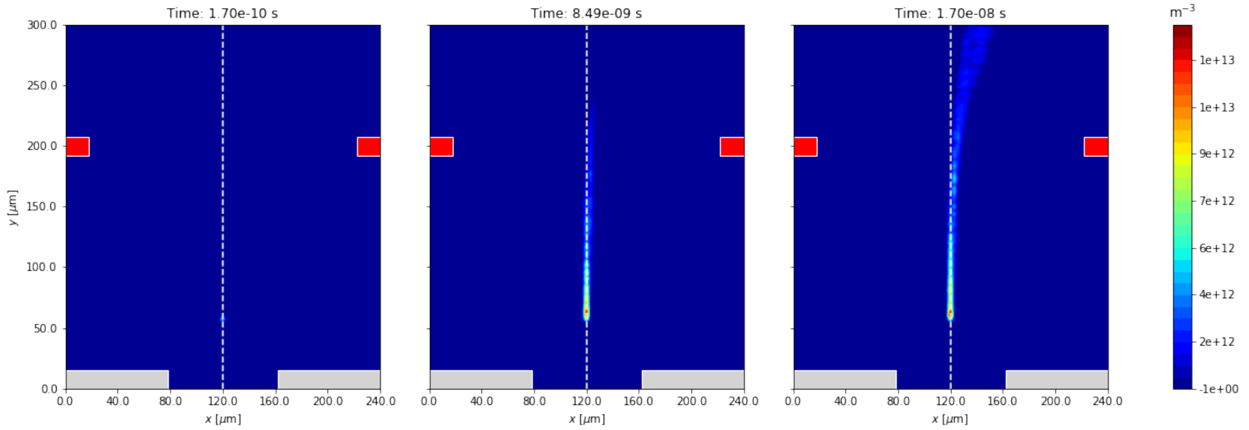

Figure 4.1: ES-PIC modeling of ion-mode thrust vectoring using electrostatic deflection of EMI-BF4. The capillary width is 80 μm, the electrode gap width is 200 μm, and the electrode distance from the capillary is 180 μm. The left electrode is set to -1800 V, while the right electrode is set to -2200 V.

4.2 Analytical Emission Profile Modeling

As discussed in Chapter 2, Wright and Wirz [82] developed an analytical model to examine the behaviour and spacing of multiplexed emission along a porous wedge. The model demonstrated how emission sites separated by 50 to 300 μm arise naturally due to pressure and electric field oscillations. The analytical model operates as follows.

Darcy's law, Eq. 2.17, subject to fluid continuity, $\nabla \cdot \mathbf{Q}_{\text{por}} = 0$, shows that the Laplacian of the pressure is zero, i.e, $\nabla^2 P = 0$. This suggests that the propellant flow within a porous wedge can be decomposed into a primary (net) radial flow along the radial axis and a secondary (oscillatory) flow along the longitudinal axis. The primary flow is driven by the primary electric field E_{p}, which is produced by the electric potential at the emitter V_{in}. The secondary flow is driven by oscillatory separation of the net flow into discrete emission sites, i.e., Taylor cones, with spacing λ. These discrete emission sites also produce secondary electric fields, however they are negligible when scaled against the primary field. The cylindrical harmonics are solved with modified Bessel functions for the exponentially decaying solutions along the radial axis and an oscillatory solution along the longitudinal axis. The net flow is found by balancing the porous flow pressure drop to the applied reservoir and Maxwell pressures:

$$\frac{\mu I_{\text{site}}}{\rho k \theta_{\text{w}} \lambda q_{\text{sp}}} \ln\left(\frac{R_2}{R_1}\right) \approx \frac{2\gamma}{R_{\text{res}}} - \frac{1}{2}\epsilon_0 E_{\text{p}}^2, \tag{4.1}$$

in which I_{site} is the current per emission site, θ_{w} is the wedge full angle, q_{sp} is the mean specific charge, R_1 is the radial distance from the virtual wedge apex to the base of the wedge, R_2 is the radial distance from the virtual wedge apex to the emission surface, and ϵ_0 is vacuum permittivity. As shown in Fig. 4.2, $R_2 = R_{\text{emit}}\left[1/\sin(\theta_{\text{w}}/2) - 1\right]$, where R_{emit} is the apex radius of curvature. Note that $\lambda \ll R_1$ is assumed [82]. By solving for the current per emission site and multiplying along the wedge length L_{emit}, Wright and Wirz [82] showed that the total emitted current can be estimated as:

$$I_{\text{total,WW}} \approx \frac{\rho k \theta_{\text{w}} L_{\text{emit}} q_{\text{sp}}}{\mu \ln\left(R_2/R_1\right)} \left(\frac{2\gamma}{R_{\text{res}}} - \frac{1}{2}\epsilon_0 E_{\text{p}}^2\right). \tag{4.2}$$

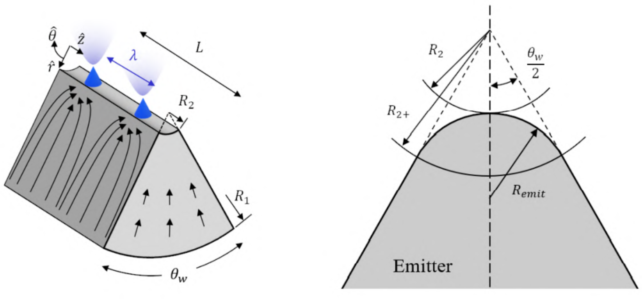

Figure 4.2: Porous prism geometry. Adapted from [82].

The primary electric field is determined by the emitter and extractor electrode geometry via:

$$E_{\mathrm{p}} = C_E V_{\mathrm{in}}, \tag{4.3}$$

in which the parameter C_E relates the voltage to the electric field. Figure 4.3 illustrates the electric potential and normalized electric field generated using COMSOL, yielding a value of $C_E = 14.3$ mm^{-1} for an emitter radius of 20 μm, a wedge full angle of 40 degrees, an extractor aperture width of 250 μm, and an extractor distance of 100 μm. Wright and Wirz [82] introduced an empirical constant $A = 5 \times 10^{-16}$ C^4 s^4 m^{-6} kg^{-2} which relates the specific charge to the emitter voltage:

$$q_{\mathrm{sp,WW}} = A\frac{E_{\mathrm{p}}^3}{\rho\gamma}. \tag{4.4}$$

However, this expression becomes invalid when the emitter voltage grows to produce a specific charge greater than the EMI-BF4 monomers, EMI$^+$ and BF4$^-$. Substituting Eq. 4.3 into Eq. 4.4 and rearranging for V_{in}, the specific charge becomes nonphysical at $V_{\mathrm{in}} = V_{\mathrm{mon}} \approx 3279$ V for a monomer specific charge of $q_{\mathrm{sp,mon}} \approx 990$ C g^{-1} (the average of the two monomers). Wright and Wirz [82] only examined the behaviour of porous wedge emitters from 1000 V to 2600 V; however, these devices commonly operate at voltages above this range [56], [85], therefore this work introduces a custom asymptotic expression to alleviate the non-physical specific charge growth when the emitter voltage approaches V_{mon}:

$$q_{\mathrm{sp,VET}} = \frac{q_{\mathrm{sp,mon}}}{2}\left[\tanh\left(\frac{V_{\mathrm{in}} - C}{B}\right) + 1\right], \tag{4.5}$$

where B and C are empirical parameters which are selected to emulate the specific charge profile in [82]. The resulting specific charge for $B = 896$ and $C = 2620$ V, optimized using the non-linear least squares curve-fitting method with the Python `scipy.optimize.curve_fit` function, is illustrated in the upper LHS of Fig. 4.4. The proposed specific charge profile closely matches that generated by Wright and Wirz [82] while asymptotically approaching the maximum physically-allowable specific charge of the monomer ions.

To estimate the minimum operating voltage required of the PPU, the onset voltage must be determined. The onset condition is met when the Maxwell pressure and reservoir static pressure are in equilibrium, i.e., the LHS of Eq. 4.1 is zero:

$$V_{\mathrm{on,WW}} = \frac{1}{C_E}\left(\frac{4\gamma}{\epsilon_0 R_{\mathrm{res}}}\right)^{1/2}. \tag{4.6}$$

The total emitted current from Eq. 4.2 as a function of the emitter voltage for all available reservoir grades is illustrated in the upper RHS of Fig. 4.4. The EMI-BF4 properties of $\rho = 1278$ kg m^{-3}, $\mu = 24$ cP, and

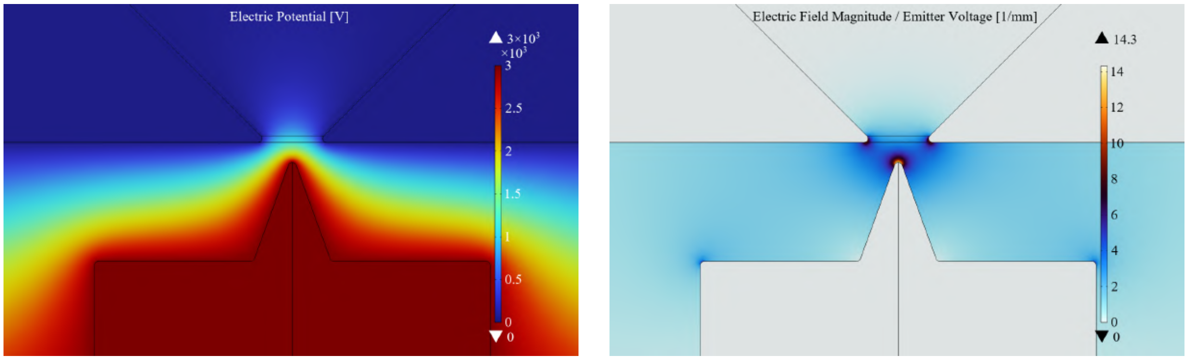

Figure 4.3: Electric potential (LHS) and normalized electric field (RHS) generated in COMSOL.

$\gamma = 49.9$ mN m^{-1} [54] as well as the reservoir radii of $R_{\text{res}}(\text{P5}) = 1$ μm, $R_{\text{res}}(\text{P4}) = 5$ μm, $R_{\text{res}}(\text{P3}) = 14$ μm, $R_{\text{res}}(\text{P2}) = 35$ μm, $R_{\text{res}}(\text{P1}) = 65$ μm, and $R_{\text{res}}(\text{P0}) = 103$ μm [83] and an emitter length of $L_{\text{emit}} = 10$ mm are used. A permeability of $k = 6 \times 10^{-15}$ m^2 is assumed [82]. Equation 4.6 is used as a lower bound on the emitter voltage and the restriction of the emitted current to below 330 μA is set by the maximum output current of the XP Power A30 converters. Notably, the theoretical onset voltage for a thruster operating with only a P5-grade substrate is well above the operating range of the A Series converters.

A model of the VET is also developed within the framework of the Electrospray Propulsion Engineering Toolkit (ESPET) [54], [55], [80] for comparison with the custom model based on Wright and Wirz [82]. The onset voltage provided by ESPET is based on an analytical solution of the Laplace equation for a hyperboloidal emission site:

$$V_{\text{on,ESPET}} = \operatorname{arctanh}(\eta)\left(1-\eta^2\right)\left[\left(\frac{2D}{\eta^2}\right)^2 \frac{1}{\epsilon_0}\left(\frac{\gamma}{R_{\text{res}}} + \frac{P_{\text{int}}}{2}\right)\right]^{1/2}, \tag{4.7}$$

where $\eta = (1 + R_{\text{emit}}/D)^{-1/2}$ and D is the distance between the emitter apex and the extractor electrode [55], [80]. The minimum volumetric flow rate required to sustain emission at onset is expressed by Eq. 2.4 [55], [80]. The hydraulic resistance of a porous wedge can be estimated as [55]:

$$Z_{\text{ESPET}} = \frac{\mu}{\theta_{\text{w}} L_{\text{emit}} k} \ln\left[\frac{R_{\text{h}} \tan(\theta_{\text{w}}/2)}{R_{\text{emit}} \cos(\theta_{\text{w}}/2)}\right], \tag{4.8}$$

where R_{h} is the prism height. The expressions for $Q_{\min}$ (Eq. 2.4) and Z_{ESPET} can be used in P_{int} (Eq. 2.18) in Eq. 4.7. The properties of $\epsilon_{\text{r}} = 12.9$ and $\sigma_{\text{e}} = 1.478$ S m^{-1} are used for EMI-BF4 and the porosity is assumed to be 0.5 [55]. The lower LHS of Fig. 4.4 compares the onset voltages calculated by Eqs. 4.6 and 4.7 for extractor distances ranging from 20 μm to 200 μm for a P5-grade substrate, while the lower RHS compares the onset voltages for reservoir pore radii ranging from 0.1 μm to 250 μm for an extractor distance of 100 μm.

A comparison of the VET propulsion profile predicted by the model based on Wright and Wirz [82] and the ESPET Domain Modeler [55] is tabulated in Table 4.1. ESPET predicts an onset voltage which is 1.8 times lower than that returned by Eq. 4.6. ESPET also predicts a droplet-dominated beam composition with a specific charge of 35.5 C kg^{-1}, which is emulative of colloid thrusters [110], whereas Eq. 4.5 suggests that the thruster is operating in the purely ionic regime.

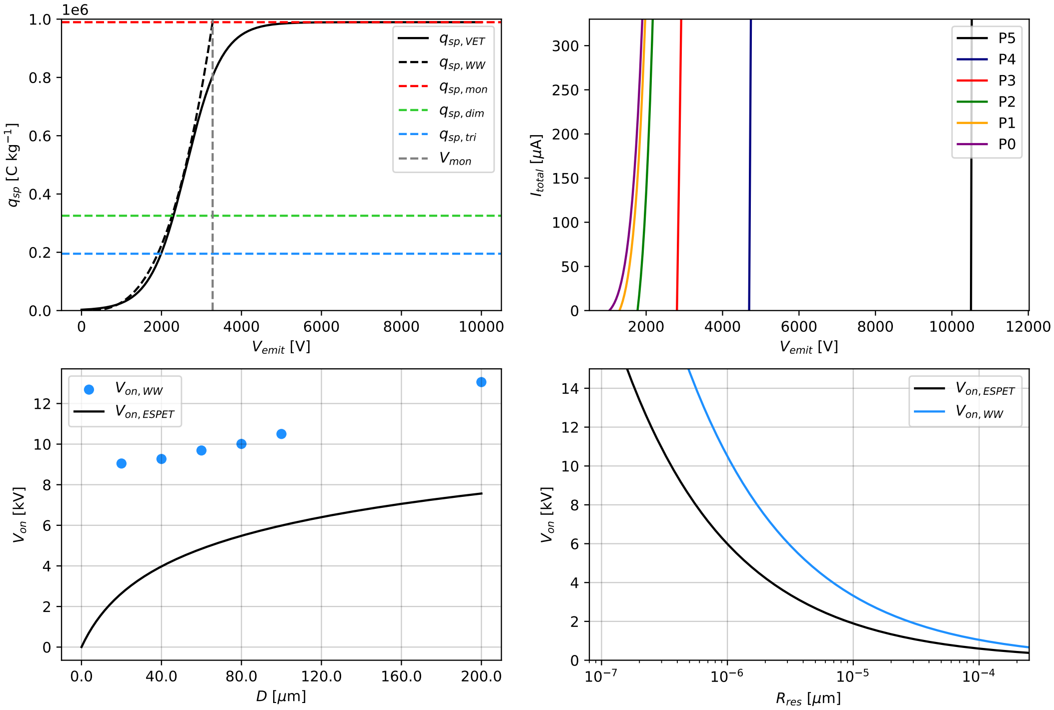

Figure 4.4: Upper LHS: specific charge as a function of emitter voltage; the monomer, dimer, and trimer specific charges are averages of their respective polar species. Upper RHS: total emitted current as a function of the emitter voltage for the full range of porous reservoir grades. Lower LHS: onset voltage as a function of the emitter to extractor distance for a P5-grade substrate. Lower RHS: onset voltage calculated as a function of the reservoir pore radius for an extractor distance of 100 μm.

As expressed in Chapter 2, knowledge of the total emitted current, specific charge, and exit velocity allows for the calculation of the torque generated by each emitter for a nanosatellite (see Fig. 2.3). Employing the values of q_{sp} and I_{total} from Table 4.1 at $V_{\text{in}} = V_{\text{on}} + 100$ V and using Eq. 2.10, the angular velocity for a nanosatellite with $L_\tau = 5$ cm and $I_\tau = 0.0065$ kg m^2 [26] after one second of firing can be estimated as $1.25\,\text{mrad}\,\text{s}^{-1}$ for the model based on Wright and Wirz [82]. The angular rate based on the thrust returned by the ESPET Domain Modeler [55] is found to be 2.56 mrad s^{-1}. These angular rates are within an acceptable range for nanosatellite attitude actuation, though it is likely that the thrust predicted by both models is an overestimate as the high-performance BET-300-P thruster, which features nine porous emitter strips, only generates up to 150 μN [69].

Table 4.1: VET propulsion characteristics for a P5-grade substrate. The emitted current is calculated at $V_{\text{in}} = V_{\text{on}} + 100$ V.

Model	V_{on} [V]	q_{sp} [C kg^{-1}]	I_{total} [μA]	T [μN]	$\Delta\omega$ [mrad s^{-1}]
Custom WW	10,500	990,000	1644	241	1.85
ESPET [55]	5987	35.5	18.1	280	2.15

In general, the analytical model developed based on Wright and Wirz [82] serves as a promising framework for estimating the VET propulsion profile. However, a more rigorous derivation of the beam composition and resulting torque will need to be produced in future investigations, as the custom model deviates from the profiles generated by ESPET. Evidently, both models agree that a single P5-grade substrate requires an operating voltage that cannot be produced by the A30 converters.

4.3 Parametric Numerical Modeling

Notably, numerical ES modeling of the VET emitter and extractor geometry directly informed the sizing of the extractor electrode aperture width. Prior to the development of this model, the aperture width was sized to an arbitrary 1 mm, as it was assumed the vertical distance from the emitter apex to the extractor plane would be the primary parameter for determining onset voltage. However, the numerical model, combined with Eq. 4.3 and Eq. 4.6, showed that minimizing the aperture width, and thus increasing the C_E coefficient, significantly reduced the onset voltage. Therefore, the aperture width was minimized to 250 μm, which was the apex width of the smallest 45-degree end mill available during fabrication. This occurrence reinforces the notion that modeling plays a critical role in the development of ESP—and, in general, any propulsion—systems.

4.4 Concluding Remarks

Efforts to model the VET current emission profile and estimate the thruster performance were presented in this chapter. Preliminary ES-PIC modeling investigated whether the thruster should use ES deflection for TVC, where it was found that the increased plume overspray would likely lead to more rapid thruster degradation. Therefore, the emission profile was kept on-axis and the method of clustering was employed to achieve TVC. Analytical modeling of the VET current emission profile was performed using two existing frameworks from literature, namely Wright and Wirz [82] and ESPET [55]. It was found that the two models agreed on the total output thrust that the VET prototype would produce, though the estimates of the specific charge were highly disparate, with one model predicting PIR emission and the other predicting a highly droplet-dominated mode. Future modeling efforts will need to reconcile the output of these models to ensure accuracy and reliability. The subsequent chapter will provide an overview of the experimental methods for characterizing the VET performance and TVC capabilities.

5 VET Experimental Characterization

Experimental characterization of the two-emitter VET prototype was performed using the RAPPEL vacuum and electrical testing suite. The vacuum equipment provided a high-vacuum environment which emulated the vacuum of space—a critical requirement for validating any spacecraft propulsion system—while the electrical suite delivered power to the PPU and provided a negative bias to the ESG.

5.1 RAPPEL Vacuum Suite

A Kurt J. Lesker bell jar vacuum chamber and its associated vacuum equipment provided high-vacuum for testing. Illustrated in the LHS of Fig. 5.1 are the vacuum chamber, vacuum pumps, and vacuum sensors. The ULVAC Technologies GLD-136A and Edwards Vacuum XDS10 dry scroll roughing pumps were used to reduce the chamber pressure to under 100 mTorr. Once this medium vacuum was achieved, a Leybold TURBOVAC 90i turbo-molecular pump, connected in series with the GLD-136A and capable of pumping 90 L s^{-1} of nitrogen, was used to reduce the chamber pressure to 10^{-5} Torr for testing, with a minimum pressure of 2.5×10^{-5} Torr being reached following one hour of pumping operation. Such a high vacuum is relevant for electrospray thruster testing [90], though state-of-the-art laboratories operate in the pressure range of 10^{-6} to 10^{-7} Torr [35], [52]. A Lesker company 275i Pirani gauge, positioned between the GLD-136A and the 90i, measured the pressure within the foreline. A Superbee CVM201 pressure gauge and a Kurt J. Lesker 354 Series hot cathode ionization gauge were used to measure the pressure within the bell jar. Figure 5.2 shows the port connections which interface with the vacuum chamber.

5.2 RAPPEL Electrical Suite

The elements of the electrical suite included the power supplies and oscilloscope. A Keysight E3633A DC power supply provided 5 V to power the PPU, while a GW Instek GPS-2303 DC power supply provided 1.25 V to the non-inverting input of the summing amplifier for providing a DC offset to the FEMTO outputs. A GW Instek GPS-4303 supplied -30 V to the ESG. A Keysight EDUX1002A 50 MHz dual-channel oscilloscope processed and displayed the FEMTO output for high-resolution waveform analysis. A diagram of the complete electrical suite is shown in Fig. 5.3.

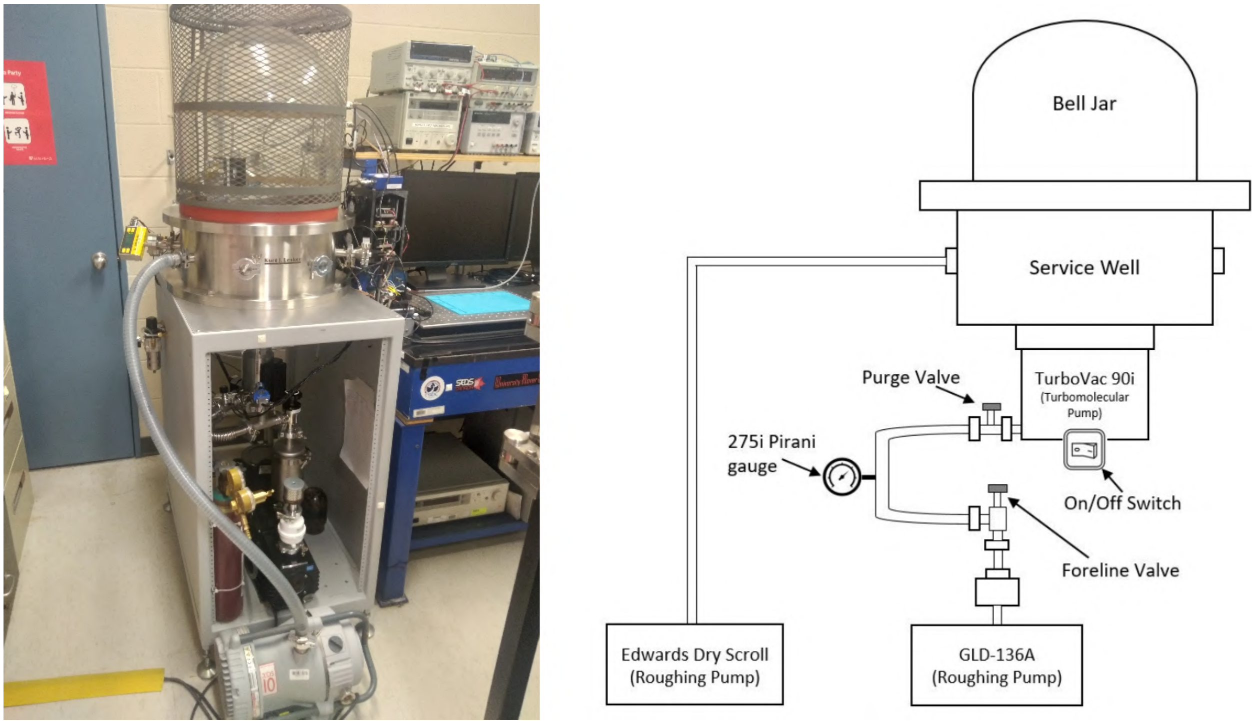

Figure 5.1: RAPPEL vacuum suite (LHS) with labeled diagram of associated equipment (RHS; sourced from RAPPEL).

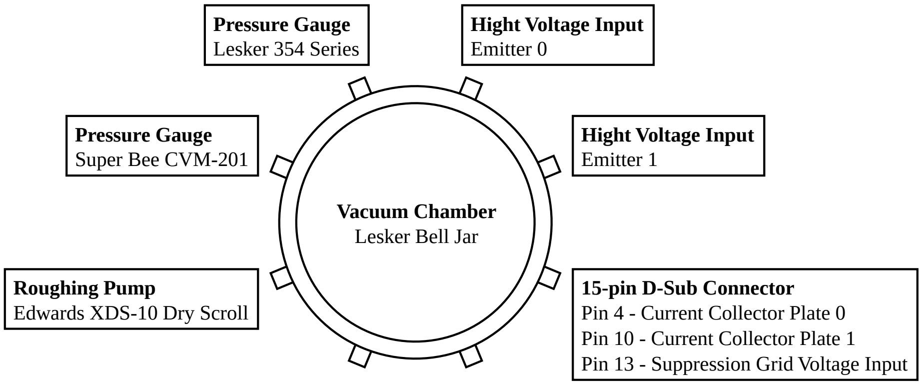

Figure 5.2: RAPPEL vacuum chamber interface ports.

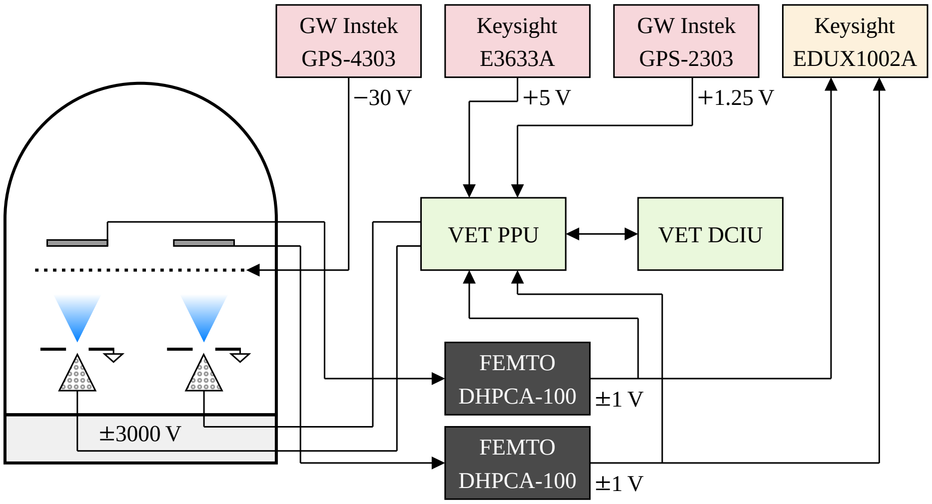

Figure 5.3: RAPPEL full electrical suite diagram.

5.3 Diagnostics Suite

The VET diagnostics suite consisted of a 0.25 in PEEK thruster mount plate, two steel current collector plates (acting as Faraday cups) secured to a similar PEEK sheet (Fig. 5.4, LHS), and an ESG secured to a similar PEEK frame (Fig. 5.4, RHS). The ESG was a Precision Eforming MN8 micro nickel mesh with 43-μm-wide wires, 30 lines-per-inch, and 90 percent transparency. Not shown in the RHS of Fig. 5.4 is the added clearance hole in the suppression grid frame that secured a ring connector to the mesh. Set screws were used to secure each of the PEEK sheets to a set of four threaded rods that were threaded into the RAPPEL thrust stand. The full assembly, labeled in Fig. 5.5, contained the VET module and diagnostics components. The extractor electrode wires were grounded to the RAPPEL thrust stand. Similar to the VET module, all fasteners used in the diagnostics suite were selected as #4-40 threads. Notably, the diagnostics suite developed for this work was developed only for collecting full-beam emitted current measurements.

Prior to connecting the FEMTO current amplifiers to the collector plates, a 100 MΩ resistive load connected to the PPU HV rails was used to verify the output waveform of the amplifiers. At 1000 V, a 100 MΩ load allows 10 μA of current to flow, which corresponds to a 1 V signal for a FEMTO gain setting of $10^5\,\mathrm{V\,A^{-1}}$. This value of 1 V was indeed recorded for such a load. This initial characterization of the amplifiers also demonstrated that their output contained significant noise at the higher gain settings beyond $10^4\,\mathrm{V\,A^{-1}}$. It was not determined whether this noise stems from the current collector plates, the amplifiers themselves, or from the oscilloscope electronics.

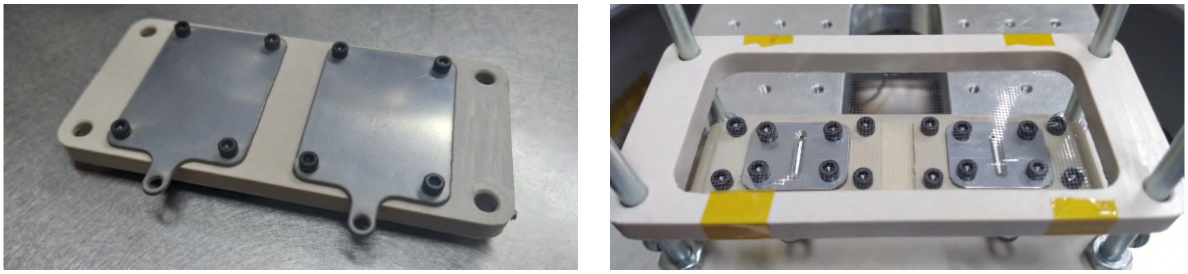

Figure 5.4: Current collector plates (LHS) and ESG (RHS).

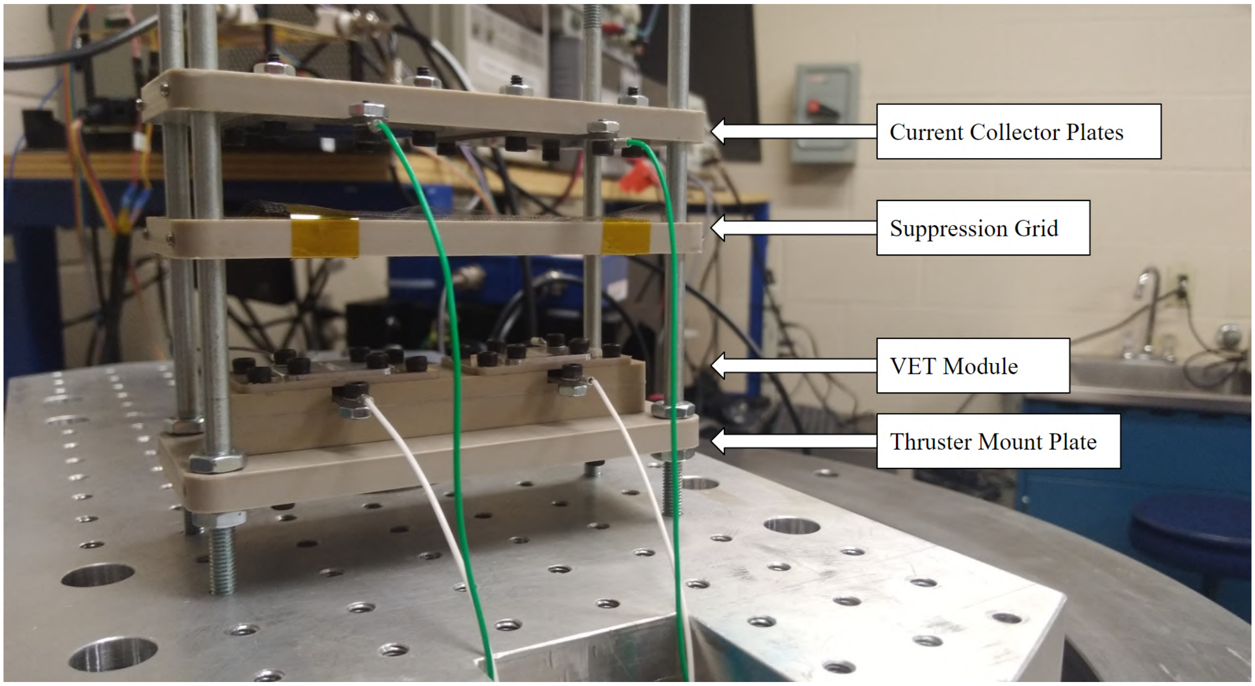

Figure 5.5: Full experimental assembly secured to the RAPPEL thrust mount in the vacuum chamber.

5.4 Assembly, Integration, and Testing

Prior to loading the wetted emitters into the thruster module, the emitters were offgassed under medium vacuum to ensure the release of any trapped air or volatile contaminants [79]. The emitters were submerged in a beaker containing EMI-BF4, and the beaker was placed in the vacuum chamber at a pressure of 100 mTorr, delivered using the Edwards roughing pump. Kapton tape was used to cover the beaker opening to prevent propellant from splashing onto and contaminating any surfaces. Once a reduction in the offgassing rate was observed, the beaker was removed from the chamber and the emitters were loaded into the thruster housing following a brief drying using a paper towel. Alignment of the emitter apex and extractor electrode aperture was performed using a Fisher Scientific stereo microscope. A Denver Instruments S-114 mass balance was used to measure the mass of the thruster and components. One emitter was measured to have a dry mass of

146 mg and a wet mass of 217 mg, therefore it can be estimated that 71 mg or 56 μL of EMI-BF4 was used per emitter. The thruster wet mass was measured to be 50.0 g.

Experimental characterization of the VET concept was executed in the following order. First, the thruster and diagnostics suite was assembled in the vacuum chamber. Next continuity checks were performed with a Fluke 179 multimeter between the low side of the PPU SRs and their corresponding distal electrodes to ensure HV would be delivered to the emitters, as well as across the distal and extractor electrodes to ensure isolation. The chamber was then brought to medium vacuum using the roughing pumps and subsequently to high vacuum using the turbo pump. The assembly then remained in high-vacuum for 30 min to ensure any residual gas which was introduced to the emitters during assembly and integration was released. The vacuum pressure was recorded following this period, and was typically around 5×10^{-5} Torr. Next, each of the FEMTO current amplifiers were cycled through their gain settings range from 10^3 V A^{-1} to 10^6 V A^{-1} to ensure their output signals were nominal. The DCIU was then activated and testing of the emitters could begin. At the end of each test, the thruster was removed from vacuum and the extractor electrodes and emitters were inspected. Lastly, all surfaces within the bell jar and on the diagnostics platform were wiped down to ensure any residual propellant would not contaminate future campaigns.

5.5 Concluding Remarks

The RAPPEL vacuum and electrical suites used for experimental characterization were detailed in this chapter. The vacuum suite, consisting of a bell jar, two roughing pumps, a turbopump, and associated vacuum sensors provided a high-vacuum to simulate the space environment. The electrical suite, composed of power supplies and an oscilloscope, provided power to the PPU and ESG and enabled high-resolution waveform analysis of the FEMTO current amplifier signals, respectively. The thruster module and thruster diagnostics suite were integrated in the vacuum chamber thrust stand, where the necessary electrical connectivity or isolation was checked with a multimeter. An estimated 71 mg or 56 μL of degassed EMI-BF4 propellant was added to each emitter for testing. The following chapter details the experimental campaign performed to validate the VET concept.

6 VET Results and Discussion

To validate the VET concept of using clustering and PWM to achieve TVC, it was essential to demonstrate (1) PWM of electrospray emission from one or both of the emitters and (2) consecutive and/or simultaneous operation of two emitters. The experimental campaign was indeed successful in validating the VET concept, and the results of PWM of a single emitter as well as the sequential and simultaneous operation of two emitters from full-beam measurements are presented in this chapter. Notably, the ESG was deactivated for all experiments.

6.1 Initial Operation

It was observed that the input lines to the SR iso-amps often experienced voltage spikes (Fig. 6.1) that reached the threshold input voltage of the iso-amps. This created noise in the PPU current measurements and occasionally caused an iso-amp to fail and require replacement. It was discovered that, despite the inclusion of the RC clamping circuits to the HV rails, the signal spikes occurred during activation of the HV signal, i.e., at the exact moment the HV rails were toggled from 0 V to ±HV. The cause of the signal spikes and failure of the iso-amps was likely due to aliasing of the fast switching HV transients with the iso-amp input sampling rate, which caused higher input offset voltages and thus damaged the internal circuitry. After consulting the iso-amp datasheet, it was found that the manufacturer suggested the inclusion of an RC anti-aliasing circuit directly on the iso-amp input pins. A breadboard prototype which contained 39 Ω resistors at each of the iso-amp input pins did indeed demonstrate a significant reduction in the signal spike magnitude. However, the existing PCBs which lacked anti-aliasing components were ultimately used as there was concern of catastrophic failure due to short-circuiting across the breadboard ties.

To smooth the PPU current measurements, a Savitsky-Golay finite impulse response digital smoothing filter that used least-squares polynomial fitting [111] was applied to all of the PPU current data. The Python function `scipy.signal.savgol_filter` with a window length of 3 and a polynomial order of 1 was used and the output of the filter for a single P4-grade emitter is shown in Figure 6.1. For comparison, a sample of the FEMTO output signal for a subsequently-tested P5-grade emitter which was captured on the oscilloscope for a FEMTO gain setting of $10^5\,\mathrm{V\,A^{-1}}$ is shown in Fig. 6.2. The higher sampling and display rate of the oscilloscope shows the current fluctuations and signal noise more clearly. While the signal does contain noise, it does not contain the signal spikes found in the PPU output. Indeed, throughout all of the oscilloscope data captured and analyzed, significant signal spikes such as those in Fig. 6.1 were not observed, suggesting that the artefacts in the PPU current measurements are a result of flaws in the PPU circuitry rather than large emission events. However, as seen in Fig. 6.2, signal spikes (e.g., at 13 s) can be observed that suggest either a drop in the electrospray emission current or a signal loss due to an error with either the FEMTO amplifiers or oscilloscope electronics.

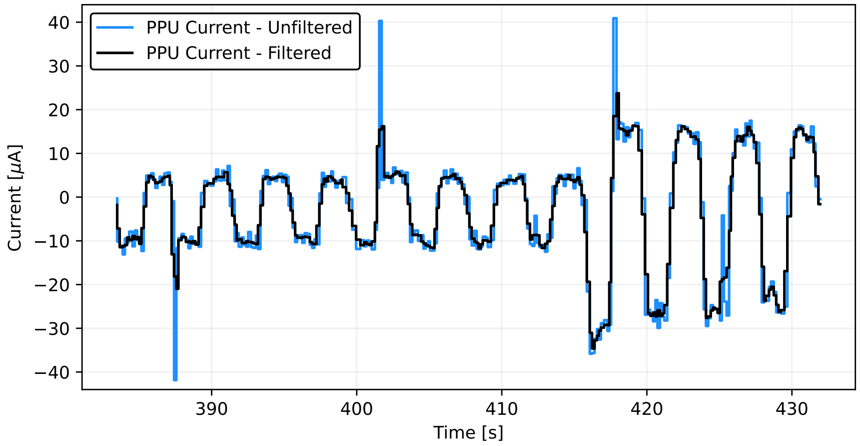

Figure 6.1: Application of a Savitzky-Golay filter with window width 3 and polynomial order of 1 to the PPU current measurements collected during testing of a single P4-grade emitter.

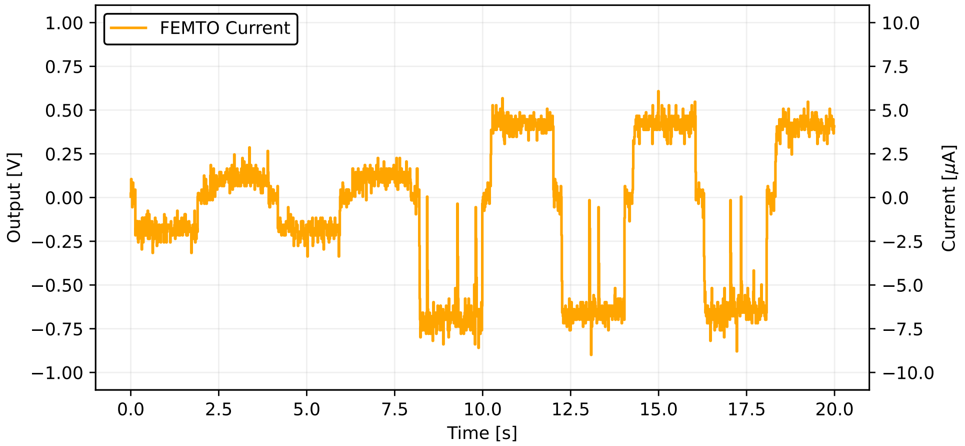

Figure 6.2: Oscilloscope waveform of FEMTO current measurements at a gain setting of $10^5\,\mathrm{V\,A^{-1}}$ for a P5-grade emitter.

In a preliminary test of a P4-grade emitter pair, the influence of the distance between the VET module and current collector plates was also characterized. In this initial test, the current collector plates were placed at a distance of approximately 8 cm from the VET module, similar to that shown in Fig. 5.5. It was observed that the exhaust plume of one of the emitters could be measured by both collector plates. This is illustrated in Fig. 6.3, which shows a plot of the data collected by the FEMTOs and exported from the oscilloscope. Note that this data was filtered using the Savitsky-Golay filter. The Emitter 1 (E1) FEMTO data is a scaled down profile of the Emitter 0 (E0) FEMTO data, with near-identical signal spike profiles seen at 7.6, 7.9, 11.9, 13.3, 15.9, and 16.5 s. Following this test, the current collector plates were brought to within 2 cm of the VET module and no cross-collection was observed in subsequent tests.

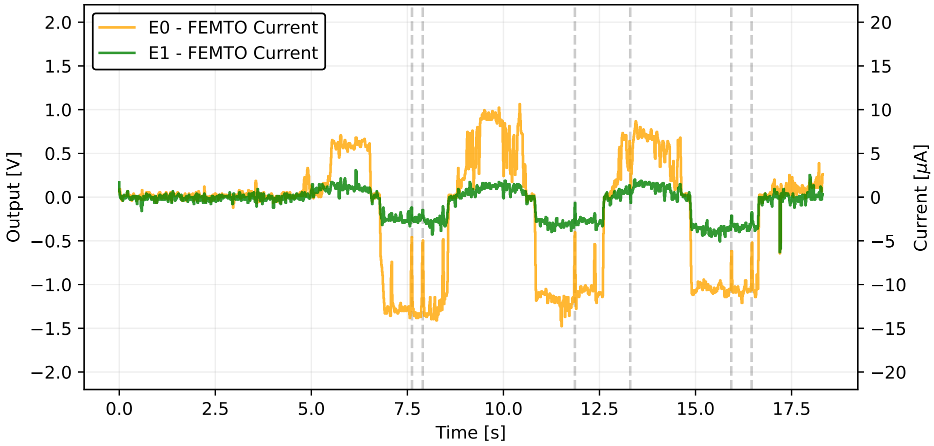

Figure 6.3: Oscilloscope current measurements from both FEMTO current amplifiers at a gain setting of $10^5\,\mathrm{V\,A^{-1}}$ for a single P4-grade emitter. While both amplifiers returned a signal, only one emitter was activated, suggesting that the emission plume from the active emitter crossed over the central plane of the assembly and was measured at the other current collector plate.

6.2 Single Emitter Operation

Figure 6.4 illustrates a single P4-grade emitter lifetime test, demonstrating a stable current output as well as an increase in current with an increase in voltage. The onset voltage for the P4-grade emitter is estimated to be +1050 V and −1100 V for the positive and negative modes, respectively. This onset voltage is several thousands of V lower than that predicted in Chapter 4. As shown in Fig. 6.4, emission occurred at approximately 355 s, directly after a command was given to increase the voltage setting. From 355 s to 460 s, the emitter generated a stable output current, with an approximately threefold increase in both PPU and FEMTO current being observed at 415 s. The maximum measured current by the PPU and by the FEMTO current amplifiers in each polarity is tabulated in Table 6.1. As shown, a maximum negative current of −34.6 μA, with a corresponding FEMTO measurement of −11.5 μA, and a maximum positive current of +23.8 μA, with a corresponding FEMTO measurement of +10.6 μA, was measured by the PPU. On the other hand, a maximum negative current of −20.4 μA, with a corresponding PPU measurement of −21.8 μA, and a maximum positive current of +17.2 μA, with a corresponding PPU measurement of +19.2 μA, was measured by the FEMTOs. In addition, the successful operation of the emitter validated the mechanical design choice introduced in Chapter 3 of not including a porous reservoir.

Notably, the output current measured by both the PPU and the FEMTO is asymmetric, where the current emitted in the negative polarity is greater in magnitude than in the positive polarity—this output is also demonstrated in Fig. 6.1. The cause of this asymmetry is due to the asymmetric HV output between the A30 converters, where the A30N-5 (−3000 V) converter output a HV approximately 100 V greater in magnitude relative to the A30P-5 (+3000 V) for the same command voltage from the DCIU. This had the effect of throttling the output current to a higher absolute value, which resulted in an asymmetric current output.

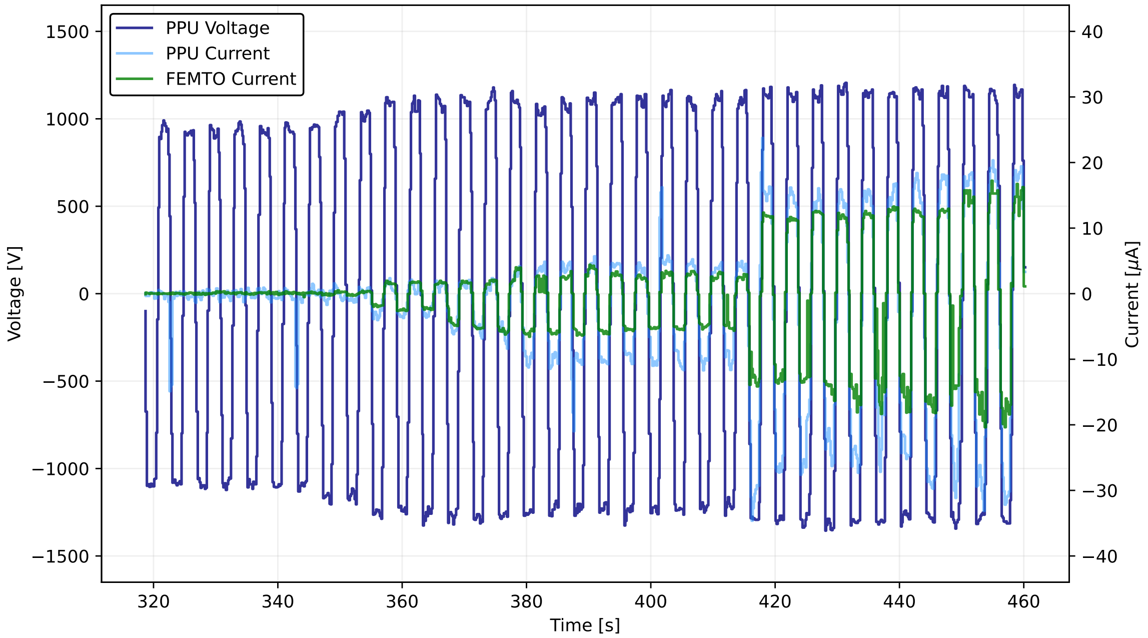

Figure 6.4: Lifetime testing of a single P4-grade emitter.

Table 6.1: Lifetime testing of a single P4-grade emitter based on data from Fig. 6.4. The maximum dual-polarity current measured by the PPU and the corresponding voltage, time, and FEMTO current are shown in the upper section. The maximum dual-polarity current measured by the FEMTO current amplifiers and the corresponding voltage, time, and PPU current are shown in the lower section.

Source	PPU Current [μA]	Voltage [V]	Time [s]	FEMTO Current [μA]
PPU Pos	+23.8	+1209	418	+10.6
PPU Neg	−34.6	−1276	416	−11.5
Source	**FEMTO Current [μA]**	**Voltage [V]**	**Time [s]**	**PPU Current [μA]**
FEMTO Pos	+17.2	+1156	455	+19.2
FEMTO Neg	−20.4	−1293	454	−21.8

Notably, there was often a significant difference between PPU current measurements and the FEMTO measurements. For example, in Fig. 6.4, the negative mode PPU current measured from 416 s to 458 s is roughly double of that measured by the FEMTOs. The discrepancies between the PPU current measurements and FEMTO measurements are evidence of significant inefficiencies in electrospray emission. As discussed in Chapter 3, the emitter apexes were trapezoidal rather than pointed. Such a shape would concentrate the electric field to the sharp corners of the trapezoid and thus lead to off-axis emission, perhaps even directly at the extractor electrodes. Indeed, Fig. 6.5 shows closeup images of the extractor electrode (LHS) and P4-grade emitter (RHS) and shows proof of propellant decomposition following the test. This decomposition is typically a result of short-circuiting between the emitter and extractor electrode and indicates that propellant was being emitted off-axis such that it would impinge on the extractor and create an electrical pathway.

To meet the PWM requirement for TVC, PWM commands were transmitted to one of the emitters once stable emission had been achieved. Figure 6.6 demonstrates PWM of a single P5-grade emitter. As expected, the duty cycle of the emitted and collected current strongly matches the duty cycle of the voltage setting at all four PWM settings of 100, 75, 50, and 25 percent. Notably, the PPU current occasionally signifies current flowing when the voltage setting is low. For example, at 260 s the PPU current reads approximately 2.4 μA, but the PPU voltage reading and the FEMTO current reading are both zero. It was not determined why the PPU was measuring current at that time. Nonetheless, the FEMTO current readings clearly demonstrate PWM of a single emitter. Note that the Savitsky-Golay filter was not applied to the PPU voltage measurement data for this test.

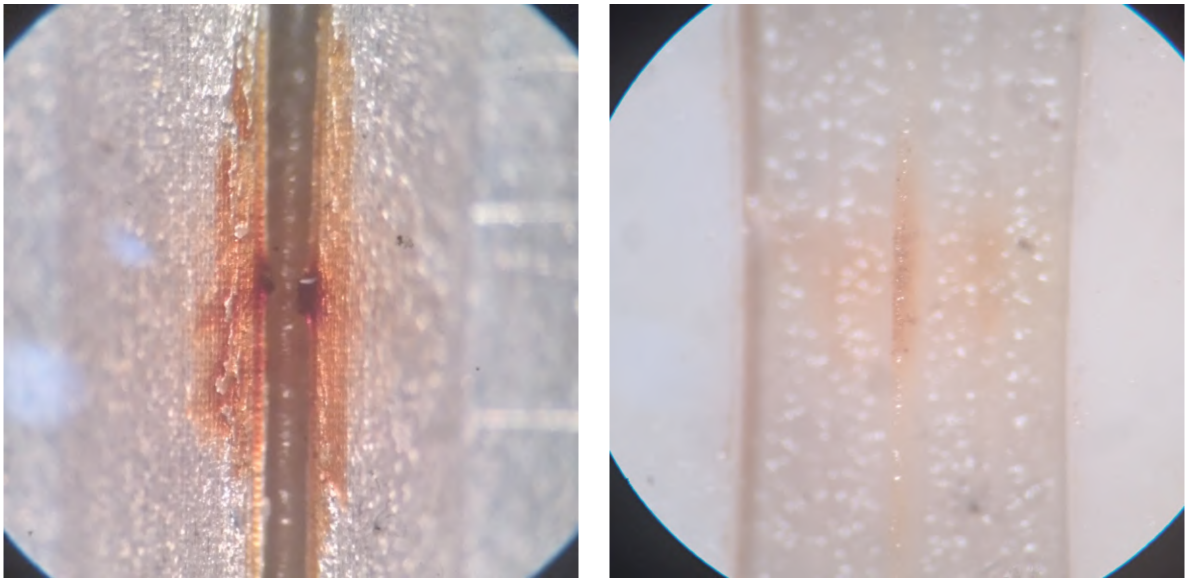

Figure 6.5: Evidence of propellant decomposition after firing. The LHS shows decomposed propellant along the extractor electrode aperture, while the RHS shows decomposed propellant at the P4-grade emitter apex.

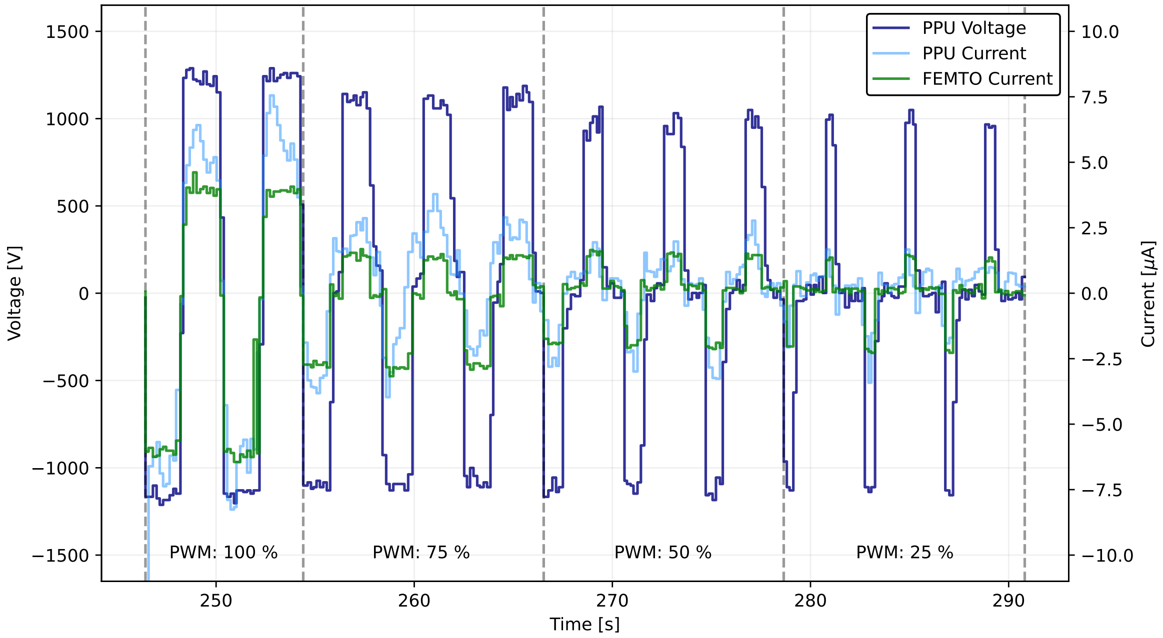

Figure 6.6: PWM of a single P5-grade emitter.

6.3 Dual Emitters Operation

To meet the clustering requirement of the VET concept, two emitters were operated both sequentially and simultaneously. Figure 6.7 illustrates the PPU voltage, PPU current, and FEMTO current measurements for two P4-grade emitters. The LHS of Fig. 6.7 plots the PPU voltage and FEMTO current measurements from 33 s to 81 s, while the RHS is a temporally magnified subset of the LHS from 69 s to 74 s and also includes the PPU current measurements. As shown in the LHS, both emitters were active at 100 percent duty cycle, with one of the emitters, E0, emitting roughly ±1.0 μA in both polarities. At 47 s, E0 was toggled off, E1 was left active, and a command was transmitted to increase the HV setting. At 63 s, a HV command was transmitted to again increase the HV setting, and stable emission of ±2.0 μA from E1 was observed. With both emitters having sequentially demonstrated emission, a command to reactivate E0 at 71 s was transmitted. Following this command, the HV rails to both emitters were activated in the negative polarity, though only the FEMTO current amplifier measuring E0 actually collected current. This was immediately followed by a short-circuit event in the E0 line, as shown in the E0 PPU voltage signal of the LHS, and the test was terminated. Notably, the RHS of Fig. 6.7 demonstrates that the PPU measured current through both emitters, where E0 emitted -7.0 μA and E1 emitted -2.5 μA; however, only the current emitted by E0 was measured at the collector plates, but at a lower -3.0 μA. This demonstrates that, while both emitters were simultaneously active and emitting, they were both emitting primarily off-axis. In addition, it is theorized that the output power of the A30s was driven to the short-circuiting emitter, which would have possessed a lower electrical resistance (order of 1 S m^{-1}), and thus would have prevented the other emitter from receiving enough power to operate nominally. As mentioned previously, the cause for the off-axis emission and subsequent short-circuiting is

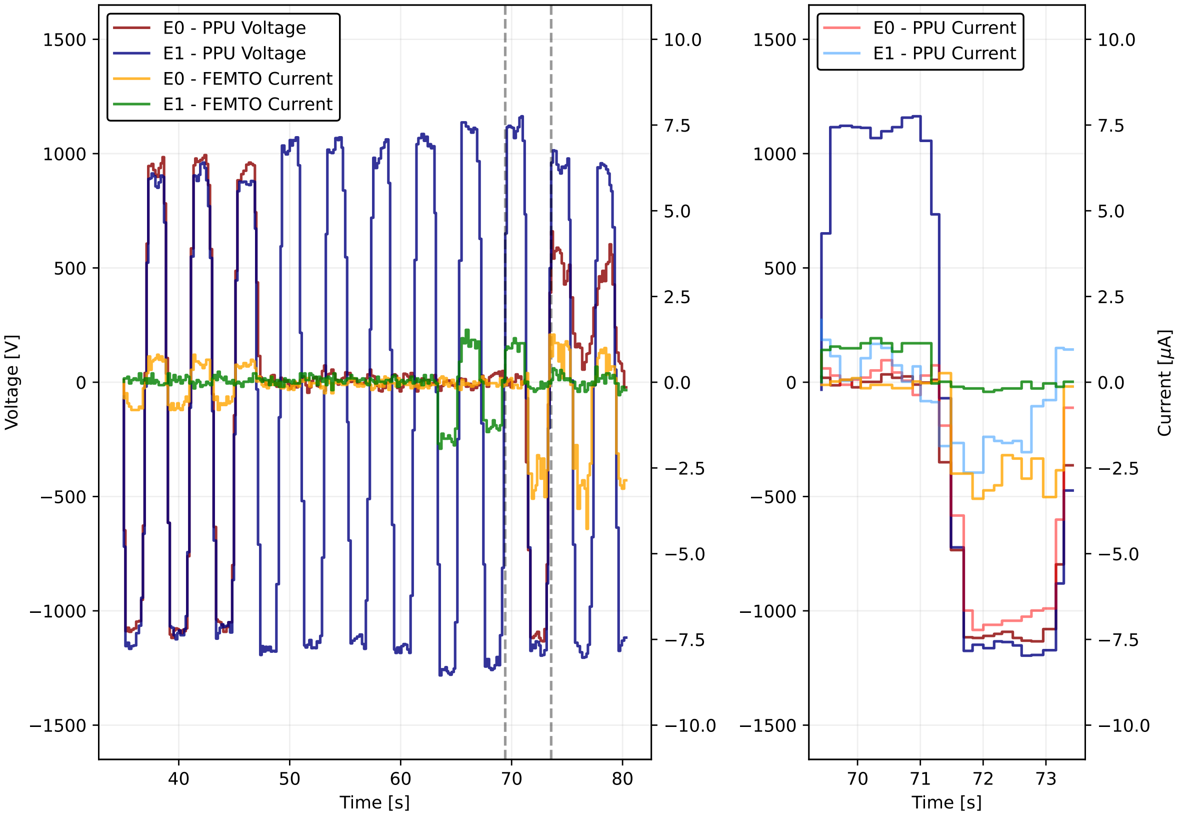

Figure 6.7: Sequential and simultaneous operation of two P4-grade emitters. The LHS plot shows the PPU voltage and FEMTO current measurements, while the RHS plot resolves the dual-polarity waveform measured from 69 s to 74 s and includes the PPU current measurements.

likely due to the trapezoidal and nonuniform shape of the emitter apexes. Indeed, several attempts were made throughout the experimental campaign to simultaneously operate both P4-grade and P5-grade emitter pairs, but these tests were terminated prematurely due to short-circuiting.

Figure 6.8 illustrates another attempt made at simultaneous operation with a pair of P4-grade emitters. This test was performed early on the in test campaign and with the FEMTO current amplifiers active but not being monitored by the PPU, therefore only the PPU voltage and PPU current measurements are present. As shown, both HV rails were activated with a voltage of ±750 V, but emission was observed only from E0. A HV-setting-increase command was transmitted at 45 s in an attempt to reach the onset voltage of E1 while maintaining emission from E0; however, the PPU current measurement began to approach $\pm 40\,\mu$A, beyond which the voltage across the SR would exceed the voltage input that could be measured by the iso-amps. Rather than increase the HV setting further to achieve emission from E1, at 65 s the E1 HV rail was deactivated and E0 was allowed to operate for another five cycles before the test was terminated.

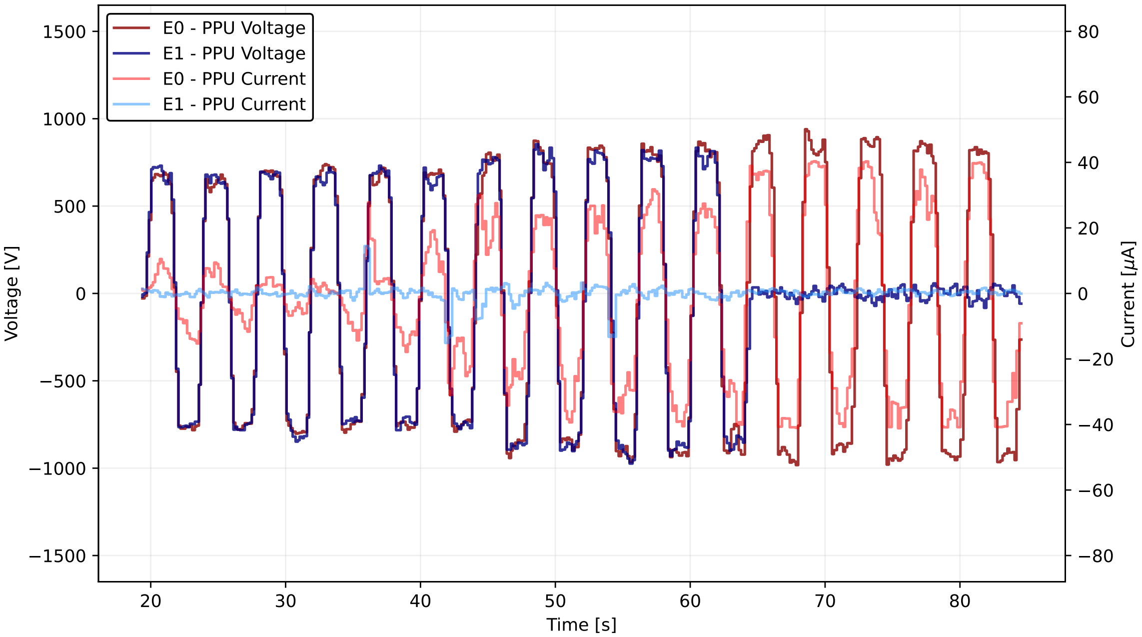

Figure 6.8: Attempt at simultaneous emission with two P4-grade emitters.

6.4 Performance Estimate

An estimate of the VET performance profile was calculated based on the measured emitted current and applied voltage as well as an assumption of the specific charge for each porous grade. Table 6.2 tabulates the estimated thrust (Eq. 2.7), specific impulse (Eq. 2.8), and change in angular velocity (Eq. 2.10) for both emitter grades. Due to the significant overspray observed, the maximum FEMTO current measurements—rather than the PPU current measurements—were used. The specific charges in each polarity for the P5-grade emitter are based on the beam composition determined using ToF measurements from Courtney et al. [52], where the percentages for each EMI-BF4 ion species from $n = 0$ to $n > 3$ in the study were used to compute an average specific charge. Note that a simplification was made to apply the $n > 3$ percentages as only $n = 3$ species. In contrast, the specific charge for the P4-grade emitter is estimated by simply applying a 50 percent reduction to the P5-grade specific charge. To the best knowledge of the author, there are no ESP publications which characterize P4-grade emitters, other than the investigation performed by Ma et al. [35], which reports an increase in specific charge when using P4-grade emitters. The ESPET Domain Modeler [54] was also consulted to provide a specific charge estimate, though it was found that a specific charge of 421,000 C kg^{-1} was returned regardless of porous emitter type (cone versus wedge) or porous emitter grade (P0 to P5).

As shown in Table 6.2, the P4-grade emitters were estimated to produce an average 2.01 μN of thrust at an average specific impulse of 2135 s, whereas the P5-grade emitters were estimated to produce an average thrust of 0.43 μN at a specific impulse of 3089 s. For an operating time of $\Delta t = 1$ s, these results lead to an average $\Delta\omega$ of 15.5 μrad s^{-1} for the P4-grade emitters and an average $\Delta\omega$ of 3.3 μrad s^{-1} for the P5-grade emitters, which are both relevant for nanosatellite attitude actuation [26]. Notably, the disparity in thrust

Table 6.2: Estimated VET performance specifications for individual P4-grade and P5-grade emitters.

Porous grade	V_{in} [V]	I_{emit} [μA]	q_{sp} [C kg^{-1}]	T [μN]	I_{sp} [s]	$\Delta\omega$ [μrad s^{-1}]
P4 Pos	+1159	+17.2	185,688	1.92	2115	14.8
P4 Neg	−1090	−20.4	205,114	2.10	2156	16.2
P4 Avg	±1125	±18.8	195,391	2.01	2135	15.5
P5 Pos	+1224	+4.6	371,375	0.37	3074	2.9
P5 Neg	−1129	−6.4	410,228	0.48	3103	3.7
P5 Avg	±1177	±5.5	390,802	0.43	3089	3.3

between the porous grades was likely a function of the difference in their respective total emitted currents, rather than the performance characteristics of the porous grades themselves.

The total emitted current measured experimentally can also be compared to that predicted via analytical modeling in Chapter 4. For the P5-grade emitters, the total emitted current measured was 300 times lower than what was predicted by the Wright and Wirz [82] framework and 3 times lower than what was predicted by the ESPET [55] framework. Under the assumption that the P5-grade emission mode is closer to being in the PIR than in colloid mode [52] and thus may be more accurately predicted by the Wright and Wirz [82] framework, it is therefore likely that the total output current of the emitters is low due to a scarcity of multiplexed emission sites. Indeed, given the nonuniformity of the emitter apexes and the regular short-circuiting observed during the experimental campaign, it may be concluded that a low number of preferred flow cells along each apex from which emission occurred were established, leaving the remainder of the wedge apex inactive. Nonetheless, the measured output current for both P4-grade and P5-grade emitters is strongly consistent with the measurements taken by Courtney et al. [83] for single-strip porous wedge P5-grade emitters coupled to various reservoir grades and using EMI-BF4 and EMI-Im propellants. In that study, a nominal output current of ±20 μA of EMI-BF4 species was observed at +1650/−1750 V and +1900/−2050 V for P1-grade and P4-grade reservoirs, respectively, with maximum output currents reaching ±50 μA when using a P3-grade reservoir. Furthermore, ToF measurements suggested a specific impulse of over 3000 s when using a P3-grade reservoir with EMI-BF4 as well as 2300 s when using a P4-grade reservoir with EMI-Im. This suggests that the measured output currents and predicted specific impulses for the VET prototype are, at minimum, on the same order of magnitude as what was measured for other single-strip porous wedge emitters.

6.4.1 Error Analysis

Error analyses based on systematic or random measurement errors of the PPU HV, PPU current, and FEMTO current measurements were not explicitly performed, though an estimate of these errors can be provided. The primary sources of error in the PPU measurements stems from inconsistencies in the reference voltage for the iso-amps, which would scale the output signal, and significant signal noise on the iso-amp input lines due to a lack of effective filtering. A reference voltage of 5.00 V was assumed, such that every ±0.05 V of difference in the actual reference voltage would result in a 1 percent systematic error of the iso-amp output signal. Regarding the FEMTO current amplifiers, the signal noise at 10^5 V A^{-1} based on Fig. 6.2 can be estimated to be ±2.0 μA, which can be a significant portion of the total current emitted by each of the emitters.

Uncertainty in the beam specific charge is the major source of error in determining the thrust (Eq. 2.7) and specific impulse (Eq. 2.8) of the thruster prototype. An assumption of the specific charge based on literature was made, but because no method of determining the beam composition was employed in this work, the thruster operating mode remains unknown. Were the thruster to have operated in droplet mode, the thrust and therefore the $\Delta\omega$ would be much greater, though at the expense of a significantly lower specific impulse. In contrast, were the thruster to have operated in the PIR, the specific impulse would would be much greater, but at the expense of a lower thrust.

6.5 Future Considerations

Many of the design elements implemented in the VET prototype proved to be successful. The first rounds of in-house CNC-milled porous emitters have been promising, and it is expected that future iterations will yield sharper and more uniform results. The VET PPU generated the HV rails necessary for extended electrospray emission, and provided an excellent framework for meeting nanosatellite SWaP demands. Parametric numerical ES modeling of the thruster also proved useful in defining the mechanical design. Nonetheless, improvements to the thruster mechanical and electrical design as well as the diagnostics suite and modeling architectures can be implemented to ensure optimized and robust performance levels.

6.5.1 Mechanical

As discussed in Chapter 2, a common life-limiting mechanisms of electrospray thrusters, including the thruster developed in this work, is short-circuiting of the propellant between the emitter and extractor electrode [36]. The two primary mechanical design elements to consider for mitigating short-circuiting are the sharpness and uniformity of the emitter apex and the alignment of the emitter apex with the extractor electrode aperture. The trapezoidal and nonuniform emitter tips used in this work likely caused the low emission current levels, due to highly concentrated flow along one low-resistance path, and regular short-circuiting, due to off-axis emission, observed in this research. In addition, while the alignment scheme implemented in this thruster design proved sufficient, the inclusion of a digital microscope capable of field and depth measurement would have allowed for precise alignment of the emitter and extractor electrode. Another critical improvement needed is reproducibility across mechanical parts and assemblies; for example, the variance in the emitter onset voltages indicates that the emitter profiles and/or emitter and extractor electrode alignment was not reproduced across the two sources. The tabbed distal electrode with a ring connector interface also proved troublesome as the design allowed for a bending moment to be produced whenever there was significant tension on the wire, which ultimately displaced the emitter. The displacement itself may be a result of either the PEEK lid deforming, or the lower compression spring deforming, or a combination of both mechanisms. Regarding a flight-qualified prototype, a vibration-proof design which maintains alignment of the emitter apex and extractor electrode aperture during launch and deployment is needed.

6.5.2 Electrical

The primary electrical design elements to consider in future PPU iterations are conditioning of the HV rails and managing over-current and short-circuit protection. The PPU required a reset each time a short-circuit event occurred, and the iso-amps were regularly destroyed due to current spikes or short-circuiting. The inclusion of appropriate filtering elements as well as active current-limiting circuitry and software which managed such events would have resulted in a more robust design and a smoother experimental campaign. Another critical disadvantage with the PPU is that the HV converters only output 330 μA at ±3000 V. This means that each emitter is limited to a maximum current input of 165 μA. This is less of a concern for a single emitting prism, but would cause a significant limitation for scaled arrays of porous emitters, which can draw anywhere from several hundreds of μA [79], [101] up to a few mA [35]. Additional improvements to the PPU include the use of surface mount device (SMD) electronics to better meet CubeSat volume constraints, use of vacuum-rated and radiation-hardened components which may operate in space missions, increased data collection rates by the DCIU that characterize signal transients with greater resolution, and the inclusion of a feedback controller which uses the iso-amp outputs to stabilize the HV signal to each emitter or operate at a specified voltage, current, or thrust setting.

6.5.3 Diagnostics

Measurements of the output current are insufficient to fully characterize the thruster emission profile. To determine the thrust, specific impulse, and efficiency of the thruster, either direct measurements of the thrust and mass flow rate or plume composition measurements of the electrospray beam will need to be performed. Direct thrust and mass flow rate measurements for ESP systems are challenging as the output thrust is on the order of μN and the flow rates are typically on the order of ng s^{-1} [76], therefore beam composition measurements, such as ToF, should be employed. ToF measurements of the thruster emission profile would allow for indirect calculation of the thrust (Eq. 2.15) and mass flow rate (Eq. 2.16). Furthermore, spatial current density mapping of the multiplexed electrospray emission from the porous wedges with translating wire probes or Faraday cup arrays would allow for determining the uniformity of the electrospray emission and characterizing the effectiveness of the CNC milling technique. Finally, measurements of the extractor electrode current will be critical for determining the rate of propellant overspray.

6.5.4 Modeling

The analytical model developed in Chapter 4 provided preliminary estimates of the thruster emissions profile, though the disparity in the specific charge and output current between the Wright and Wirz [82] framework and the ESPET [55] application will need to be reconciled to ensure the models are accurate. This can be accomplished with more rigorous derivations of the multiplexed emission model developed by Wright and Wirz [82], as well as a more thorough investigation of the equations used by the ESPET modeller to determine which parameters are contributing to the droplet-dominated emission profile estimate. Furthermore, the onset voltage of the prototype developed herein was close to an order of magnitude lower than what was predicted by the analytical modeling, suggesting that the geometry employed in the model was not representative of the fabricated prototype dimensions. Other types of electrospray models may also be pursued. The two-dimensional EHD developed by Mallalieu [53] may be expanded on into three dimensions to develop a three-dimensional EHD model of multiplexed emission from a porous wedge. Such a model could characterize the propellant flow and electric field fluctuations at the wedge apex self-consistently, and would greatly complement the existing porous ESP literature.

6.5.5 Multi-axis Attitude Actuation

Though the two-emitter thruster prototype validated the use of clustering and PWM of porous wedge emitters to achieve single-axis attitude control, the prototype still retains two degrees of rotational freedom. A next-generation nanosatellite-rated prototype would need to provide multi-axis attitude control, similar to the NANO AR3 [87] and TILE [91], to further complement the nanosatellite ADCS. A four-emitter VET prototype which offers dual-axis attitude actuation for a CubeSat assembly is illustrated in Fig. 6.9. The use of porous wedge emitters would maximize the output thrust, as the wedges would provide natural multiplexed emission, and the placement of the emitters to the edges of the CubeSat propulsion plane would allow for a maximum torque to be generated per axis.

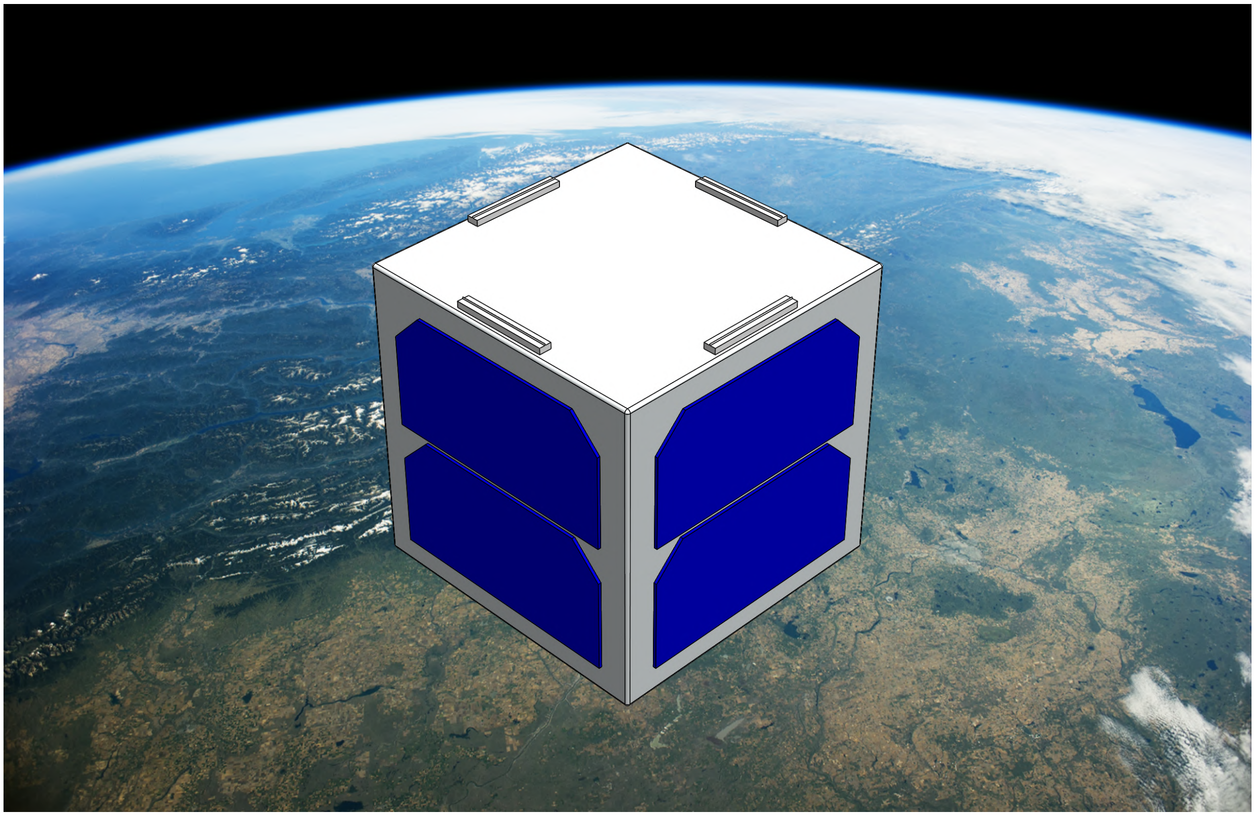

Figure 6.9: CubeSat assembly with the placement of four porous wedge emitters. This configuration would allow for multi-axis attitude actuation.

7 Conclusion

ESP systems are a promising technology for nanosatellites. These devices operate at exceedingly high specific impulses, require very little electrical power and few—if any—propellant management components, and are packaged in highly-miniaturized form factors, making them ideally-suited to meet nanosatellite SWaP constraints. Furthermore, ESP devices may implement TVC to provide greater propulsive versatility, as the increased overlap of the propulsion and attitude control systems is conducive for next-generation nanosatellite missions that require high-resolution impulse and torque maneuvers. To this extent, the VET was developed to meet the attitude and trajectory control requirements of these next-generation missions. The VET concept is based on employing multiplexed emission from porous borosilicate glass wedge emitters and using the principles of clustering and PWM control to achieve high-resolution TVC.

The design, fabrication, and experimental characterization of a two-emitter VET prototype offering single-axis attitude actuation was carried out. A novel thruster housing was designed and the porous wedge emitter profiles were fabricated using conventional CNC fabrication. A custom PPU was developed to generate the HV rails necessary for electrospray emission, and a custom DCIU was built to transmit TC to and receive TM from the PPU. In addition, a tailored experimental suite that measured the emitted current was built, and an experimental campaign was carried out at the RAPPEL testing facility. The campaign successfully demonstrated PWM of a single emitter as well as sequential and simultaneous operation of two emitters, ultimately validating the VET concept. As such, this prototype may serve as a foundation for future research initiatives to develop high-performance nanosatellite propulsion systems.

References

[1] G. P. Sutton and O. Biblarz, *Rocket propulsion elements.* John Wiley & Sons, 2016.

[2] J. R. Wertz, D. F. Everett, and J. J. Puschell, *Space mission engineering: the new smad.* Microcosm Press, 2011.

[3] P. L. Wright, "Porous electrospray fluid mechanics," 2022.

[4] R. Hofer, H. Kamhawi, P. Peterson, *et al.*, "Development and qualification of a 12-kw hall thruster for deep-space missions," *Impulse (s)*, vol. 12, no. 600, p. 590, 2022.

[5] C. Bashnick, "Real-time autonomous model predictive control of spacecraft rendezvous and docking with moving obstacles," Carleton University, 2022.

[6] C. Bashnick and S. Ulrich, "Fast model predictive control for spacecraft rendezvous and docking with obstacle avoidance," *Journal of Guidance, Control, and Dynamics*, pp. 1–10, 2023.

[7] I. Savytskyy and M. Jugroot, "Design and modeling of a vectored electrospray thruster," in *ASCEND 2022*, 2022, p. 4271.

[8] B. Yost, S. Weston, G. Benavides, *et al.*, "State-of-the-art small spacecraft technology," 2021, National Aeronautics and Space Administration Technical Report.

[9] K. Lemmer, "Propulsion for cubesats," *Acta Astronautica*, vol. 134, pp. 231–243, 2017.

[10] D. M. Goebel and I. Katz, *Fundamentals of electric propulsion: ion and hall thrusters.* John Wiley & Sons, 2008.

[11] J. L. Rovey, C. T. Lyne, A. J. Mundahl, *et al.*, "Review of multimode space propulsion," *Progress in Aerospace Sciences*, vol. 118, p. 100 627, 2020.

[12] D. A. Herman, T. Gray, I. Johnson, S. Hussein, and T. Winkelmann, "Development and qualification status of the electric propulsion systems for the nasa ppe mission and gateway program," in *37th International Electric Propulsion Conference*, 2022.

[13] I. Levchenko, K. Bazaka, Y. Ding, *et al.*, "Space micropropulsion systems for cubesats and small satellites: From proximate targets to furthermost frontiers," *Applied Physics Reviews*, vol. 5, no. 1, p. 011 104, 2018.

[14] E. Kulu, *Nanosats database*, https://www.nanosats.eu/, 2023.

[15] B. Cheetham, T. Gardner, A. Forsman, E. Kayser, and M. Clarkson, "Capstone: A unique cubesat platform for a navigation demonstration in cislunar space," in *ASCEND 2022*, 2022, p. 4382.

[16] Z. Pavanello, "Development and analysis of a pitch sun tracking attitude mode for the 2u cubesat orcasat," 2021.

[17] University of Victoria, *Orcasat*, https://www.orcasat.ca/, 2022.

[18] Government of Canada, *Canadian cubesat project*, https://www.asc-csa.gc.ca/eng/satellites/cubesat/, 2022.

[19] Government of Canada, *Cubesats initiative in canada for stem*, https://www.asc-csa.gc.ca/eng/funding-programs/funding-opportunities/ao/2022-cubics-cubesats-initiative-in-canada-for-stem.asp, 2022.

[20] L. Stras, D. D. Kekez, G. J. Wells, *et al.*, "The design and operation of the canadian advanced nanospace experiment (canx-1)," in *Proc. AMSAT-NA 21st Space Symposium, Toronto, Canada*, Citeseer, 2003, pp. 150–160.

[21] E. Kahr, O. Montenbruck, K. O'Keefe, *et al.*, "Gps tracking on a nanosatellite the canx-2 flight experience," in *8th International ESA Conference on Guidance, Navigation & Control Systems*, 2011, pp. 5–10.

[22] G. Bonin, N. Roth, S. Armitage, J. Newman, B. Risi, and R. E. Zee, "Canx–4 and canx–5 precision formation flight: Mission accomplished!," 2015.

[23] R. Vincent and R. Van Der Pryt, "The canx-7 nanosatellite ads-b mission: A preliminary assessment," *Positioning*, vol. 8, no. 1, pp. 1–11, 2017.

[24] R. Vincent and K. Freitag, "The canx-7 ads-b mission: Signal propagation assessment," *Positioning*, vol. 10, no. 1, pp. 1–15, 2019.

[25] B. Cotton, I. Bennett, and R. Zee, "On-orbit results from the canx-7 drag sail deorbit mission," 2017.

[26] F. Mier-Hicks and P. C. Lozano, "Electrospray thrusters as precise attitude control actuators for small satellites," *Journal of Guidance, Control, and Dynamics*, vol. 40, no. 3, pp. 642–649, 2017.

[27] D. Sternberg, J. Essmiller, C. Colley, A. Klesh, and J. Krajewski, "Attitude control system for the mars cube one spacecraft," in *2019 IEEE Aerospace Conference*, IEEE, 2019, pp. 1–10.

[28] D. Sternberg, "Insight entry descent and landing support by the mars cube one spacecraft," 2019.

[29] E. Fonda-Marsland, G. Roberts, D. Gibbon, and C. Ryan, "Development of a low-cost 0.1 n high test peroxide thruster using additive manufacturing," in *AIAA Propulsion and Energy 2019 Forum*, 2019, p. 4227.

[30] C. Smith, D. Cavender, L. Littleton, and E. G. Lightsey, "Assembly integration and test of the lunar flashlight propulsion system," in *AIAA SCITECH 2022 Forum*, 2022, p. 1731.

[31] Busek, *Bgt-x5*, https://www.busek.com/bgtx5, 2023.

[32] I. Krusharev, R. Poyck, B. Zandbergen, A. Cervone, and Q. Bellini, "Cubesat micro-propulsion systems for extending the capabilities of academic projects," *Impulse [Ns]*, vol. 34, pp. 1–8, 2014.

[33] J. Foust, *Deep space smallsats face big challenges*, https://spacenews.com/deep-space-smallsats-face-big-challenges/, 2023.

[34] D. Rafalskyi, J. M. Martínez, L. Habl, *et al.*, "In-orbit demonstration of an iodine electric propulsion system," *Nature*, vol. 599, no. 7885, pp. 411–415, 2021.

[35] C. Ma, T. Bull, and C. N. Ryan, "Plume composition measurements of a high-emission-density electrospray thruster," *Journal of Propulsion and Power*, vol. 37, no. 6, pp. 816–831, 2021.

[36] D. Krejci, F. Mier-Hicks, C. Fucetola, P. Lozano, A. H. Schouten, and F. Martel, "Design and characterization of a scalable ion electrospray propulsion system," 2015.

[37] A. Rudolph, "Lisa pathfinder launch and early operations phase-in-orbit experience," in *14th International Conference on Space Operations*, 2016, p. 2412.

[38] D. Krejci and A. Reissner, "The first 100 feep propulsion systems in space: A statistical view and lessons learnt of 4 years of enpulsion," in *IEPC-2022-199, 37th International Electric Propulsion Conference*, 2022.

[39] L. Grimaud, T. Schönherr, I. Vasiljevich, A. Reissner, D. Krejci, and B. Seifert, “Qualification status update of the micro r3 and nano r3 feep thrusters,” in *IEPC-2022-201, 37th International Electric Propulsion Conference*, 2022.

[40] D. G. Courtney, H. Shea, K. Dannenmayer, and A. Bulit, “Charge neutralization and direct thrust measurements from bipolar pairs of ionic electrospray thrusters,” *Journal of Spacecraft and Rockets*, vol. 55, no. 1, pp. 54–65, 2018.

[41] J.-P. Boeuf, “Tutorial: Physics and modeling of hall thrusters,” *Journal of Applied Physics*, vol. 121, no. 1, p. 011 101, 2017.

[42] F. Chan-Ying and M. Jugroot, “Simulation and design of a micro-hall thruster for spacecraft,” in *AIAA Propulsion and Energy 2021 Forum*, 2021, p. 3442.

[43] C. Ellison, Y. Raitses, and N. J. Fisch, “Cross-field electron transport induced by a rotating spoke in a cylindrical hall thruster,” *Physics of Plasmas*, vol. 19, no. 1, p. 013 503, 2012.

[44] P. Lascombes, M. Montès, A. Fiorentino, T. Gelu, M. Fillastre, and A. Gurciullo, “Lessons learnt from operating the first cubesat mission equipped with a hall thruster,” 2021.

[45] D. A. Spencer, B. Betts, J. M. Bellardo, A. Diaz, B. Plante, and J. R. Mansell, “The lightsail 2 solar sailing technology demonstration,” *Advances in Space Research*, vol. 67, no. 9, pp. 2878–2889, 2021.

[46] D. Krejci, F. Mier-Hicks, C. Fucetola, and P. Lozano, “High efficiency ionic liquid electrospray propulsion for nanosatellites,” in *International Astronautical Congress*, 2016.

[47] B. Reddy, E. Codner, R. E. Hainley, and W. C. Tang, “Design and fabrication of field-emission tips with self-aligned gates,” *Micro & Nano Letters*, vol. 11, no. 9, pp. 518–523, 2016.

[48] B. Little and M. Jugroot, “Bimodal propulsion system for small spacecraft: Design, fabrication, and performance characterization,” *Journal of Spacecraft and Rockets*, vol. 57, no. 4, pp. 707–719, 2020.

[49] D. Krejci, A. Reissner, T. Schönherr, B. Seifert, Z. Saleem, and R. Alejos, “Recent flight data from ifm nano thrusters in a low earth orbit,” in *36th International Electric Propulsion Conference*, 2019, pp. 15–20.

[50] C. Chong, C. Maolin, and Z. Haohao, “Characterization of an ionic liquid electrospray thruster with a porous ceramic emitter,” *Plasma Science and Technology*, vol. 22, no. 9, p. 094 009, 2020.

[51] M. R. Natisin, H. L. Zamora, Z. A. Holley, *et al.*, “Efficiency mechanisms in porous-media electrospray thrusters,” *Journal of Propulsion and Power*, vol. 37, no. 5, pp. 650–659, 2021.

[52] D. G. Courtney, S. Dandavino, and H. Shea, “Comparing direct and indirect thrust measurements from passively fed ionic electrospray thrusters,” *Journal of Propulsion and Power*, vol. 32, no. 2, pp. 392–407, 2016.

[53] P. Mallalieu and M. Jugroot, “Investigation of droplet mode electrospray emitters for use in multimodal systems for spacecraft,” in *AIAA Propulsion and Energy 2021 Forum*, 2021, p. 3438.

[54] B. S. Peter, R. A. Dressler, Y.-h. Chiu, and T. Fedkiw, “Electrospray propulsion engineering toolkit (espet),” *Aerospace*, vol. 7, no. 7, p. 91, 2020.

[55] R. A. Dressler and B. St Peter, “Electrospray propulsion engineering toolkit, espet 1.0,” 2018, Developed for: National Aeronautics and Space Administration.

[56] J. Hanwu, C. Maolin, L. Xuhui, *et al.*, “Experimental study of a porous electrospray thruster with different number of emitter-strips,” *Plasma Science and Technology*, vol. 23, no. 10, p. 104 003, 2021.

[57] T. Morris, C. Malardier-Jugroot, and M. Jugroot, “Characterization of electrospray beams for micro-spacecraft electric propulsion applications,” *Journal of Electrostatics*, vol. 71, no. 5, pp. 931–938, 2013.

[58] F. Mier-Hicks and P. C. Lozano, "Spacecraft-charging characteristics induced by the operation of electrospray thrusters," *Journal of Propulsion and Power*, vol. 33, no. 2, pp. 456–467, 2017.

[59] D. Howe, "Design of an electrospray thruster power processing and digital control interface unit," California Polytechnic State University, San Luis Obispo, 2020.

[60] H. Huh and R. E. Wirz, "Numerical simulation of electrospray thruster extraction," in *36th International Electric Propulsion Conference*, 2019, pp. 15–20.

[61] L. Rayleigh, "Xx. on the equilibrium of liquid conducting masses charged with electricity," *The London, Edinburgh, and Dublin Philosophical Magazine and Journal of Science*, vol. 14, no. 87, pp. 184–186, 1882.

[62] J. Zeleny, "The electrical discharge from liquid points, and a hydrostatic method of measuring the electric intensity at their surfaces," *Physical Review*, vol. 3, no. 2, p. 69, 1914.

[63] G. I. Taylor, "Disintegration of water drops in an electric field," *Proceedings of the Royal Society of London. Series A. Mathematical and Physical Sciences*, vol. 280, no. 1382, pp. 383–397, 1964.

[64] L. De Juan and J. F. De La Mora, "Charge and size distributions of electrospray drops," *Journal of colloid and interface science*, vol. 186, no. 2, pp. 280–293, 1997.

[65] R. Krpoun, "Micromachined electrospray thrusters for spacecraft propulsion," EPFL, Tech. Rep., 2009.

[66] M. Huberman, J. Beynon, E. Cohen, D. Goldin, P. Kidd, and S. Zafran, "Present status of colloid microthruster technology.," *Journal of Spacecraft and Rockets*, vol. 5, no. 11, pp. 1319–1324, 1968.

[67] M. Tajmar, A. Genovese, and W. Steiger, "Indium field emission electric propulsion microthruster experimental characterization," *Journal of Propulsion and Power*, vol. 20, no. 2, pp. 211–218, 2004.

[68] S. Marcuccio, A. Genovese, and M. Andrenucci, "Experimental performance of field emission microthrusters," *Journal of Propulsion and Power*, vol. 14, no. 5, pp. 774–781, 1998.

[69] D. G. Courtney, N. Alvarez, and N. R. Demmons, "Electrospray thrusters for small spacecraft control: Pulsed and steady state operation," in *2018 Joint Propulsion Conference*, 2018, p. 4654.

[70] E. M. Petro, C. E. Miller, J. Schmidt, and P. C. Lozano, "Development of an electrospray fragmentation model for kinetic plume modeling," in *36th International Electric Propulsion Conference*, 2019, p. 830.

[71] R. S. Legge Jr and P. C. Lozano, "Electrospray propulsion based on emitters microfabricated in porous metals," *Journal of Propulsion and Power*, vol. 27, no. 2, pp. 485–495, 2011.

[72] R. E. Wirz, "Electrospray thruster performance and lifetime investigation for the lisa mission," in *AIAA Propulsion and Energy 2019 Forum*, 2019, p. 3816.

[73] P. Mallalieu and M. Jugroot, "Development of a time-of-flight diagnostic system for electrospray thrusters," in *IEPC-2022-197, 37th International Electric Propulsion Conference*, 2022.

[74] B. Little and M. Jugroot, "Development of a microthrust balance and ion beam measurement system: Characterizing a dual-mode thruster for spacecraft," *Vacuum*, vol. 164, pp. 367–380, 2019.

[75] P. L. Wright, N. M. Uchizono, A. L. Collins, and R. E. Wirz, "Characterization of a porous tungsten electrospray emitter," in *IEPC-2022-232, 37th International Electric Propulsion Conference*, 2022.

[76] C. T. Lyne, M. F. Liu, and J. Rovey, "A brief review of diagnostics for electrospray propulsion," in *AIAA SCITECH 2023 Forum*, 2023, p. 0263.

[77] C. Perez-Martinez and P. Lozano, "Ion field-evaporation from ionic liquids infusing carbon xerogel microtips," *Applied Physics Letters*, vol. 107, no. 4, p. 043 501, 2015.

[78] J. Rojas-Herrera, I. Jivanescu, D. Freeman, D. Krejci, C. Fucetola, and P. Lozano, “Porous materials for ion-electrospray spacecraft microengines,” *Journal of Nanomechanics and Micromechanics*, vol. 7, no. 3, p. 04 017 006, 2017.

[79] M. Natisin, H. Zamora, W. McGehee, *et al.*, “Fabrication and characterization of a fully conventionally machined, high-performance porous-media electrospray thruster,” *Journal of Micromechanics and Microengineering*, vol. 30, no. 11, p. 115 021, 2020.

[80] R. A. Dressler, B. St. Peter, Y.-H. Chiu, and T. Fedkiw, “Multiple emission sites on porous glass electrospray propulsion emitters using dielectric propellants,” *Journal of Propulsion and Power*, pp. 1–13, 2022.

[81] D. Krejci, L. Grimaud, T. Schönherr, V. Hugonnaud, A. Reissner, and B. Seifert, “Enpulsion nano and micro propulsion systems: Development and testing,” in *AIAA Propulsion and Energy 2021 Forum*, 2021, p. 3420.

[82] P. L. Wright and R. E. Wirz, “Multiplexed electrospray emission on a porous wedge,” *Physics of Fluids*, vol. 33, no. 1, p. 012 003, 2021.

[83] D. G. Courtney and H. Shea, “Influences of porous reservoir laplace pressure on emissions from passively fed ionic liquid electrospray sources,” *Applied Physics Letters*, vol. 107, no. 10, p. 103 504, 2015.

[84] D. Bock, M. Ebert, F. Roesler, M. Koessling, and M. Tajmar, “Development and testing of field emission thrusters at tu dresden,” in *Proceedings of the 5th Russian-German Conference on Electric Propulsion*, 2014, pp. 1–16.

[85] C. Chen, M. Chen, W. Fan, and H. Zhou, “Effects of non-uniform operation of emission sites on characteristics of a porous electrospray thruster,” *Acta Astronautica*, vol. 178, pp. 192–202, 2021.

[86] C. Coffman, L. Perna, H. Li, and P. Lozano, “On the manufacturing and emission characteristics of a novel borosilicate electrospray source,” in *49th AIAA Joint Propulsion Conference and Exhibit*, 2013.

[87] Q. Koch, T. Schönherr, D. Krejci, N. Mühlich, and B. Seifert, “Verification of the thrust vectoring capability of a feep thruster using spatial plasma plume diagnostic measurements,” in *IEPC-2022-201, 37th International Electric Propulsion Conference*, 2022.

[88] M. R. Natisin and H. L. Zamora, “Performance of a fully conventionally machined liquid-ion electrospray thruster operated in pir,” in *36th International Electric Propulsion Conference*, 2019, pp. 9–12.

[89] C. Huang, J. Li, M. Li, T. Si, C. Xiong, and W. Fan, “Experimental investigation on current modes of ionic liquid electrospray from a coned porous emitter,” *Acta Astronautica*, vol. 183, pp. 286–299, 2021.

[90] C. Huang, L. Jianling, and L. Mu, “Performance measurement and evaluation of an ionic liquid electrospray thruster,” *Chinese Journal of Aeronautics*, 2021.

[91] E. Petro, A. Bruno, P. Lozano, L. E. Perna, and D. Freeman, “Characterization of the tile electrospray emitters,” in *AIAA Propulsion and Energy 2020 Forum*, 2020, p. 3612.

[92] C. Pirat, F. Ankersen, R. Walker, and V. Gass, “Vision based navigation for autonomous cooperative docking of cubesats,” *Acta Astronautica*, vol. 146, pp. 418–434, 2018.

[93] T. S. Rose, D. W. Rowen, S. LaLumondiere, *et al.*, “Optical communications downlink from a 1.5 u cubesat: Ocsd program,” in *International Conference on Space Optics—ICSO 2018*, International Society for Optics and Photonics, vol. 11180, 2019, 111800J.

[94] D. G. Courtney, Z. Wood, S. Gray, and J. Model, “High-speed transient characterization of the busek bet-300-p electrospray thruster,” in *36th International Electric Propulsion Conference*, 2019.

[95] D. G. Fearn, “Ion thruster thrust vectoring requirements and techniques,” in *27th International Electric Propulsion Conference*, 2001, pp. 1–115.

[96] N. R. Demmons, Z. D. Wood, A. Margousian, J. Knott, and T. Fedkiw, “Electrospray attitude control system flight preparation,” in *AIAA SCITECH 2022 Forum*, 2022, p. 0039.

[97] T. P. Forbes, *Electrohydrodynamics and ionization in the array of micromachined ultrasonic electrospray (amuse) ion source*. Georgia Institute of Technology, 2010.

[98] W.-C. Yan, P. Davoodi, Y. W. Tong, and C.-H. Wang, “Computational study of core-shell droplet formation in coaxial electrohydrodynamic atomization process,” *AIChE Journal*, vol. 62, no. 12, pp. 4259–4276, 2016.

[99] L. Brieda, *Plasma simulations by example*. CRC Press, 2019.

[100] J. M. Jones, T. M. Moeller, L. Costa, B. K. Canfield, and A. Terekhov, “Numerical investigation of the effects of geometry and materials on the onset voltage of electrospray emitters,” *Journal of Electrostatics*, vol. 108, p. 103 487, 2020.

[101] F. M. Hicks, L. Perna, C. S. Coffman, and P. C. Lozano, “Characterization of a cubesat compatible magnetically levitated thrust balance for electrospray propulsion systems,” in *49th AIAA/ASME/SAE/ASEE Joint Propulsion Conference*, 2013, p. 3879.

[102] J. Eisen, B. Cline, S. P. Berg, and J. Rovey, “Power processing unit and feed system development for a multimode spacecraft propulsion system,” in *AIAA Propulsion and Energy 2021 Forum*, 2021, p. 3428.

[103] A. R. Bruno and P. C. Lozano, “Design and testing of a propellant management system for bimodal chemical-electrospray propulsion,” in *2021 IEEE Aerospace Conference (50100)*, IEEE, 2021, pp. 1–7.

[104] A. Bruno, M. Schroeder, and P. C. Lozano, “Characterization of electrospray thrusters with han-based monopropellants for multimode propulsion applications,” in *AIAA SCITECH 2022 Forum*, 2022, p. 2490.

[105] C. T. Lyne, J. Rovey, and S. P. Berg, “Monopropellant-electrospray multimode thruster testing results: Electrospray mode,” in *AIAA Propulsion and Energy 2021 Forum*, 2021, p. 3439.

[106] N. Brikner and P. C. Lozano, “The role of upstream distal electrodes in mitigating electrochemical degradation of ionic liquid ion sources,” *Applied Physics Letters*, vol. 101, no. 19, p. 193 504, 2012.

[107] K. Battes, C. Day, and V. Hauer, “Outgassing behavior of different high-temperature resistant polymers,” *Journal of Vacuum Science & Technology A: Vacuum, Surfaces, and Films*, vol. 36, no. 2, p. 021 602, 2018.

[108] K. J. P. Veeramraju and J. W. Kimball, “An improved power processing unit for multi-mode monopropellant electrospray thrusters for satellite propulsion systems,” in *2019 IEEE Energy Conversion Congress and Exposition (ECCE)*, IEEE, 2019, pp. 1302–1309.

[109] C. T. Lyne, M. F. Liu, and J. L. Rovey, “A low-cost linear time-of-flight mass spectrometer for electrospray propulsion diagnostics,” in *IEPC-2022-178, 37th International Electric Propulsion Conference*, 2022.

[110] M. S. Alexander, J. Stark, K. L. Smith, B. Stevens, and B. Kent, “Electrospray performance of microfabricated colloid thruster arrays,” *Journal of Propulsion and Power*, vol. 22, no. 3, pp. 620–627, 2006.

[111] R. W. Schafer, “What is a savitzky-golay filter? [lecture notes],” *IEEE Signal Processing Magazine*, vol. 28, no. 4, pp. 111–117, 2011.

A VET PPU and DCIU

As discussed, a custom PPU was developed to operate and monitor two emitters, while a custom DCIU was developed to receive TM from and transmit TC to the PPU and provide a GUI to the user. The PPU was controlled by a Bluno Mega 2560 evaluation board that interfaced with a personal computer via wired serial communication. Firmware for the Mega 2560 was developed in C and uploaded via the Arduino integrated development environment (IDE), while the GUI software was developed in Python.

A.1 VET PPU

A detailed schematic of the VET PPU control and DAQ hardware, developed using KiCad, is shown in Fig. A.1. Starting from the left, a Microchip MCP4922 12-bit dual-channel voltage output DAC, which communicated via the serial peripheral interface (SPI) protocol, was used to convert digital commands from the microcontroller into HV commands to the HV converters. The DAC was followed by a Texas Instruments TLV4112 dual channel, high output drive (>300 mA) op-amp. Next, the A30P-5 (+3000 V) and A30N-5 (−3000 V) converters were selected to deliver bipolar HV rails to each of the emitters, while HVM OPTO-150 15 kV HV optocouplers were used to toggle the HV rails at the specified duty cycles. The required input current of each A30 was 300 mA, but the output current of the MCP4922 was limited to 25 mA per channel, so the TLV4112 was added as a voltage follower. Similarly, the OPTO-150s required an input current of 360 mA, but the Mega 2560 could only output 40 mA per pin, so Philips 2N2222 NPN switching transistors were used to drive current directly from the +5 V power rail. An RC clamping circuit, consisting of a 47 Ω resistor and 470 pF Vishay Cera-Mite 3 kV ceramic capacitor, with a time constant of 22 ns and impedance of 969 Ω was added to each HV rail to reduce the HV transients during switching. A high-side VD and high-side SR were placed directly prior to each emitter to measure the consumed voltage and current, respectively. This housekeeping data was directed to Avago HCPL-7510 iso-amps, which had an input voltage range of ±200 mV and an output voltage range of 0 to 5 V. Texas Instrument DCH010505 1 W, 3 kV isolated DC-DC converters provided a floating 5 V potential to the iso-amps, which output their signals to the built-in ADC in the Mega 2560. Notably, all components required a supply voltage of 5 V, which eliminated the need for intermediate buck/boost converters.

The VET PPU HV CTRL and DAQ PCBs developed for this research are illustrated in Figs. A.2 and A.3. The front mask, terminals, and front silkscreen are shown in Fig. A.2, whereas the the back mask and terminals are shown in Fig. A.3. Each of the PCBs were designed to meet CubeSat volume standards, hence the PCBs have dimensions of 96 mm × 96 mm. Note that these PCBs do not contain RC filtering circuitry on the HV rails or HCPL-7510 input lines.

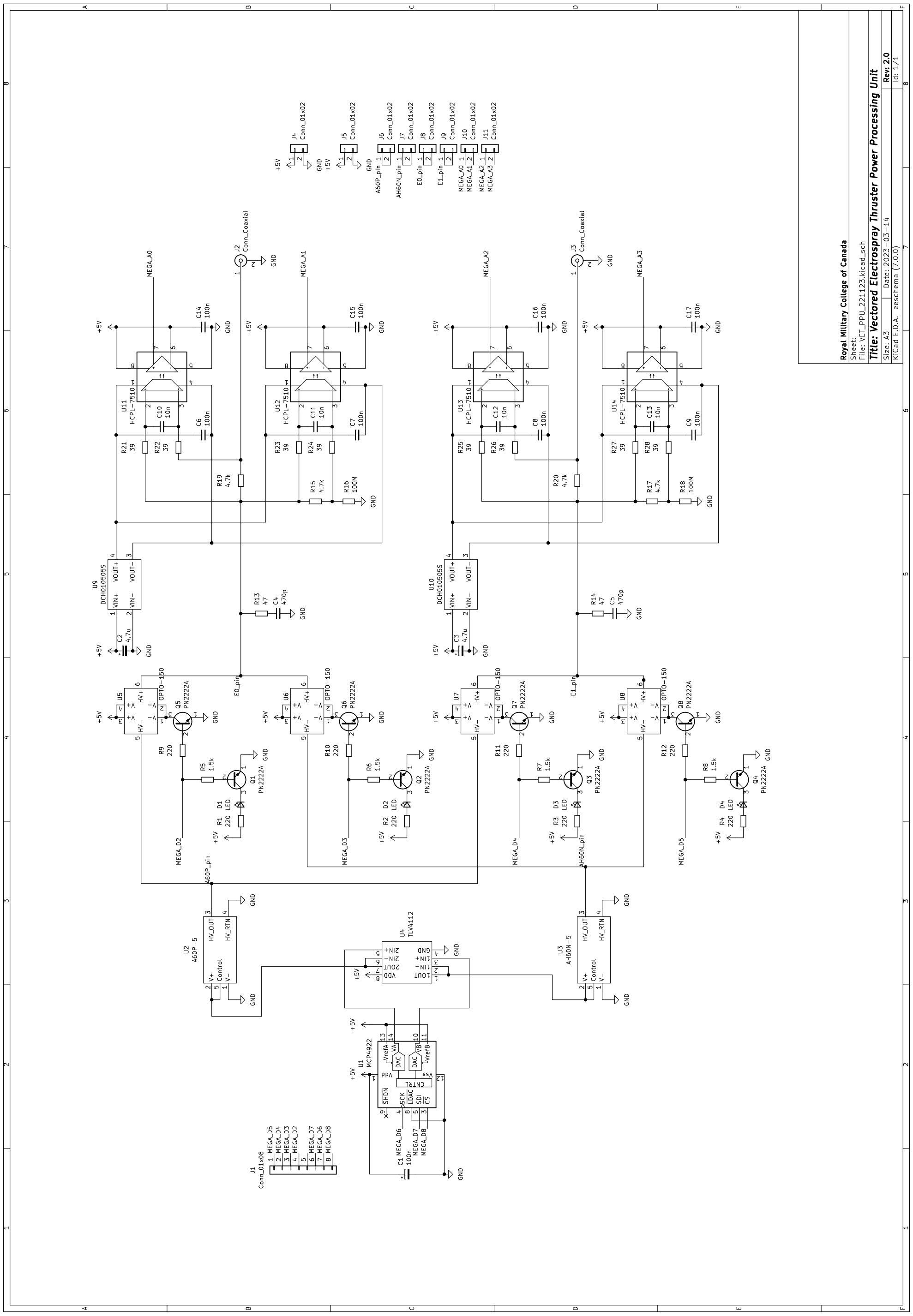

Figure A.1: Detailed VET PPU schematic.

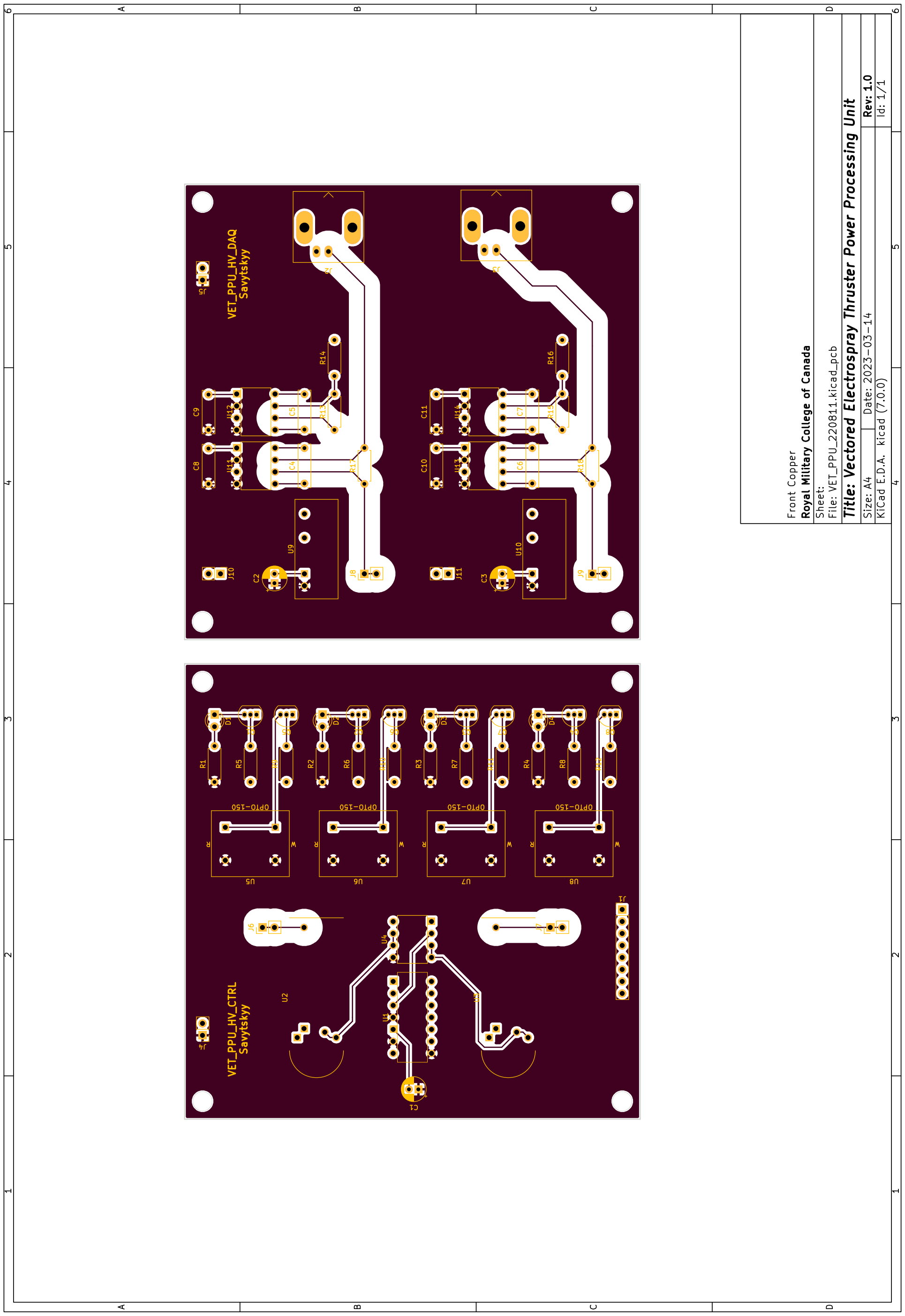

Figure A.2: Detailed VET PPU PCB front.

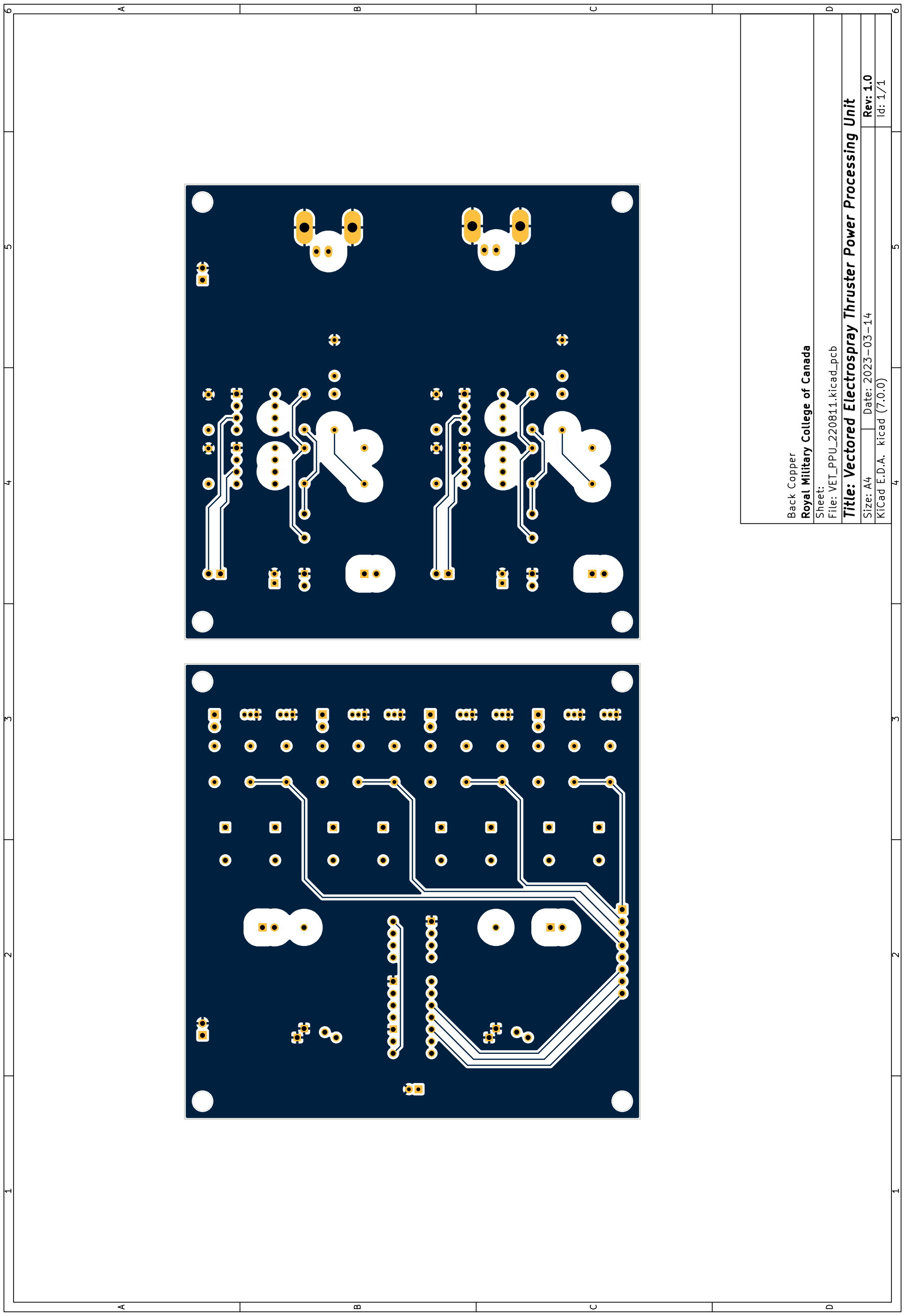

Figure A.3: Detailed VET PPU PCB back.

Since the Mega 2560 ADC could only receive 0 to 5 V, a summing amplifier circuit was included to add a 2.5 V DC offset to the FEMTO output. This schematic is shown in Fig. A.4. The gain on the non-inverting input was $A_{\text{non-inv}} = 1 + R_{\text{feedback}}/R_{\text{in}}$, therefore an input voltage of 1.25 V was applied. The gain on the inverting input was $A_{\text{inv}} = -R_{\text{feedback}}/R_{\text{in}}$.

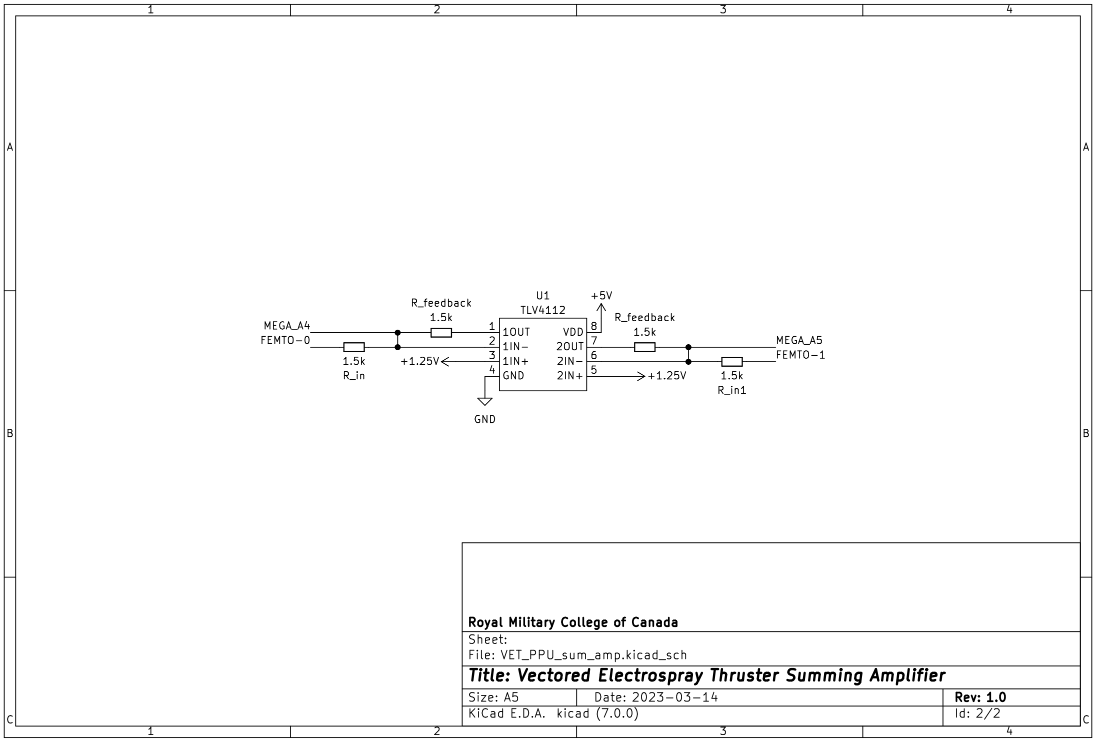

Figure A.4: Summing amplifier schematic for FEMTO output.

Figure A.5 is a closeup photo of the A30N-5 IC. As discussed, these converters were selected due to their extremely small form factor and low power requirements. Indeed, these converters have dimensions of 29 mm × 11 mm × 6 mm and require only 1 W input power each, making them highly conducive to meet the SWaP requirements of nanosatellites. The proportional input/output characteristics of the A30s for a $10\,\mathrm{M\Omega}$ load are illustrated in Fig. A.6. Based on the linear trendline, calculated using the Python `numpy.polyfit` function, both HV converters would theoretically reach a maximum output voltage of ±2500 V. The switching characteristics of the A30s using the OPTO-150s are illustrated in Fig. A.7, where a Cal Test ELDITEST GE3421 100 MHz, 100:1 attenuation, 4 kV oscilloscope probe was used directly on the HV rails. The LHS of Fig. A.7 shows the fall time of the A30N-5 converter followed by the rise time of the A30P-5 with and without the added RC clamping circuit. As shown, the fall time of the converters is typically 100 ms. The RHS of Fig. A.7 shows a higher-resolution capture of the rise times of both A30 converters with the RC clamping circuit, with a rise time of 1.5 ms being observed. Finally, HV duration testing of the A30s is illustrated in Fig. A.8. Both the A30P-5 and A30N-5 were able to operate at or above ±2000 V for extended periods, though noticeably the A30N-5 was able to reach a higher magnitude than the A30P-5. It was not determined why this asymmetry occurred, though as discussed in Chapter 6, this had the effect of increasing the magnitude of the output electrospray current of the negative polarity relative to the positive polarity.

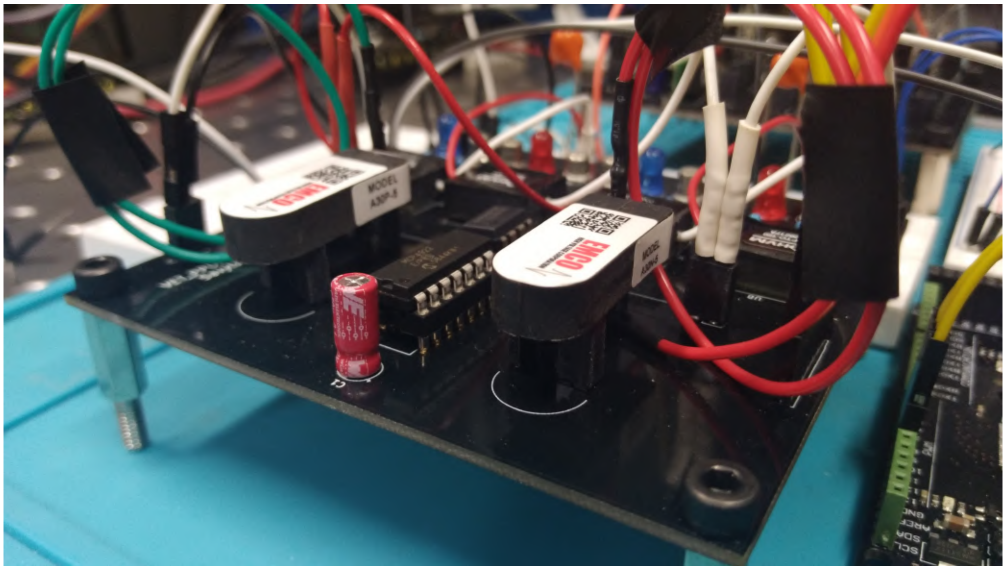

Figure A.5: A30N-5 closeup.

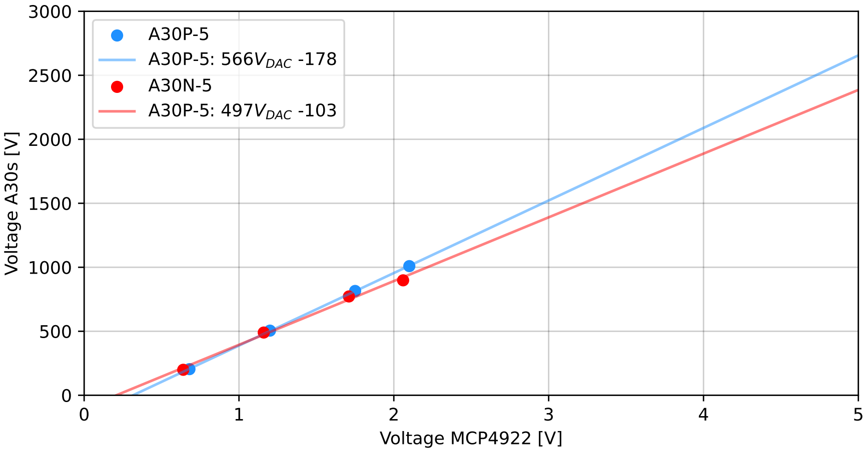

Figure A.6: Control of the A30 converters via the MCP4922 DAC.

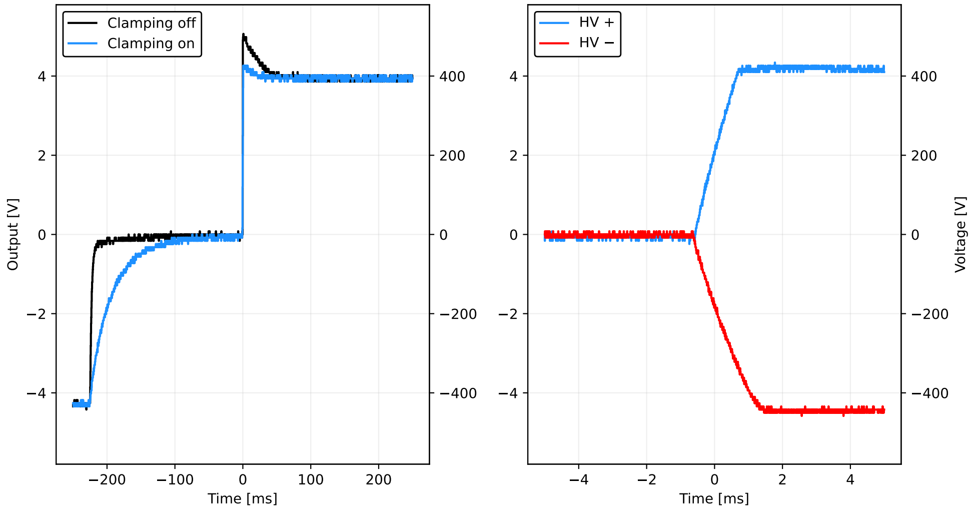

Figure A.7: HV rise and fall times and clamping circuit and switching characterization of the A30s, as measured on an oscilloscope.

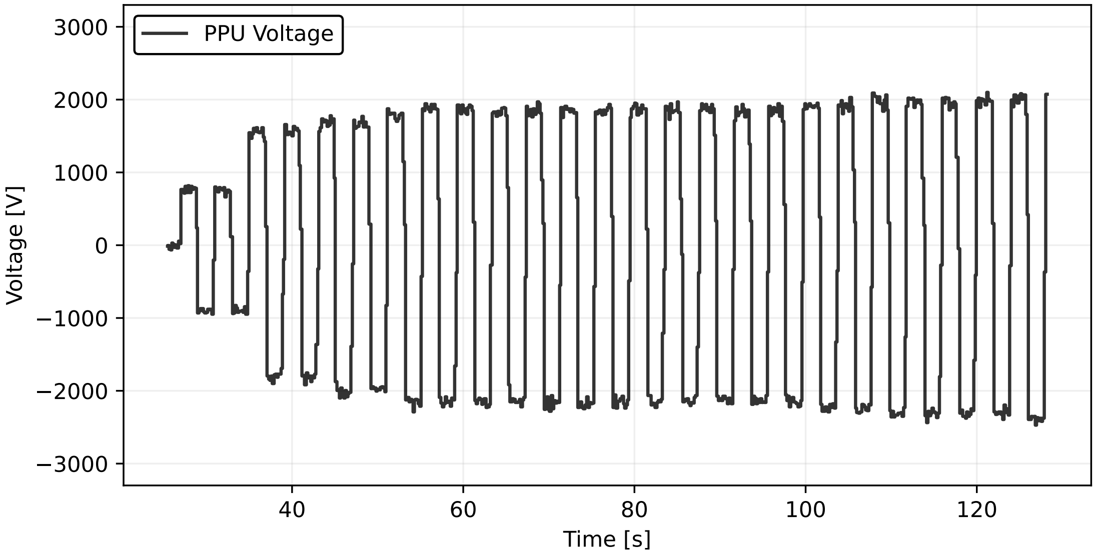

Figure A.8: HV duration testing of the A30 converters.

A.2 VET DCIU

As discussed, the Mega 2560 microcontroller was used to interface between the PPU and the parent system. The Mega 2560 ran a single-thread C script that controlled the PPU, regularly polled for TC from the parent system, and transmitted TM to the parent system. The control software for the DCIU GUI was written in Python, where the `tkinter` library was used to create the GUI application—illustrated in Fig. A.9—which received and displayed incoming frames from the Mega 2560. A separate background thread received serial TM data from the Mega 2560 and stored it to a .csv file, while the primary thread processed and visualized the TM data using `matplotlib.animation.FuncAnimation` at a rate of 10 samples per second. The data transfer protocol for transmitting TC to the PPU is tabulated in Table A.1, while the data transfer protocol for receiving TM from the PPU is tabulated in Table A.2.

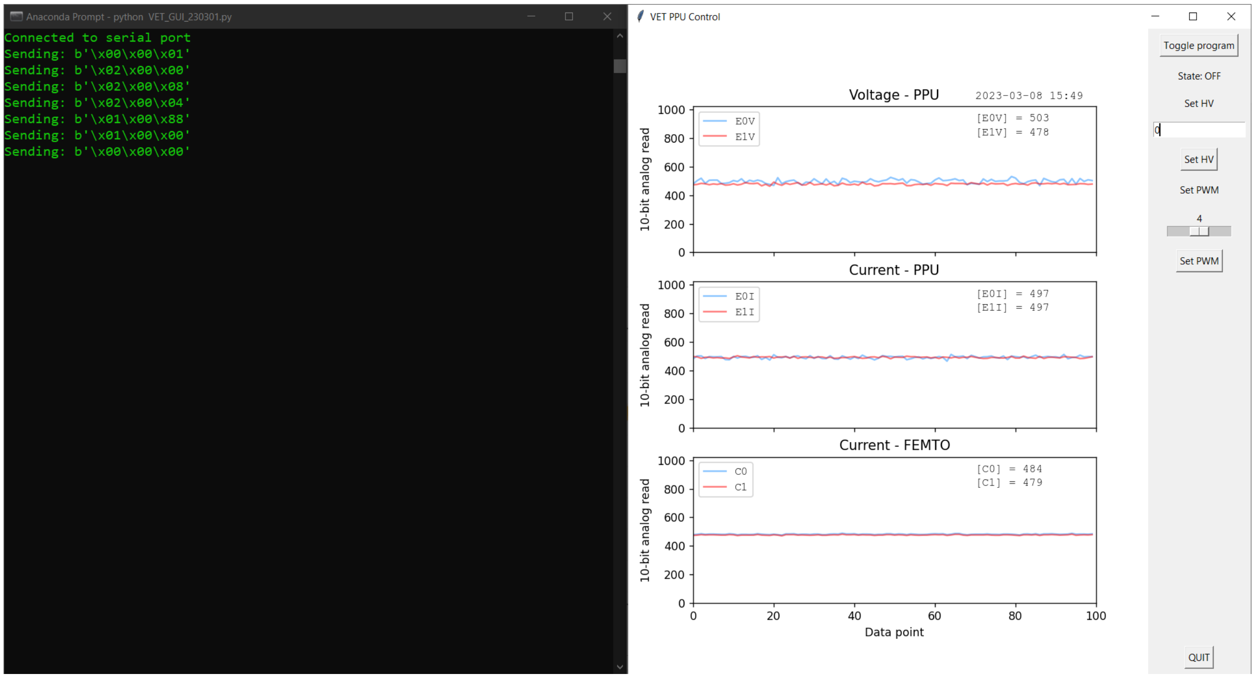

```
Connected to serial port
Sending: b'\x00\x00\x01'
Sending: b'\x02\x00\x00'
Sending: b'\x02\x00\x08'
Sending: b'\x02\x00\x04'
Sending: b'\x01\x00\x88'
Sending: b'\x01\x00\x00'
Sending: b'\x00\x00\x00'
```

2023-03-08 15:49

[E0V] = 503
[E1V] = 478

[E0I] = 497
[E1I] = 497

[C0] = 484
[C1] = 479

State: OFF
Set HV: 0
Set PWM: 4

Figure A.9: DCIU GUI screenshot.

Table A.1: DCIU packet protocol to transmit TC.

Command	Range	Command ID	Length [bytes]	Type
Toggle PPU	[0, 1]	0	1	uint16
Set HV	[0, 2999]	1	2	uint16
Set PWM	[0, 8]	2	2	uint16

Table A.2: DCIU packet protocol to receive TM.

Data	Range	Length [bytes]	Type	Offset
E0 HV	[0, 1023]	2	uint16	0
E1 HV	[0, 1023]	2	uint16	2
E0 current	[0, 1023]	2	uint16	4
E1 current	[0, 1023]	2	uint16	6
FEMTO-0	[0, 1023]	2	uint16	8
FEMTO-1	[0, 1023]	2	uint16	10